Louisiana State University
LSU Digital Commons

LSU Master's Theses | Graduate School

2013

Development of a laboratory scale reactor facility to generate hydrogen rich syngas via thermochemical energy conversion

Mandeep Sharma
Louisiana State University and Agricultural and Mechanical College, mandeepsharma14@gmail.com

Follow this and additional works at: https://digitalcommons.lsu.edu/gradschool_theses

 Part of the Mechanical Engineering Commons

Recommended Citation
Sharma, Mandeep, "Development of a laboratory scale reactor facility to generate hydrogen rich syngas via thermochemical energy conversion" (2013). *LSU Master's Theses*. 3436.
https://digitalcommons.lsu.edu/gradschool_theses/3436

This Thesis is brought to you for free and open access by the Graduate School at LSU Digital Commons. It has been accepted for inclusion in LSU Master's Theses by an authorized graduate school editor of LSU Digital Commons. For more information, please contact gradetd@lsu.edu.

DEVELOPMENT OF A LABORATORY SCALE REACTOR FACILITY TO GENERATE HYDROGEN RICH SYNGAS VIA THERMOCHEMICAL ENERGY CONVERSION

A Thesis

Submitted to the Graduate Faculty of the
Louisiana State University and
Agricultural and Mechanical College
in partial fulfillment of the
requirements for the degree of
Master of Science in Mechanical Engineering

in

The Department of Mechanical Engineering

by
Mandeep Sharma
B. Tech. M.E., Punjab Technical University, 2007
May 2013

Dedicated to my father, Late Mr. Raj Paul Sharma

Acknowledgments

First of all, I would like to express my sincere gratitude to my advisor, Dr. Ingmar Schoegl for his consistent support, guidance and help throughout this thesis work. This thesis would not have been possible without his persistent support. I would like to thank my advisory committee members, Dr. Ram Devireddy and Dr. Ying Wang for being a part of it. The Louisiana State University Council on Research Faculty Research Grant Program is highly acknowledged for providing funding for this study.

I would like to thank my colleagues at Combustion Research Group for their immense help and motivation during my two years at LSU. More specifically, Matthew Lousteau provided significant assistance in initial set-up for cold flow model studies, Avishek Guha's contribution towards the set-up for carrier gas vaporizer/bubbler. Joseph Gibson, Mohsen Ayoobi, Avishek and Khurshida Sharmin provided me an immediate assistance in programming issues and their rides whenever I need to buy anything for experiments from local stores. Joe Poynot's contribution for building the temperature control panel for carrier gas vaporizer is greatly appreciated.

I sincerely thank Zianqing Zhao, graduate student of Dr. Wang's research group, for providing excellent assistance in preparation of catalysts. I would like to express my appreciation to Devendra Pakhare, graduate student of Dr. Spivey in chemical engineering department, for carrying out BET surface area measurement and Temperature Programmed Reduction (TPR) tests for characterization of catalysts.

I would also like to mention sincere thanks to all my friends I made at LSU, Dr. Kahlon, Dr. Singh, Narinder, Jaspreet, Kirandeep, Sukh, Ahmed and Pratap who made these two years a memorable experience to cherish forever.

Finally, I am very grateful to my family; my mom, sister Seema, brother Vippy, uncle Gorkhnath, fiancée Rupali and best friend Ashish for being the source of my motivation and support throughout my academic journey at LSU.

Table of Contents

List of Tables

List of Figures

Abstract

The thesis provides data needed for development of a conical spouted bed (CSB) reactor for the purpose of producing hydrogen rich synthesis gas (syngas). The syngas has potential to utilize energy more efficiently, eliminate pollutant emissions and significantly cut emissions of greenhouse gases. The development of CSB reactor system involves three phases. The first phase investigates the hydrodynamic behavior of a small, laboratory scale, conical spouted bed (CSB) by considering the effect of specific system parameters (stagnated bed height, particle size and inlet diameter) on minimum spouting velocity $(u_{ms})_o$, stable operating pressure drop (ΔP_{ms}) and maximum pressure drop (ΔP_M). Experimental results show fair agreement with correlations for $(u_{ms})_o$ available in existing literature. Using experimental data, an alternative correlation for minimum spouting velocity is developed. Improvements of prediction quality are attributed to the inclusion of an additional non-dimensional geometry parameter relating particle diameter to inlet diameter, which is absent from most, previously published correlations. The second phase involves an experimental assessment of multiple propane reforming pathways: dry reforming (DR), partial oxidation (POX), steam reforming (SR) and auto-thermal reforming (ATR). The selection of operating conditions for experiments – reactants feed ratio, pressure and temperature – is guided by results from thermodynamic equilibrium. In experiments, the propane conversion efficiency increases with temperature and 100% efficiency is achieved mostly at 1000°C. The propane conversion efficiency for homogeneous ATR process always appears higher than DR, POX and SR which is in agreement with thermodynamic equilibrium analysis. The thermodynamic equilibrium predictions and experimental results for homogeneous fuel reforming suggest that the hydrogen production efficiency for homogeneous ATR is higher than DR, POX and SR. The hydrogen production efficiency is higher in thermodynamic equilibrium as compared to experiments for homogeneous DR, POX, SR and ATR. This difference is due to the formation of small hydrocarbon species such as acetylene and ethane in actual tests whereas negligible amount of them appeared in thermodynamic equilibrium. The third phase of CSB reactor facility eventually involves construction of a bench top laboratory scale CSB for the follow-up research where similar tests are required to perform.

Chapter 1
Introduction

1.1 Research Motivation

The declining fossil fuel supplies as well as rising demand for clean transportation fuels in recent years have stimulus intensive research for efficient alternative sources. Hydrogen at present is mainly used for production of ammonia and methanol, in oil refineries and in hydrogenation facilities in the chemical industry. It has been attracting great interest as a major source of eco-friendly future clean fuel for small and portable power applications including combustion engines, gas turbines and fuel cells. Hydrogen contains more energy per unit mass than any other fuel. Hydrogen and synthesis gas (mixture of hydrogen and carbon monoxide) production via thermochemical technologies (Figure1.1) can utilize energy more efficiently, eliminate pollutant emissions and significantly cut emissions of greenhouse gases [10].

Syngas production can contribute to more efficient electrical power generation through advanced energy systems, such as Integrated Gasification Combined Cycle (IGCC) and high temperature fuel cells. Among the active ongoing energy research and development areas are H_2 and syngas production from hydrocarbon resources including fossil fuels, biomass, and carbohydrates. Synthesis gas is considered as an important intermediate product for further syntheses to produce valuable clean transportation fuels. For example, the conversion of synthesis gas to clean transportation fuels such as liquid hydrocarbon fuels, methanol, dimethyl ether, and ethanol [53]. These fuels produced from Fischer–Tropsch (F–T) synthesis are suitable for transportation vehicles because they are sulfur free and have high cetane or octane numbers. The required molar ratio of hydrogen to carbon monoxide, known as syngas ratio, depends on the desired product and fuel processing technology [37]. The composition of the syngas from either gasification processes or syngas production technologies are generally not directly use in the downstream fuel process. In several cases, H_2/CO syngas ratio adjustment techniques such as downstream shift reactors, membrane separators or pressure swing adsorption are used to meet the ratio requirement [45].

Hydrogen production has multiple application areas in chemical industry, food industry, and fuel cell systems. In recent years, fuel cells have gain remarkable popularity in potential applications in transportation, as well as stationary and portable power generation. Figure 1.2 demonstrates a schematic

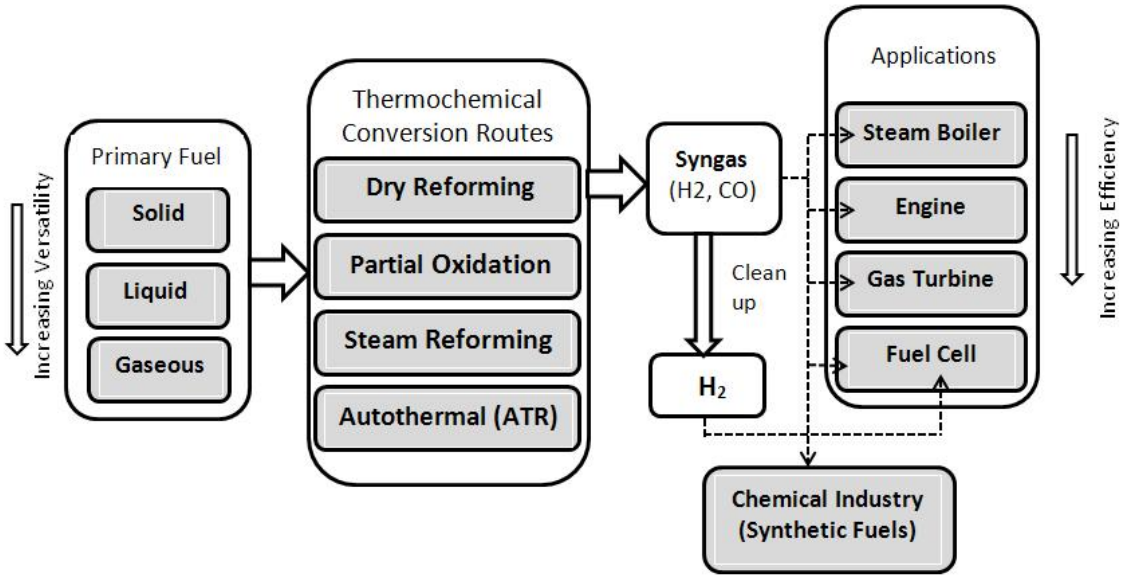

Figure 1.1: Thermochemical energy conversion schematic.

of a fuel cell that directly converts the chemical energy of a fuel primarily hydrogen into electricity. A fuel cell consists of three main components namely; the reactant hydrogen is on anode side, oxygen or air is on cathode side and an electrolyte. Fuel cell electrochemical devices are capable of producing continuous electric energy as long as fuel and an oxidant are fed to the electrodes. The chemical energy is directly converted to electricity and heat without involving combustion cycles as happened in combustion engines.

The recent development of fuel cell has spurred the processing of fuel for compact and portable power systems. Researchers are investigating hydrogen production for these portable power applications from various fuels, such as methane, various kinds of higher hydrocarbons and ethanol as biogenic fuel. One of the major technical challenges associated with hydrogen based portable power generation systems is the supply of hydrogen gas. Most of these systems including fuel cell require hydrogen in molecular form, which is not readily available. Additionally, the low volumetric energy density below 3 Wh/L causes hydrogen an unrealistic choice for storage and transportation as a primary fuel. Its storage requires either large pressures, low temperatures or heavy metal-hydride reservoirs. These technical challenges can be overcome by adopting alternative approach of producing hydrogen from primary hydrogen source in a decentralized and on demand basis [48, 46]. However, hydrogen is abundant in nature; it is primarily bound into other molecules such as hydrocarbons (C_mH_n), oxygenated hydrocarbon ($C_mH_nO_p$) and water

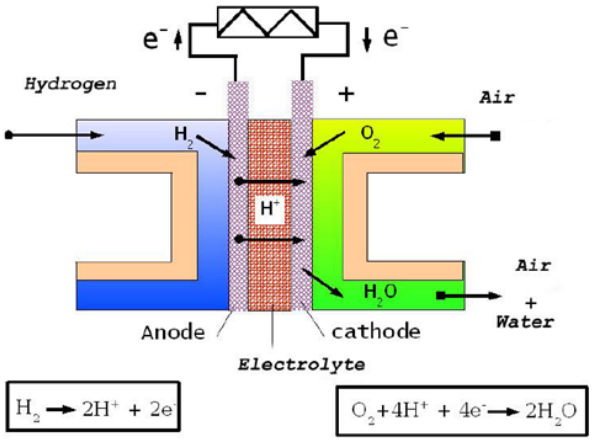

(a) PEM Fuel cell Schematic [36]

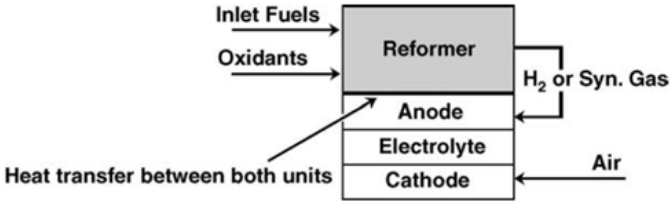

(b) SOFC Fuel Cell Schematic [33]

Figure 1.2: Examples for portable power generation system

(H_2O). Therefore, it is worth pursuing fuel upgrade paths, such as fuel reforming of hydrocarbons and alcohols, gasification of coal or biomass, electrolysis of water [59].

The fuel reforming process converts primary hydrogen source, for example hydrocarbon fuel/oxygenated hydrocarbon fuel into a hydrogen rich synthesis gas (syngas). The syngas mainly consists of hydrogen and carbon monoxide as main species whereas carbon dioxide, methane and other species as minor components. There are two main types of fuel cells reforming: external reforming, which is carried out before the fuel reaches the portable power systems for e.g., PEM (Proton Exchange Membrane, Figure 1.2a), and internal reforming (Figure 1.2b), which takes place within the fuel cell anode for e.g., SOFC (Solid Oxide Fuel Cell). Considerable research has been done in the development of internal reforming portable power systems, one example can be found in high temperature solid oxide fuel cell (SOFC) with an indirect internal reforming operation, called IIR-SOFC (Figure). Although IIR-SOFC does not require a separate fuel reformer and it also provides a good heat transfer between the reformer itself and the fuel cell, it posses a limitation in the sense that it can operate only for limited number of gaseous hydrocarbon fuels such as methane and propane. Thus, a more robust and efficient external fuel reformer is required for PEM fuel cells which can be flexible for wide variety of hydrogen contained primary fuels in solid, liquid or gaseous forms.

The goal of the present thesis is to develop a more advanced, efficient and more flexible fuel reformer/reactor at laboratory scale in order to produce hydrogen rich syngas and which can be suitable

for small and portable power generation applications specifically in remote areas. It can be operated with wide range of hydrocarbon fuels either conventional gaseous fuels such as methane and propane, or biofuel genated liquid wastage such as glycerol, and biomass wastage such as sawdust. The main focus of present thesis is to work towards the development of a conical spouted bed reactor at laboratory scale in order to produce hydrogen rich syngas from hydrocarbon and oxygenated hydrocarbon fuels, such as propane and glycerol. The work towards this goal divides into three phases: the cold flow model facility in the first phase deals with the study of hydrodynamic behavior of a CSB reactor and the second phase involves a simpler plug flow reactor facility which is used for an evaluation of favorable operating conditions for hydrogen rich syngas production. The plug flow reactor is meant to provide preliminary results that are used to evaluate different reforming approaches, which will eventually be applied in a CSB reactor. The different reforming approaches include dry reforming (DR), partial oxidation (POX), steam reforming (SR) and autothermal reforming (ATR). Tests from the plug flow reactor hot flow studies are used to assess the efficiency of each homogeneous reforming process. The selection of operating conditions is guided by results from thermodynamic equilibrium analysis. Some preliminary results for heterogeneous (catalytic) reforming, particularly ATR are presented. These preliminary results are listed as recommended work for the future scope of the thesis. Results from this study will lay the foundation for follow-up research, where similar tests will be performed for a bench-scale CSB reactor facility in the third phase for syngas production.

1.2 Fuel Reforming and Gasification

Hydrogen containing compounds in solid, liquid or gaseous forms such as sawdust, methanol, glycerol, methane and propane respectively, differ significantly in physical, chemical and morphological properties. This necessitates developing different methods of gasification or fuel reforming, consequently requires different reactor designs or even unique fuel reforming technologies. Successful development of the fuel reforming process largely relies on the design of a proper reactor in conjunction with non-catalytic and catalytic reforming routes. The extensive research over the past decade focused mostly on biomass feedstock in the context of hydrogen rich synthesis gas (syngas) generation; biomass gasification produces fuel gas or syn gas through the thermo-chemical conversion processes, usually involving partial oxidation of feedstock in a reducing atmosphere in presence of air, oxygen and/or steam [35, 29].

Table 1.1: Comparison of difference between gas-fluidized beds and gas-spouted beds reactor systems [18].

Parameter	Fluidized Bed Reactor	Spouted Bed Reactor
Mean particle size	~ 0.03 mm; usually < 1 mm	~ 0.6 - 6 mm; usually > 1 mm
Particle size distribution	usually broad	usually narrow
Gas motion	Less ordered; depends on flow regime and specific geometry	Outward from the spout into the dense phase, except just above inlet
Particle motion	Complex flow regimes and particle motion; region surrounding the gas entry orifices is usually fluidized with few particle-particle contact	Systematic circulation patterns, up the spout and slowly downward in the annulus. Annulus is in moving packed bed flow with substantial particle-particle contacts
Column geometry	Usually cylinderical columns	Usually diverging conical base with or without cylinderical portion above
Pressure drop across entry orifices	Usually 30 - 50% of that across the bed	As small as possible consistent with satisfying the other constraints, e.g., orifice dia. < 25 mean particle dia.
Axial gradient of pressure	Virtually independent of height in the column	Varies with height
Superficial gas velocity	Broad range, typically 0.2 to 10 m/s	More limited range, typically 1.1 to 1.8 times minimum spouting velocity

It is also reported by Beenackers [7] in his review of Eurpean technologies for biomass gasification that fluidized bed gasifiers are less suitable to produce syngas from biomass. The reason is they suffer from high tar yields in the product gas. In addition, the inability to maintain uniform radial temperature profiles and to avoid local slagging problems makes them unsuitable for large installations [5].

Mathur and Gishler initially introduced spouted beds in 1954 as an alternative method for drying moist wheat grains [18]. Since then, spouted beds have been used extensively for drying of various granular materials and coating of particles. Spouted bed reactors are suitable for the treatment of material of wide particle size distribution, irregular shape and high moisture content [15]. Moreover, spouted beds have been used for the combustion of solid and heavy liquid fuels [61]. The spouted bed reactor was described as an emerging technology by 1993 for recycling wastes such as coal-tar-contaminated soils, petroleum refinery wastes, and municipal solid wastes, gasified at temperatures of 538 - 870 °C by highly

superheated steam to produce syngas.[18], however, gasification of municipal solid waste in a spout-fluid bed of square cross-section, feed rates and temperatures data is not available. Spouted bed reactors have a potential to generate syngas from biomass wastes, since a very few researchers have used spouted bed reactors in various applications. Some of these examples as mentioned by Cui and Grace [15] in their review on spouting of biomass particles include sawdust was pyrolyzed in a conical spouted bed reactor and pyrolysis of synthetic biomass in a pilot-scale spouted bed reactor for separating heavy metals, pilot-scale air blown spouted bed reactor to assess the gasificaiton of sewage sludge. It has been demonstrated that conical spouted beds (CSBs) have potential for the flash pyrolysis of sawdust and the pyrolysis of plastic wastes and scrap tires [42]. Table 1.1 presents some significant differences between gas-fluidized beds and gas-spouted bed reactors. In the present study, conical spouted bed reactor system is chosen because of its simpler design and thus suited for lab scale reactors. Moreover, it has certain advantages over fluidized bed reactors: fuel flexibility (solid, liquid and gaseous hydrocarbon fuels), lower minimum fluidization velocity, simpler design and efficient contact between the gas and the primary fuel because of uniform cyclic movements inside the bed.

1.3 Thermochemical Energy Conversion

A thermochemical conversion of hydrocarbon fuel, propane in present study, into syngas involves four main types of fuel reforming routes: dry reforming (DR), partial oxidation (PO), steam reforming (SR) and auto-thermal reforming (ATR) [10, 1]. The purpose here is to compare DR, POX, SR and ATR processes, and also to run a baseline study among these by selecting an optimum operating conditions. The optimum conditions include temperature, pressure and reactants feed ratios at particular reactants mixture flow rate. Below is a brief description of each of these reforming process.

1.3.1 Dry Reforming (DR)

In this process, a fuel at high temperature breaks down into hydrogen and other hydrocarbon species. The reaction is either exothermic ($\Delta H_r < 0$) or endothermic ($\Delta H_r > 0$) that depends on the type of fuel.

The dry reforming reaction of a general hydrocarbon fuel can be written as

$$C_mH_n \rightarrow aH_2 + b\text{Hydrocarbons}\,(...CH_4, C_2H_2, C_2H_6, \text{etc.}) + cC \tag{1.1}$$

for example,

$$C_3H_8 \rightarrow aH_2 + \text{other hydrocarbon species (...}CH_4, C_2H_2, C_2H_6, \text{ etc.)} + cC \tag{1.2}$$

$$CH_4 + CO_2 \rightarrow 2CO + 2H_2 \; [\Delta H^o_{298K} = +247.2\,\text{kJmol}^{-1}] \tag{1.3}$$

$$C_3H_8 + 3CO_2 \rightarrow 6CO + 4H_2 \; [\Delta H^o_{298K} = +644.8\,\text{kJmol}^{-1}] \tag{1.4}$$

There has been considerable interest in the dry reforming of methane with CO_2 since this allows two major greenhouse gases (methane and carbon monoxide) to be utilized simultaneously for the production of synthesis gas. It has been proposed that the CO_2 is shifted to CO and H_2O through the reverse water–gas shift (RWGS) reaction, Eq. 1.5, and then H_2O is reacted with CH_4 (Eq. 1.6) to produce syngas during the dry reforming [45]. Since the last decade, hydrogen production via dry reforming of methane and propane (Eqs. 1.3 and 1.4) with CO_2 and followed water-gas shift reaction have received considerable attention [44, 41]. A major disadvantage of dry reforming is the tendency for carbon deposition leading to catalyst deactivation. Laosiripojana et. al [33] reported the investigation of Sodesawa et al. in which the dry reforming (DR) of methane with CO_2 over several catalysts at a stoichiometric reactant feed ratios and due to carbon deposition most of catalysts were deactivated. Halliche et al. [24] however suggested that carbon formation could be avoided by using excess carbon dioxide in the range of 3:1 to 5:1 with respect to methane over Ni/Al_2O_3 catalyst.

$$CO + H_2O \leftrightarrow CO_2 + H_2 \; [\Delta H^o_{298K} = -42.1\,\text{kJmol}^{-1}] \tag{1.5}$$

$$CH_4 + H_2O \leftrightarrow CO + 3H_2 \; [\Delta H^o_{298K} = +206\,\text{kJmol}^{-1}] \tag{1.6}$$

1.3.2 Partial Oxidation (POX)

In this case, hydrocarbon fuel is partially oxidized to syngas in presence of air or oxygen. The oxidation reaction results in heat generation, since $\Delta H_r < 0$ and hence, the reaction is exothermic in nature. Partial oxidation reactions are preferred than direct-oxidation, since direct-oxidation reaction is difficult to study because of excess reactor temperatures, which can destroy reactor. The reactants feed in direct oxidation is flammable and proper care is required so that the inlet composition does not fall

into flammable limits of hydrocarbon fuel, for example, in propane-air mixture, lower flammable limit (LFL) and upper flammable limit (UFL) of propane are 2.15% and 9.60%. That means between LFL and UFL of propane, the mixture is combustible whereas beyond these limits, combustion will not occur. Therefore, fuel air mixture is diluted with nitrogen gas in order to avoid explosion.

The general partial oxidation reaction of a hydrocarbon fuel can be expressed as

$$C_mH_n + yO_2 \rightarrow aH_2 + bCO + cCO_2 + dCH_4 + eH_2O \tag{1.7}$$

for example,

$$C_3H_8 + 3O_2 \rightarrow \frac{9}{4}H_2 + CO + CO_2 + CH_4 + \frac{3}{2}H_2O \tag{1.8}$$

1.3.3 Steam Reforming (SR)

The steam reforming reaction may be described by the general reaction:

$$C_mH_n + mH_2O \rightarrow (m + \frac{n}{2})H_2 + mCO + oH_2O + HCs \tag{1.9}$$

for example,

$$C_3H_8 + 3H_2O \rightarrow 7H_2 + 3CO \tag{1.10}$$

The CO formed may take part in two further reactions, the water-gas shift reaction:

$$CO + H_2O \rightarrow CO_2 + H_2 \, [\Delta H^o_{298K} = -42.1\,\text{kJmol}^{-1}] \tag{1.11}$$

and the methanation reaction:

$$CH_4 + H_2O \leftrightarrow CO + 3H_2 \, [\Delta H^o_{298K} = +206\,\text{kJmol}^{-1}] \tag{1.12}$$

The overall product gas is a mixture of carbon monoxide, carbon dioxide, hydrogen, and unconverted methane and water. Steam reforming is probably the most common method for hydrogen production in chemical industries [57]. Although relatively high concentrations of hydrogen are produced from SR as

compared to DR and POX reforming routes, this process is mostly suited for long periods of steady-state operation. In addition, larger reactors are required because of its highly endothermic nature ($\Delta H_r > 0$) for the purpose of supplying heat in the form of steam. Steam reforming of hydrocarbons is performed at higher H/C (hydrogen in steam to carbon present in fuel) ratios, typically between 1 and 3, in order to reduce the risk of carbon deposition.

1.3.4 Autothermal Reforming (ATR)

The autothermal reforming reaction may be described by the general reaction:

$$C_mH_n + aO_2 + bH_2O \rightarrow dCH_4 + eCO + fCO_2 + gH_2 + hH_2O \tag{1.13}$$

for example,

$$C_3H_8 + 3O_2 + 3H_2O \rightarrow CH_4 + CO + CO_2 + 2H_2 + 3H_2O \tag{1.14}$$

Autothermal reforming was developed in the late 1950s so that both the reactions, e.g. POX and SR can be carried out in a single reactor. ATR combines partial oxidation (POX) and steam reforming (SR), in a single process. POX reactions are exothermic (produces heat) while SR reactions are endothermic and heat must be generated external to the reforming process. Other exothermic reactions that may simultaneously occur in ATR include water gas shift (WGS) and methanation reactions as already described in SR. Typically, ATR reactions are considered to be thermally neutral, and therefore, do not produce or consume external thermal energy. Since, the both reactions, SR and POX, take place simultaneously, the reactor design is simpler as compared to conventional steam reformer. Exothermic, endothermic and thermoneutral conditions can be selected by choosing an appropriate ratio of hydrocarbon: oxygen: steam as suggested by Ayebee et. al. [4]. The thermoneutral point can be defined as a point where heat of reaction is zero. Catalysts are commonly used to enhance the reaction rate of the reforming processes at lower temperatures.

1.4 Assessment of Fuel Reforming Approaches

As homogeneous (non-catalytic) fuel reformers are able to operate over a wide range of mixture qualities and are insensitive to elevated temperatures, they represent an attractive alternative to catalytic reforming techniques. In particular, most non-catalytic reactors operate with peak flame temperatures higher

than 1525°C to ensure adequate flame stability and margin from blowout. As is well known, NO_x emissions even for fuel rich perfectly premixed fuel-air flames at 1525°C can exceed the 3 ppm threshold (at 15% O_2) targeted for many new power plants [34]. Catalytic reactors, however, can operate stably with flame temperatures far below 1525°C , offering both reduced NO_x emissions and improved combustor turndown. The presence of a catalyst in fuel reforming processes enables complete combustion at lower temperatures than otherwise possible. Moon et. al [40] suggested that catalytic processes, however, require tightly controlled operating conditions and fuel quality to prevent degradation due to excessive temperatures and catalyst poisoning by sulfur compounds. On the other hand, non-catalytic fuel reformers do not rely on catalytically active surfaces and thus are not susceptible to poisoning and temperature-related deterioration [47].

1.5 Fuel Selection

The primary fuels of interest include oxygenated hydrocarbon fuel such as glycerol and gaseous hydrocarbon fuel such as propane. In the present study, propane because of its easy testing is used as a gaseous hydrocarbon fuels in order to investigate detailed characterization of reforming conditions, for example, temperature range and reforming routes. The choice of propane, C_3H_8 (LHV 46.35 MJ/Kg) for initial studies is based on its high potential as hydrogen carrier for future power applications [31]. Propane has more stored energy per unit volume and thus releases more heat when the same amount of propane is burned as compared to methane. It also contains four diatomic hydrogen atoms which is higher when compared to methane. Moreover, propane has a higher boiling point (-42 ºC) than methane (-164 ºC), so it can be liquified even at low pressures i.e. at 9 bar, and hence is easier to store and transport [57]. Long-term, experiments will be conducted with glycerol in order to test the fuel flexibility of CSB reactor. The choice of glycerol, $C_3H_8O_3$ (LHV 16.0 MJ/Kg), a byproduct of bio-diesel production, is based on its excellent potency for H_2 production. National Bio diesel Board in 2006 estimated that only in the US, bio-diesel production has increased dramatically from 500,000 gallons in 1999 to 70 million gallons in 2005. According to Gupta et al. [11] the US bio-diesel production has a potential production of almost 850 million gallons per year. For every 9 kg of bio-diesel produced, about 1 kg of a crude glycerol by-product is formed. Glycerol is a potential feedstock, for hydrogen rich syngas production because one mole of glycerol can produce up to four moles of hydrogen.

1.6 Structure of this Thesis

The present research focuses on the development of a laboratory scale conical spouted bed (CSB) reactor for the purpose of producing hydrogen rich syngas from a variety of fuel feed including liquid biomass such as glycerol and hydrocarbon fuels. The work towards this goal divides into three phases: the cold flow model facility in the first phase (Chapter 2) deals with the study of hydrodynamic behavior of a CSB reactor, the second phase (Chapter 4) involves a simpler plug flow reactor facility which is used for an evaluation of favorable operating conditions for hydrogen rich syngas generation. The plug flow reactor allows for a detailed characterization of reforming conditions in terms of temperature and gasification regime, i.e. dry reforming (DR), partial oxidation (POX), steam reforming (SR) and auto-thermal reforming (ATR). For validation purposes, first experiments will use propane as a supplying fuel, while additional tests will use glycerol as a renewable fuel source. In both cases, the selection of operating conditions is guided by results from thermodynamic analysis. Thermodynamic predictions (Chapter 3) is evaluated using experimental results. Tests from the plug flow reactor are used to assess the efficiency of the reforming process in terms of temperature range, water to fuel ratio, and oxygen to fuel ratio. Results from this study will lay the foundation for follow-up research, where similar tests will be performed in third phase for a bench top CSB reactor facility for syngas production.

Chapter 2 deals with the cold flow hydrodynamic studies. The main purpose of studying cold flow model of conical spouted bed system is to investigate the hydrodynamic behavior of a small, laboratory scale, conical spouted bed (CSB) by considering the effect of specific system parameters (stagnated bed height, particle size and inlet diameter) on minimum spouting velocity $(u_{ms})_o$, stable operating pressure drop (ΔP_{ms}) and maximum pressure drop (ΔP_M). Knowledge of the minimum spouting velocity (u_{ms}) is of fundamental importance in the design and operation of spouted beds. Minimum spouting velocity and pressure drop over the bed are major parameters for a spouted bed system, which are used for sizing of bed dimensions and selection of auxiliary equipment. Most of the work presented in Chapter 2 is published in literature [50].

Chapter 3 provides a thermodynamic equilibrium analysis of homogeneous DR, POX, SR and ATR of propane for qualitative predictions. Thermodynamic equilibrium calculations provide information that is useful for the assessment of a combustion process as well as a valuable tool to obtain some insights into

the potential of non-catalytic reforming. Equilibrium calculations use an idealized thermodynamic state with maximum entropy to predict the composition of the reacted mixture. This state requires infinite residence time for all chemical reactions to complete, which in actual practice it is not feasible. Therefore, it restricts equilibrium calculations to qualitative predictions. The thermodynamic equilibrium solver is used as a reference tool to qualitatively choose operating conditions such as pressure, temperature and reactants feed ratio irrespective of reaction kinetics, reactor design and operation.

Chapter 4 is devoted to the experimental setup which describes in detail the experimental apparatus as well as method to study non-catalytic thermochemical energy conversion routes from propane. This chapter also focuses on results and discussion for experimental data obtained for homogeneous (non-catalytic) DR, POX, SR and ATR. The experimental data is quantitatively obtained from the gas chromatography system. The data includes product species concentration for major as well as minor species. It also includes performance evaluation in terms of efficiencies for DR, POX, SR and ATR processes. These efficiencies include propane conversion, hydrogen generation and carbon monoxide generation efficiencies.

Chapter 6 includes summary, conclusions and recommendations for future work for cold flow studies and homogeneous propane reforming hot flow studies. Chapter 5 includes catalyst selection, its preparation, characterization methods and some preliminary heterogeneous propane reforming test results for ATR process are presented for future scope of the thesis.

Chapter 2
Cold Flow Hydrodynamic Studies

The main purpose of studying cold flow model of CSB is to investigate the hydrodynamic behavior of a small, laboratory scale, conical spouted bed (CSB) by considering the effect of specific system parameters (stagnated bed height, particle size and inlet diameter) on minimum spouting velocity $(u_{ms})_o$, stable operating pressure drop (ΔP_{ms}) and maximum pressure drop (ΔP_M). Experimental results show fair agreement with correlations for $(u_{ms})_o$ available in existing literature. Using experimental data, an alternative correlation for minimum spouting velocity is developed. Improvements of prediction quality are attributed to the inclusion of an additional non-dimensional geometry parameter relating particle diameter to inlet diameter, which is absent from most, previously published correlations. Available experimental data for $(u_{ms})_o$ from tests with small sized CSBs using different particle sizes, inlet diameters and static bed heights show excellent agreement with the proposed correlation.

2.1 Minimum Spouting Velocity

Knowledge of the minimum spouting velocity $(u_{ms})_o$ is of fundamental importance in the design and operation of spouted beds. The minimum spouting velocity is the minimum gas velocity needed to maintain spouting operation. Although CSBs have been actively studied for more than five decades, there is still considerable uncertainty about the method of estimating minimum spouting velocity $(u_{ms})_o$ [3]. The majority of the papers published by previous authors [30, 22, 20, 55, 43, 39], as summarized by Bi H. T. [8], are based on the results of model experiments, where the effect of a single parameter on the minimum spouting velocity was determined. Although the correlations as proposed by these authors are based on limited data, they did provide some guidance for the design of large beds.

With a column diameter of 63.5 mm, the spouted bed used for this study is significantly smaller than the experimental setups used in the available literature. In order to evaluate the applicability and accuracy of existing correlations for small sized conical spouted beds, predictions of these correlations are compared with experimental results; and effects of stagnated bed height, particle size, and inlet diameter are analyzed.

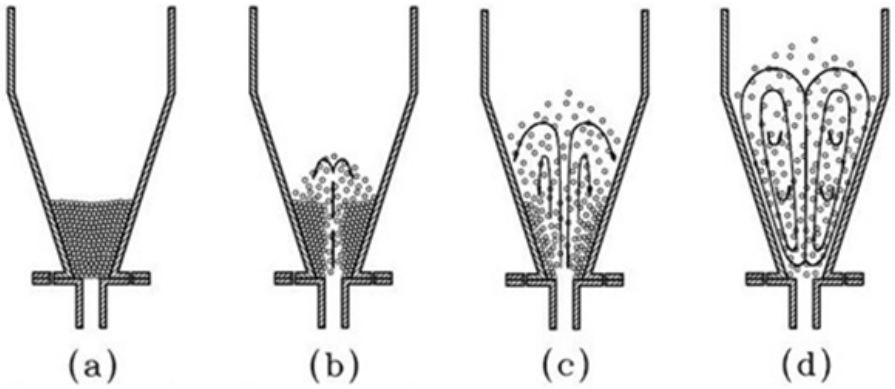

Figure 2.1: Spouting regimes and particle states for different inlet velocities in the conical spouted bed [50]: fixed bed (a), stable spouting operation (b), transition regime (c), and jet spouting (d).

2.2 Conical Spouted Bed (CSB) Reactor

The term 'spouted bed' originates from the characteristic 'spout' that is created by a gas jet entering through a central inlet at the bottom of a conical bed of particles (Figure 2.1). The jet entrains particles, which are carried through the central spout, forming a 'fountain' before being deposited in an annular region. This mechanism creates a regular circulation pattern of particles through the bed. Thus, spouted beds can be classified as a special case within the larger category of fluidized beds.

Spouting operation in spouted beds can be subdivided into several spouting regimes (Figure 2.1). For low inlet flow velocities, the bed remains fixed (Figure 2.1a). An increase of the gas velocity above a threshold value establishes stable spouting operation (Figure 2.1b). Once established, spouting operation continues even below the initial threshold due to a hysteresis effect. A second, lower threshold is found by decreasing the inlet velocity until the internal spout collapses, which determines the 'minimum spouting velocity' $(u_{ms})_o$. At high gas velocities, annular and spout zones become progressively less pronounced (Figure 2.1c), before they can no longer be differentiated in jet spouting (Figure 2.1d). The conical spouted bed reactor schematic is shown in Figure 2.2 which will eventually be used in the third phase of the thesis.

2.3 Experimental Apparatus

Figure 2.3 illustrates the geometry of the conical spouted bed, whereas geometric parameters, physical properties and operating conditions are listed in Table 2.1. A schematic for the experimental setup is shown in Figure 2.4. Compressed air at 293.15K is passed through a receiving manifold, silica desiccant,

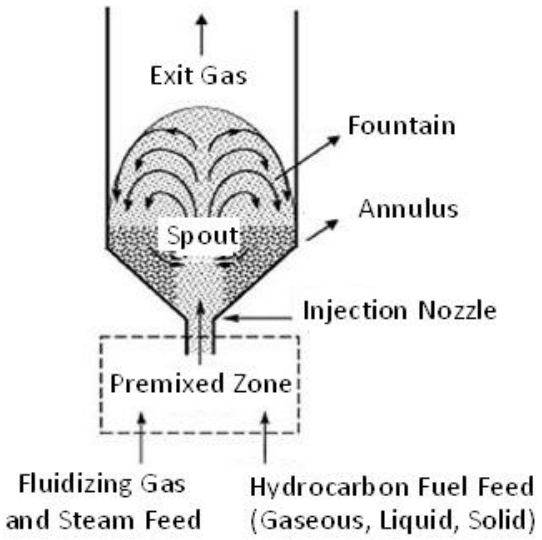

Figure 2.2: Conical spouted bed reactor schematic

and manual control valve before entering the conical contactor. The gas inlet is located at the bottom of a conical contactor manufactured using a 3D printer, where inlet diameters were 6.35 mm, 4.572 mm and 3.302 mm, respectively. The upper part of the setup is formed by a transparent plexiglass cylindrical column with a diameter of 63.5 mm. Aluminum oxide particles with two different mean diameters (0.483 mm and 1.092 mm) were used as bed material. The stagnated bed heights ranged between 10 mm and 65.27mm.

In preliminary testing, two conical contactors with cone angles of 30° and 60° were evaluated. While minimum spouting velocities were found to be lower for the 30° cone, spouting operation was found to be unstable. This observation is in agreement with published results suggesting optimum CSB cone angles between 40° and 60° [60]. All results reported in the present study were obtained for a 60° cone angle.

Experiments were performed by following standard procedure as documented in literature [17]. A weighed charge of bed material was loaded into the conical contactor from the top of the cylindrical column. Prior to recording data, the charge was vigorously moved by the inlet air supply at a velocity at which no entrainment was observed. A uniform bed was obtained when the air flow was abruptly stopped, after which the stagnant bed height was recorded. Experiments were conducted by incrementally increasing the velocity of air, in each instance allowing sufficient time to reach a steady state before

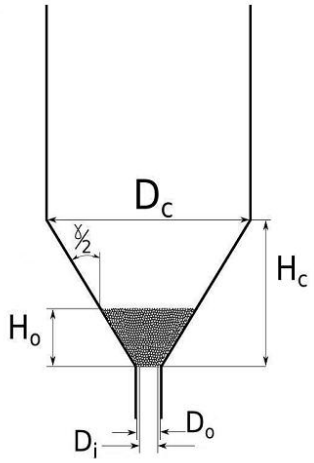

Figure 2.3: CSB geometry parameters

Table 2.1: Range of parameters used for cold flow hydrodynamic study

Parameters	**Symbol**	**Range**	**Units**
Particle diameter	d_p	0.483, 1.092	mm
Inlet air pipe diameter	D_o	3.302, 4.572, 6.35, 9.525	mm
Cone upper part diameter	D_c	63.5	mm
Cone lower part diameter	D_i	3.302, 4.572, 6.35, 9.525	mm
Column diameter	D_c	63.5, 69.85	mm
Cone height	H_c	50.8, 58.53, 61.57, 114.55, 115.6	mm
Cone angle	γ	30, 60	degree
Stagnated bed height	H_o	10 ~ 50, 13.81 ~ 32.82, 35.20 ~ 65.23	mm
Minimum spouting velocity at Do	$(u_{ms})_o$	2.96 ~ 61.93	m/s
Reynolds number at minimum spouting	$(Re_{ms})_o$	93.84 ~ 4433.73	-
Archimedes number	Ar	15885 ~ 183577	-
Density of particles	ρ_p	3960	kg/m^3
Density of air	ρ	1.184	kg/m^3
Viscosity of air	μ	$1.81 * 10^{-5}$	Pa.s
Bed voidage at stagnated bed height	ε_o	0.707 ~ 0.896	-

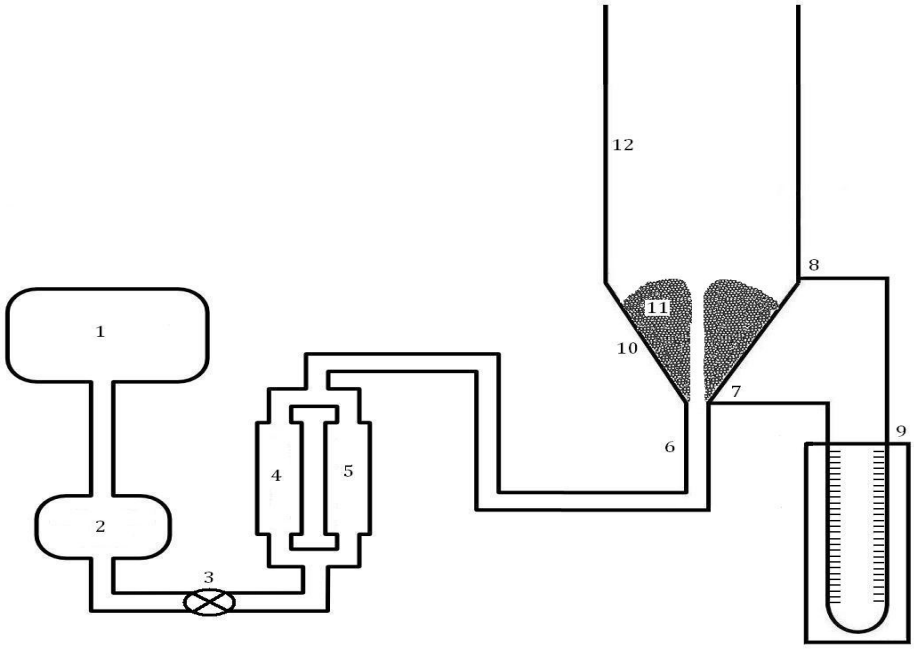

Figure 2.4: Schematic of CSB cold model setup.

rotameter and manometer readings were recorded. The flow rate of gas was gradually increased until steady spouting operation was established, after which the flow rate was gradually decreased to a minimum value where a slight reduction in flow rate caused the spout to collapse, which marked the minimum spouting velocity $(u_{ms})_o$. The same process was repeated for different stagnant bed heights, particle sizes and inlet diameters of the spouted bed. Using up to four trials per test, results proved to be highly repeatable, yielding identical results for typical velocity increments of 0.4-0.8 m/s. In Figure 2.4, different parts are shown such as: (1) air manifold, (2) air filter (3), control valve, (4/5) rotameters, (6) air inlet pipe, (7/8) pressure taps at bed inlet and outlet, (9) U-tube manometer, (10) conical contactor, (11) bed material, and (12) cylindrical column.

2.4 Results and Discussion

2.4.1 Evolution of Spouting Regimes

The evolution of pressure drop for decreasing inlet air flow velocity is illustrated in Figure 2.5a [28]. The minimum spouting velocity $(u_{ms})_o$ is correlated to the steep pressure increase at the transition from spouted bed to fixed bed, which in figure 2.5a is located at $(u_{ms})_o$ equals to 6.99 m/s. Additional results

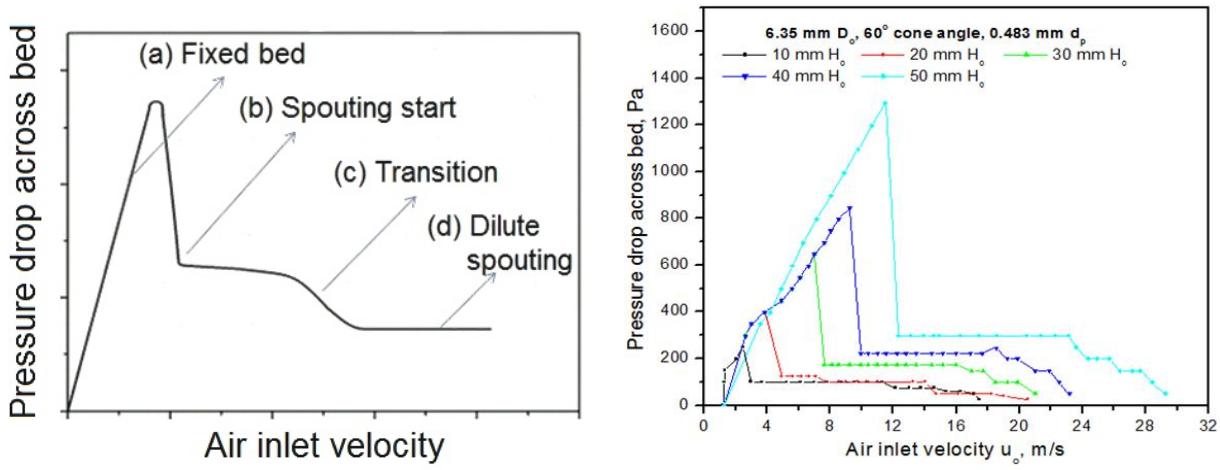

(a) Typical pressure drops for different spouting regimes (b) Evolution of pressure drop for decreasing inlet velocity

Figure 2.5: Pressure drop variations with inlet air flow.

of interest are pressure drop at stable spouting operating (ΔP_{ms}), and maximum pressure drop (ΔP_M) across the fixed bed. Figure 2.5b shows pressure drop vs. air inlet velocity for stagnated bed heights H_o ranging between 0.01 m and 0.05 m. The overall trends of the pressure drop curves are similar to the schematic shown in Figure 2.5a. Results reveal that both minimum spouting velocity and maximum pressure drop increase with increasing stagnated bed height.

2.4.2 Effect of Stagnated Bed Height, Inlet Diameter and Particle Size on $(u_{ms})_o$

Figure 2.6 shows an overview of experimental results from a 60° conical spouted bed for six data sets, defined by a test matrix with two particle mean diameters (0.483 mm and 1.092 mm) and three inlet diameters (6.35 mm, 4.572 mm and 3.302 mm). The minimum spouting velocity $(u_{ms})_o$ shows a linear increase with increasing stagnated bed height (H_o). Moreover, $(u_{ms})_o$ increases for increasing particle size (d_p), whereas it decreases for increasing inlet diameter (D_o). Results are in agreement with previous experimental work of Olazar [42, 43], Bi H. T. [9, 8]. Preliminary testing with a cone angle of 30° suggested that the minimum spouting velocity decreases with decreasing cone angle, which is in agreement with published experimental work by Bi. H. T. [9, 8] and Olazar et al. [42].

2.4.3 Evaluation of Correlations for Minimum Spouting Velocity

Most of the correlations available in the literature [9, 18] are based on results from conical spouted beds that are significantly larger than the system investigated in this study. Table 2.2 presents bed geome-

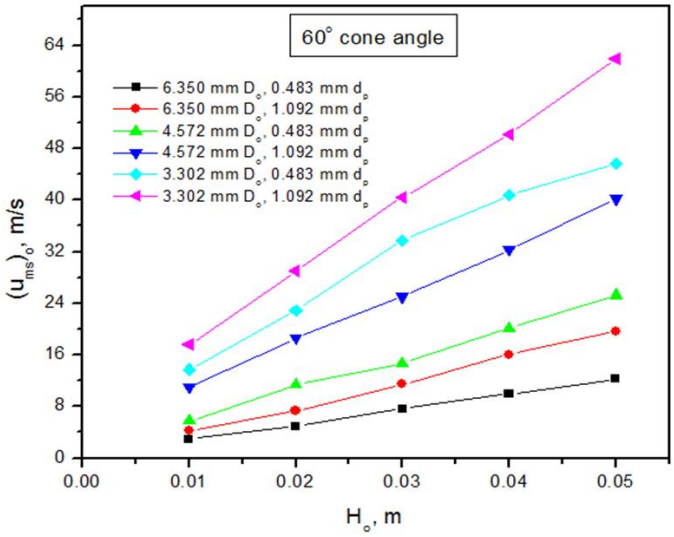

Figure 2.6: Effects of inlet diameter (D_o) and particle size (d_p) on minimum spouting velocity $(u_{ms})_o$.

Table 2.2: Summary of operating parameters used previously and in the present study

Source	Particle size (mm)	D_o (mm)	D_c (mm)	D_i (mm)	γ (deg)	H_o (mm)	H_o/D_o
Markowski [10]	3.41 ~ 10.35	5.6 ~ 300	300 ~ 1100	5.6 ~ 300	37	3.36 ~ 690	0.6 ~ 2.3
Olazar [12]	0.95 ~ 25	30 ~ 60	360	60	28 ~ 45	70 ~ 300	0.33 ~ 6.67
Bi et al. [13]	1.16	12.7 ~ 25.4	65 ~ 95.8	38.1	30 ~ 60	80 ~ 335	3.15 ~ 26.38
Choi [18]	2.1 ~ 2.8	21 ~ 35	240 ~ 450	38	60	240 ~ 400	6.86 ~ 19.05
Present Study	0.483, 1.092	3.3 ~ 9.53	63.5 ~ 70	3.3 ~ 9.525	30 ~ 60	10 ~ 65	3.03 ~ 6.82

Table 2.3: Summary of correlations [9, 18] for calculating $(u_{ms})_o$.

Source	Correlation	Eqn.
Markowski (1983)	$(Re_{ms})_o = 0.028 Ar^{0.57} (H_o/D_o)^{0.48} (D_c/D_o)^{1.27}$	(2.1)
Choi (1992)	$(u_{ms})_o = \sqrt{2gH_o}\, 0.147 (\rho_p - \rho)/\rho)^{0.477} (d_p/D_c)^{0.61} (H_o/D_c)^{0.508} (D_o/D_c)^{0.243}$	(2.2)
Gorshtein (1964)	$(Re_{ms})_o = 0.174 Ar^{0.5} [1 + 2\tan(\gamma/2)(H_o/D_o)]^{0.25} \tan(\gamma/2)^{-1.25}$	(2.3)
Mukhlenov (1965)	$(Re_{ms})_o = 3.32 Ar^{0.33} (H_o/D_o) \tan(\gamma/2)^{0.55}$	(2.4)
Tsvik et al. (1967)	$(Re_{ms})_o = 0.4 Ar^{0.52} (H_o/D_o)^{1.24} \tan(\gamma/2)^{0.42}$	(2.5)
Olazar et al. (1992)	$(Re_{ms})_o = 0.126 Ar^{0.5} (D_b/D_o)^{1.68} \tan(\gamma/2)^{-0.57}$, $d_p > 1$ mm	(2.6)
Olazar et al. (1996)	$(Re_{ms})_o = 0.126 Ar^{0.39} (D_b/D_o)^{1.68} \tan(\gamma/2)^{-0.57}$, $d_p \leq 1$ mm	(2.7)
Bi et al. (1997) (for $D_b/D_o \geq 1.66$)	$(Re_{ms})_o = [0.30 - 0.27/(D_b/D_o)^2] \sqrt{Ar (D_b/D_o) [(D_b/D_o)^2 + (D_b/D_o) + 1]/3}$	(2.8)

try and particle size for comparable studies [39, 43, 9, 13]. Furthermore, Table 2.3 lists eight correlations predicting $(u_{ms})_o$ in CSBs.

Equations (2.1) and (2.3) given in Table 2.3 include the column diameter D_c as a parameter. These equations are reported to work well for large beds, while having limitations when used for small beds [9]. Equations (2.3) through (2.8) do not include D_c and are suitable for both small size and large size CSBs, although their accuracy needs further verification [9].

Figure 2.7a shows an overview of predictions from the six best performing correlations compared to experimental results obtained for an inlet diameter of 6.35 mm, a particle diameter of 0.483 mm and various stagnated bed heights. While all correlations display similar trends corresponding to experimental observations, predicted values differ significantly. While some correlations appear to perform well for this particular data set, it will be shown that the performance of the correlations is not independent of the data, i.e. none of the available correlations perform well for all available data.

In order to better illustrate the performance of individual correlations, Figure 2.7b plots predicted $(u_{ms})_o$ as a function of experimental $(u_{ms})_o$ for the same data as shown in Figure 2.7a. Each of the symbols represents predictions from a specific correlation, which is plotted versus data points obtained from experiments. In theory, predictions should match experimental data, i.e. the best performing correlations will align with the diagonal line. Data points below the diagonal reveal correlations that under-predict, whereas data points above the diagonal correspond to correlations that over-predict. In particular, the correlation by Bi, et al. (Eq. 2.8) over-predicts by a relative error (RE) up to 159.4%, whereas the correlation by Olazar (Eqns. 2.6 and 2.7) under-predicts by a RE of -54.5%. In comparison, results from

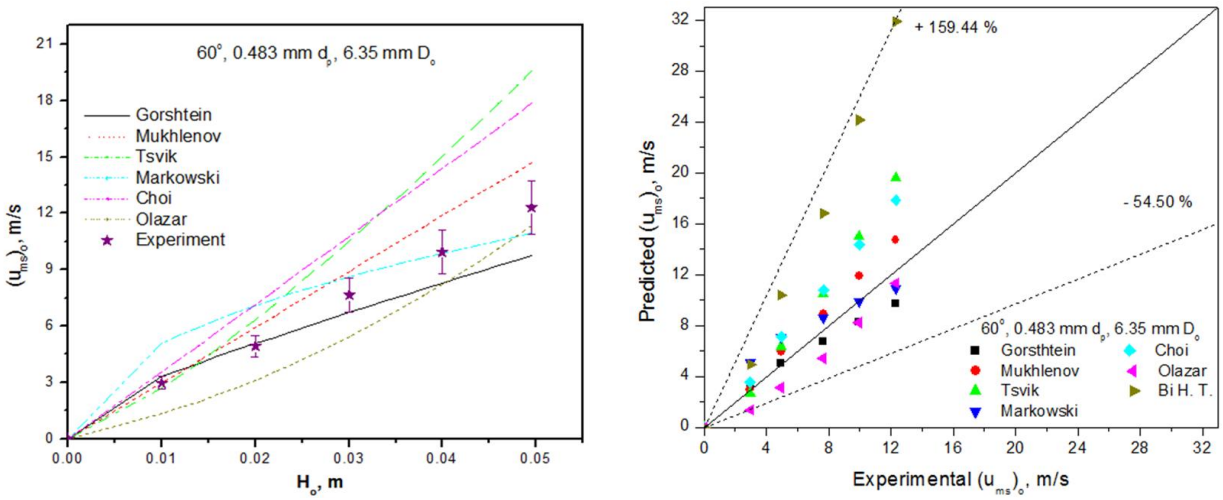

(a) Comparison of experiments and correlations for minimum spouting velocity $(u_{ms})_o$ at varying stagnated bed heights

(b) Comparison of predicted $(u_{ms})_o$ with experimental data; best performing correlations align with the diagonal line

Figure 2.7: Comparisons for minimum spouting velocity among existing correlations and with experimental findings

correlations proposed by Gorshtein (Eq. 2.3) and Mukhlenov (Eq. 2.4) appear to perform reasonably well, whereas Choi (Eq. 2.2) and Tsvik (Eq. 2.5) suggest significant over-predictions.

Figure 2.7 illustrates only one out of a total of six data sets taken for this study, where in the following, the overall performance of each of the individual correlations listed in Table 2.3 is assessed for all available data sets. Similar to Figure 2.7b, predicted $(u_{ms})_o$ are plotted as a function of experimental $(u_{ms})_o$; instead of plotting predictions from multiple correlations for one single data set, predictions from a single data correlation are plotted for all available multiple data sets. A detailed analysis reveals that all of the correlations in Table 2.3 consistently show relative errors (RE) in excess of 50% for selected data points.

Figure 2.8 illustrates that analysis using all available data sets reveal distinct differences with respect to results suggested by Figure 2.7, which were obtained for a single data set. In particular, Figs. 2.8a / 2.8b show that correlations that performed well previously tend to under-predict, whereas Figs. 2.8c / 2.8d indicate that other correlations perform better than expected.

On close inspection, a comparison of minimum spouting velocities for the two different particle sizes reveals that predictions for small particles tend to be higher than for large particles; in addition, results show a significant impact of the inlet diameter, with larger diameters predicting higher values.

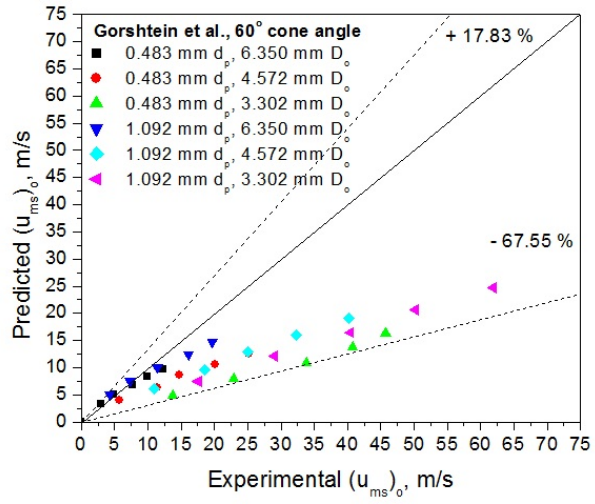

(a) Gorshtein, et al.

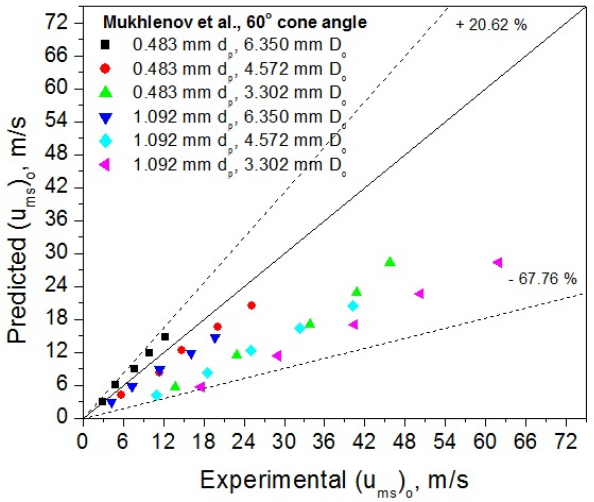

(b) Mukhlenov, et al.

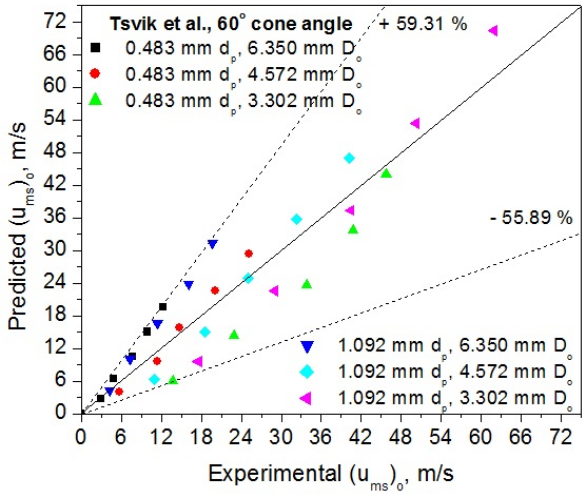

(c) Tsvik, et al.

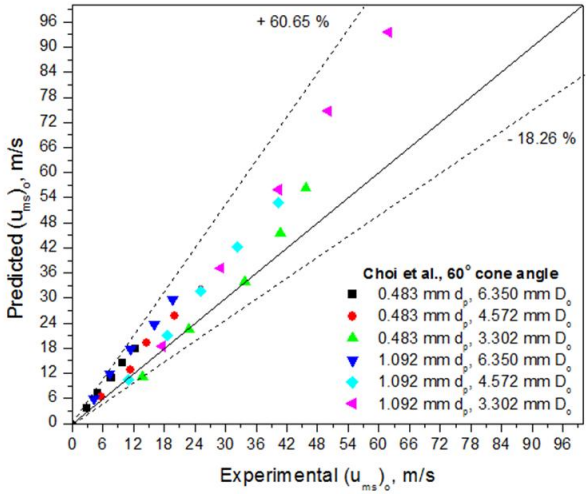

(d) Choi, et al.

Figure 2.8: Comparison of predictions from selected correlations

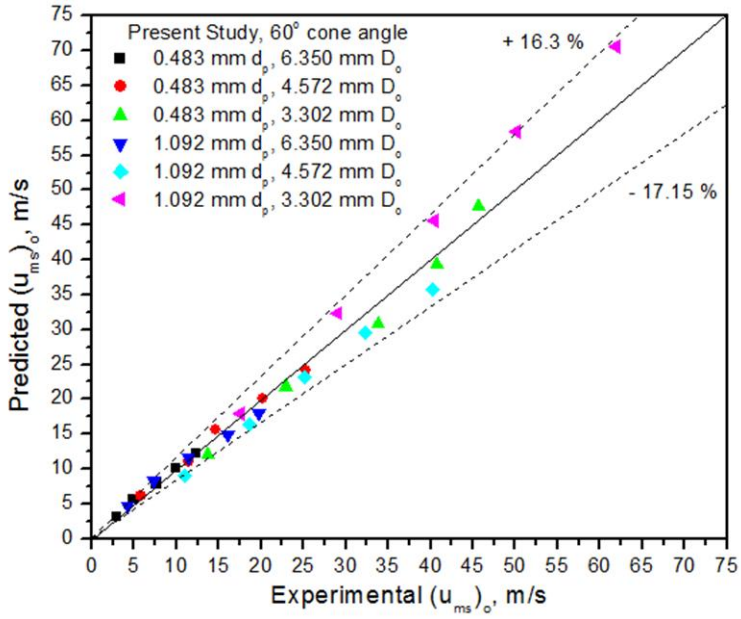

Figure 2.9: Plot for predictions from proposed correlation (eqn. 2.11) for different operating parameters.

While this effect is most obvious in Figs. 2.8b and 2.8c, it is significantly reduced in the correlation by Choi, et al. (2.8d/Eq. 2.2). The improved performance is attributed to the choice of a different set of non-dimensional parameters in comparison to other correlations; all other equations are dependent on the Archimedes number, which ties particle size and density information into a single non-dimensional parameter as

$$Ar = \frac{g\, d_p^3 \rho\, (\rho_p - \rho)}{\mu^2} \tag{2.1}$$

In particular, the ratio of exponents of d_p and ρ_p in the Archimedes number is 3, assuming $\rho_p >> \rho$, whereas it is about 1.28 in Eq. 2.2. Thus, the poor performance of available correlations is attributed to an incomplete set of non-dimensional parameter that separates the particles size d_p from the Archimedes number Ar, which is corroborated by studies by Olazar, et al. [42, 43], who proposed separate exponents of Ar for different particle sizes (Eq. 2.6/2.7). In general, the minimum spouting velocity depends on the geometry of the system defined by stagnated bed height (H_o), particle size (d_p), inlet diameter (D_o), cone angle (γ), column diameter (D_c), and property data for gas and particles. As long as the bed stays entirely in the conical section, results do not depend on D_c [16]. As all data were obtained for a single cone angle, the only parameters affecting the results are H_o, d_p, D_o and property data. A multi-variable regression

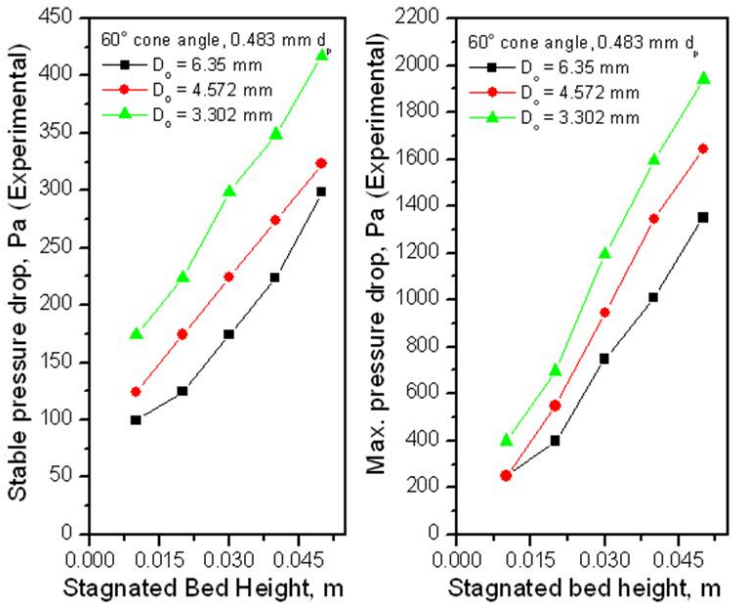

Figure 2.10: Effects of H_o and D_o on stable pressure drops (left plot) and maximum pressure drops (right plot).

for experimentally evaluated Reynolds number $(Re_{ms})_o$ based on the non-dimensional parameters Ar, H_o/D_o, and d_p/D_o yields

$$(u_{ms})_o = f(\mu, \rho, \rho_p, g, D_o, H_o, d_p) \tag{2.2}$$

$$(Re_{ms})_o = 717.26\,(Ar)^{0.08}\,(H_o/D_o)^{0.85}\,(d_p/D_o)^{1.23} \tag{2.3}$$

Where, Reynolds number at minimum spouting can be written as

$$(Re_{ms})_o = \frac{\rho\,(u_{ms})_o\,d_p}{\mu} \tag{2.4}$$

From eqn. 2.3, the minimum spouting velocity can be easily calculated.

Figure 2.9 illustrates that correlation results show excellent agreement with all available data obtained for varying inlet diameters and alumina particle sizes. It is noted that additional tests with particles of different densities and spouted beds with different cone angles are required for the development of a universally applicable correlation for small sized conical spouted beds.

2.4.4 Maximum Pressure Drop ΔP_M and Stable Pressure Drop ΔP_{ms}

In experiments, both peak pressure drop and stable pressure drop increased with increasing stagnated bed height H_o, whereas they increased with decreasing inlet air diameters as can be seen in Figure 10. Both pressure drops, ΔP_M and ΔP_{ms}, were also observed to be higher for larger particle size than for smaller particle sizes.

Stable operating pressure drop ΔP_{ms} and maximum pressure drop ΔP_M have been studied by several researchers, who developed correlations for predicting pressure drops in CSBs [55, 28]. Correlations for ΔP_M perform poorly, which is attributed to large pressure drops that are significantly impacted by inlet design, pressure tap locations and initial state of the bed. While correlations for ΔP_{ms} show better results, a satisfactory analysis of their performance goes beyond the scope of the present study.

2.5 Summary

Minimum spouting velocity and pressure drop over the bed are major parameters for a spouted bed system, which are used for sizing of conical spouted bed (CSB) dimensions and selection of auxiliary equipment. The cold flow conical spouted bed model study presents results for the hydrodynamic behavior of a laboratory scale conical spouted bed. In experiments, minimum spouting velocity $(u_{ms})_o$, pressure drop under stable spouting operating ΔP_{ms} and maximum pressure drop ΔP_M were determined for varying stagnated bed heights (H_o). A test matrix with three different inlet diameters (D_o) and two mean alumina particle sizes (d_p) yielded six data sets. Experimental results verified that $(u_{ms})_o$ increases with increasing particle size (d_p) and increasing stagnation bed height (H_o), whereas it decreases for increasing D_o. A comparison of experimental data to results from correlations for $(u_{ms})_o$ that are available in literature revealed that, while trends were predicted correctly, values showed significant deviations. All available correlations showed relative errors (RE) in excess of 50% for at least one out of the six available data sets. An analysis of the results revealed that predicted values appear to be dependent on the particle size and inlet diameter, which indicates an insufficient number of dimensionless parameters in existing correlation. As an alternative, a simple empirical correlation for $(u_{ms})_o$ was fitted to the six available experimental data sets taken for cold flow study, where an additional non-dimensional parameter relating particle size to inlet diameter was included. While additional tests using varying particle densities and cone angles are required for the development of a universally applicable correlation for

small sized conical spouted beds, results from the new correlation show a drastic improvement of prediction quality. Predicted values show excellent agreement for all available experimental data with varying inlet diameters, particle sizes and stagnated bed heights.

Chapter 3
Thermodynamic Equilibrium Analysis

Thermodynamic equilibrium calculations provide information that is useful for the assessment of a combustion process as well as a valuable tool to obtain some insights into the potential of homogeneous reforming. Equilibrium calculations use an idealized thermodynamic state with maximum entropy to predict the composition of the reacted mixture. This state requires infinite residence time for all chemical reactions to complete, which in actual practice it is not feasible. Therefore, it restricts equilibrium calculations to qualitative predictions. This chapter provides a thermodynamic analysis of non-catalytic DR, POX, SR and ATR of propane for qualitative predictions. The thermodynamic equilibrium calculations are performed utilizing the CANTERA equilibrium solver, involving a non-stoichiometric approach (element potential method), [21]. This tool is capable of modeling problems involving chemical kinetics, thermodynamics, and/or transport processes; in the present study, it is used for equilibrium calculations. Thermodynamic database GRI-Mech 3.0 (a 53 species database) [52] and solid carbon database are used to evaluate the thermodynamic properties of the chemical species considered in the model. The initial amount of propane is assumed to be 1 mol. The primary species involved in propane reforming routes are C_3H_8, H_2, CO, CO_2, CH_4, H_2O, C_2H_2, C_2H_6 and carbon (graphite). However, the most occuring species including H_2, CO, CO_2, CH_4 and carbon together with C_3H_8 are used in both theoretical and experimental studies of the present work. The thermodynamic equilibrium solver is used as a reference tool to qualitatively choose operating conditions such as pressure, temperature and reactants feed ratio irrespective of reaction kinetics, reactor design and operation.

3.1 Operating Pressure and Temperature Selection

The selection of operating pressure for the present investigation of propane reforming is guided by thermodynamic equilibrium approach. Figure 3.1 shows that the effect of pressure on H_2 production efficiency, $\eta_{\mathrm{H_2,prod.}} = \chi_{H_2,prod}/4\times\chi_{\mathrm{C_3H_8,in}}$, in the exhaust gas produced per mole of propane for homogeneous propane reforming processes. The pressure varies from 0.5 ~ 5 atm whereas the temperature lies in the range of 500 ~ 1000º C. It can be seen that the lower pressure favors the formation of H_2whereas the H_2 is significantly reduced with the increase of pressure from 0.5 to 5 atm. In the present study, atmospheric

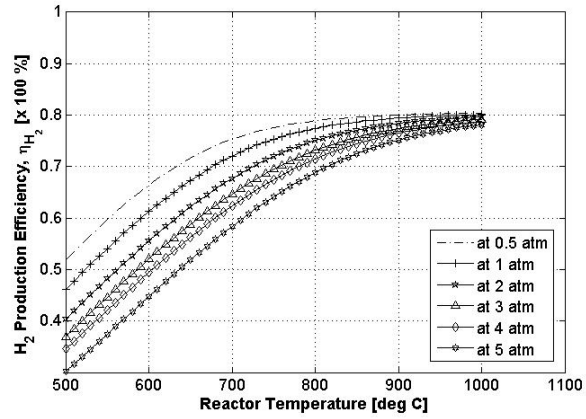

(a) Propane dry reforming.

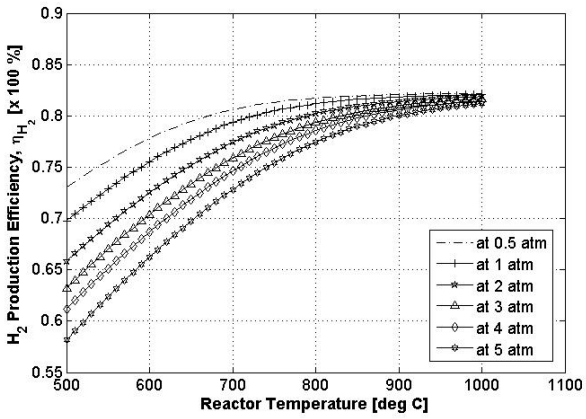

(b) Propane partial oxidation.

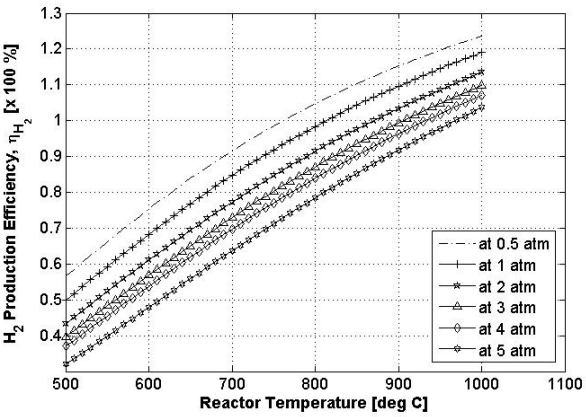

(c) Propane steam reforming

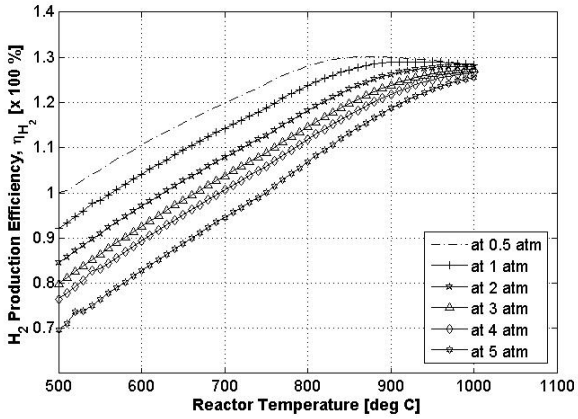

(d) Propane auto-thermal reforming

Figure 3.1: Effect of pressure on H_2 production efficiency during DR, POX, SR and ATR of propane at a specified reactants mole fractions.

pressure is preferred for all experimental tests. This selection is mainly due to the available pyrex glass reactor facility. It is also noted in Figures 3.1a, 3.1b, 3.1c and 3.1d that H_2 increases with the increase of temperature. The reason is that at high temperatures propane dissociates into hydrogen bound species. The temperature range chosen for the present investigation of propane reforming reactions falls in the range of 500 ~ 1000º C. It is noted in Figures 3.1a and 3.1b that maximum H_2 production efficiency for DR is close to that of POX, around 78 ~ 82% for 1 atm pressure and 800 ~ 1000º C. However, H_2 production efficiency for POX reforming always appears higher than DR of propane for the entire temperature and pressure ranges shown.

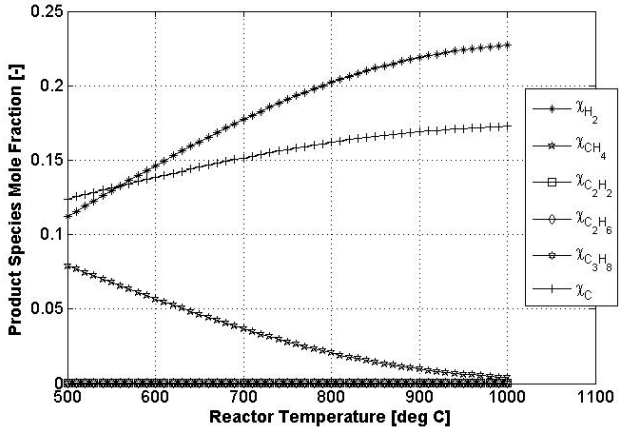

(a) Thermodynamic equilibrium analysis with $\chi_{C_3H_8}$ = 0.09, $\chi_{N_2} = 0.91$ (CPR = 10)

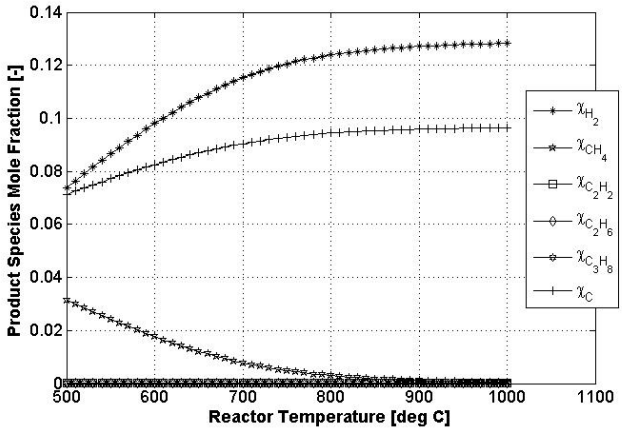

(b) Thermodynamic equilibrium analysis with $\chi_{C_3H_8}$ = 0.04, $\chi_{N_2} = 0.96$ (CPR = 24)

(c) carbon deposits inside the reactor tube at 900º C

(d) carbon deposits inside the reactor tube at 900º C

Figure 3.2: Effects of temperature and carrier to propane gases ratio (CPR) on product species concentration for dry reforming of propane

3.2 Homogeneous Reforming Processes

3.2.1 Dry Reforming (DR)

Two different CPR (career gas to propane ratio) ratios of 10 and 21 are tested for DR of propane. The thermodynamic analysis (Figures 3.2a and 3.2b) for DR of propane reveals that hydrogen concentration (%vol) although increases with temperature, carbon accumulation also significantly increases at all temperatures range. Figures 3.2c and 3.2d provide experimental evidence of carbon formation inside reactor tube at two CPRs of 10 and 24 at 900º C and 1 atm pressure. It is seen that the effect of carbon accumulation is less pronounced for the case of CPR of 24 as compared to CPR of 10. The formation of carbon for DR of propane is attributed to the most probable reactions of propane cracking and carbon formation: $C_3H_8 \rightarrow 4H_2 + 3C$ and $CH_4 \rightarrow 2H_2 + C$ that could lead to carbon formation [32]. It is observed (Figures 3.2a/3.2b) that the H/C ratio varies in the range of 2 ~ 2.65 identical to the ratio mentioned in above reactions. Since insignificant carbon is observed for the case of DR of propane where CPR of 24

(C_3H_8 is diluted with 96 % N_2) is used, further experimental test resits are presented in Chapter 4 of the thesis.

3.2.2 Ternary Reaction Systems (POX, SR and ATR)

A ternary system diagram, also known as Gibbs triangle, is a plot on three variables which sum to a constant. It graphically represents the ratios of three variables as positions in an equilateral triangle. Ternary plots are used in physical chemistry, petrology, mineralogy, metallurgy, and other physical sciences to show the compositions of systems composed of three species. The advantage of using a ternary plot for depicting compositions is that three variables can be conveniently plotted in a two-dimensional graph. Any point within this triangle represents the overall composition of a ternary system at a fixed temperature and pressure. It should be noted that the overall composition (concentrations sum of the three components) must add up to 100%. The concentration of components is determined independently, then check by adding them up to obtain 100%. The concentration of each species is 100% (pure phase) in its corner of the triangle and 0% at the line opposite it. The percentage of a specific species decreases linearly with increasing distance from this corner, as seen in Figure 3.3. By drawing parallel lines at regular intervals between the zero line and the corner, fine divisions are established for easy estimation of the content of a species. For a given point, the fraction of each of the three materials in the composition can be determined by following the path as shown by arrows for composition at point 2 shown in Figure 3.3. The pure components are represented by each corner, for example components A, B and C. Note the numbers 1 - 4 on the diagram. The composition for each of these points is shown below.

1. 60% A, 20% B and 20% C add to 100 % overall composition.

2. 25% A, 40% B, 35% C and their sum is 100%.

3. 10% A, 70% B, 20% C and their sum is 100%.

4. 0% A, 25% B, 75% C and overall sum is 100%.

In the present study, ternary system diagram is used as a convenient way to decide an optimum ratios of reactants mixture which is supplied to the reactor for SR, POX and ATR reactions. The optimum reactants feed ratio is desired in order to carry out propane reforming in carbon free region, since propane has large amount of carbon bound to it. The second reason to choose optimum reactants feed ratio is not to allow temperature change too much in the reaction system. To ensure trouble free operation

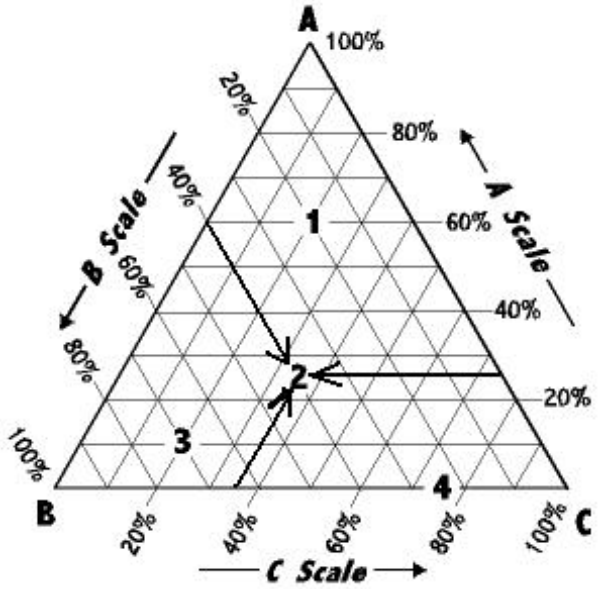

Figure 3.3: Reading a ternary diagram

of the reformer, it is essential to control the soot formation in all process conditions, a thermodynamic equilibrium analysis in context with ternary system is used as a tool to find out an optimum reactants feed ratios at which carbon free reactions are feasible without harming the reaction system. An atmospheric pressure and maximum temperature range (1000º C) conditions are used for all three cases considered here.

Four parameters are selected in order to decide an optimum reactants feed ratios (carrier to propane (CPR), water to propane (WPR) and air to propane (APR) ratios) in a ternary reaction systems including SR, POX and ATR reactions. These parameters inlcude mole fraction of carbon, mole fraction of H_2, mole fraction of CO and ΔT. Since, H_2 and CO are main required species in syngas, these two are selected as qualitative parameters. The reason for selecting carbon is to predict carbon free region whereas ΔT is selected as fourth parameter, since it is not required to change temperature too much.

3.2.3 Steam Reforming (SR) of Propane

Mole fractions of carbon, H_2 and CO are shown in Figures 3.4a, 3.4c and 3.4d respectively whereas ΔT is shown in Figure 3.4b. It can be seen in Figure 3.4a that the amount of carbon increases with an increase in propane supply from 0 to 1 (all values are indicated in mole fractions) and it also increase with the decrease of dilution gas (nitrogen) i.e. maximum C occurs to be 40 % whereas minimum to be 1%. The region of propane supply where carbon appears minimum (carbon free region) is at 0 ~ 10 % of

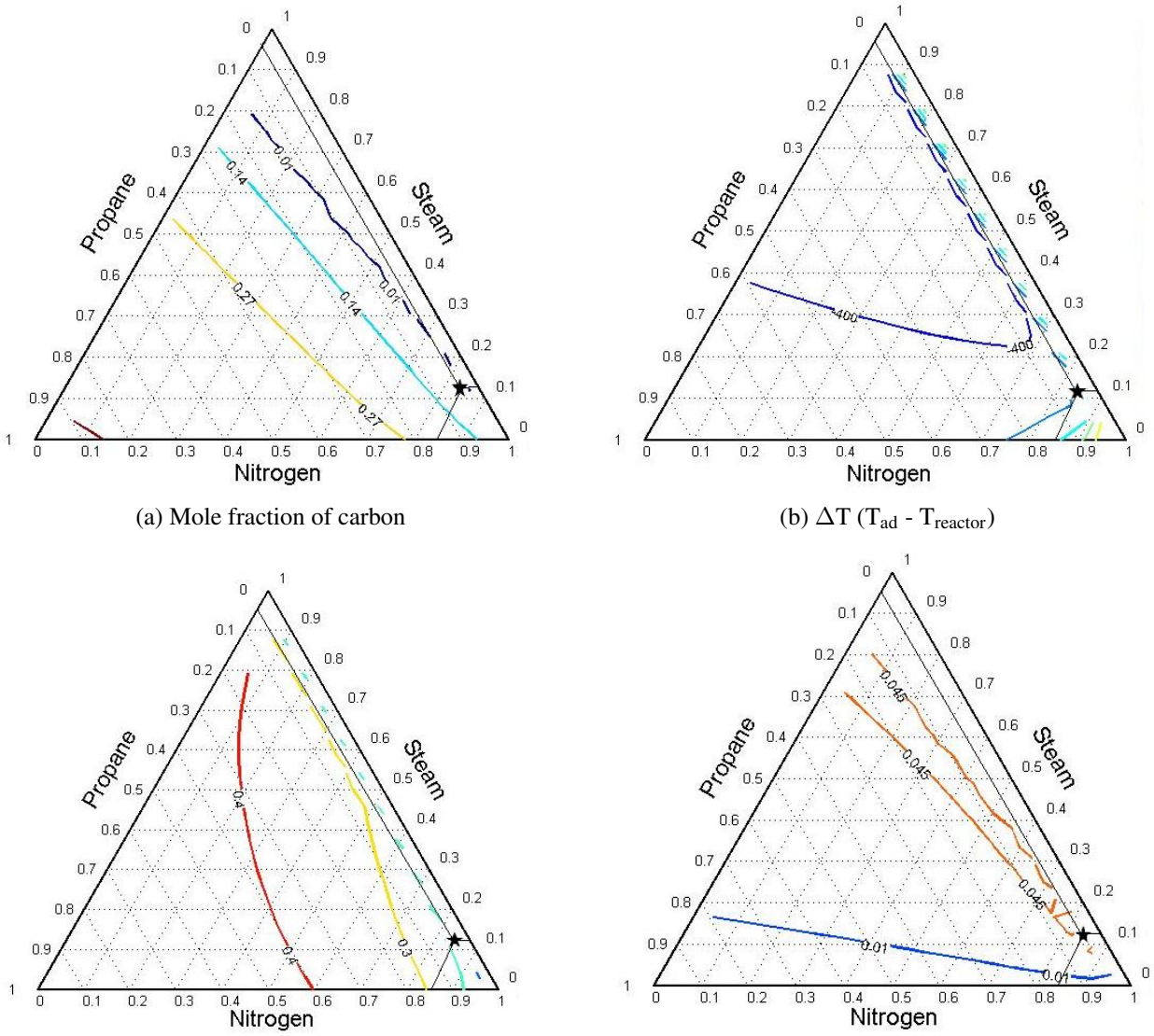

(a) Mole fraction of carbon

(b) ΔT (T_{ad} - $T_{reactor}$)

(c) Mole fraction of H_2

(d) Mole fraction of CO

Figure 3.4: Ternary diagrams for SR of propane.

propane. The reason for this trend is that the propane is dominant reactant species in high carbon region. Large amount of propane in the reactant mixture has tendency of more carbon formation in product stream. However, mole fraction of H_2 is maximum towards the increasing side of propane supply and decreasing side of N_2. Secondly, amount of syngas (mainly H_2 and CO) increases with increase of steam because of methanation reaction ($CH_4 + H_2O \leftrightarrow CO + 3H_2$). Although high amount of steam require higher reactor volume due to higher steam volumetric flow. In addition, higher steam content also consumes higher input heat because of higher vaporization energy.

Also, it can be seen from Figure 3.4b that SR reactions are endothermic, since i.e. ΔT always appears negative i.e. large amount of heat is required to generate steam from water prior going to the reactor. More negative ΔT means more heat is need to supplied. The minimum ΔT appears at 0 ~ 10 % of propane (carbon free region). Due to constraint of available lab built vaporizer system, WPR (water to propane ratio) is limited to 3. In the range of 0 ~ 10 % of propane (carbon free region), H_2 mole fraction appears to be 0.25 (25% volume) and mole fraction of CO appears to be 0.045 (4.5%), which is still plausible amount of hydrogen rich syngas. Therefore, from the above discussion, it is viable to choose reactants ratio as shown in Table 3.1.

3.2.4 Partial Oxidation (POX) of Propane

In this case, there are also four parameters (mole fractions of C, H_2, CO and ΔT as shown in Figures 3.5 a - d, are used to decide optimum reactants feed ratios which include carrier gas to propane ratio (CPR) and air to propane ratio (APR). Since ΔT (Figure 3.5b) is positive, POX of propane is exothermic. Also, it is noted from Figure 3.5a that the carbon formation is highly significant at large amount of propane i.e. close to 40%vol whereas it is almost negligible ($\simeq 1\%$) in the range of 0 to 8% of propane. It could also be noted that in this range of propane, mole fraction of H_2 (Figure 3.5c) is 0.20. Secondly, it is well known that the POX process are highly flammable because the amount of heat release is problematic and it is self-sustained. In order to avoid excess temperature change, the inlet feed composition does not fall into highly flammable limits of hydrocarbon fuel, for example, in propane-air mixture, lower flammable limit (LFL) and upper flammable limit (UFL) of propane are 2.15% and 9.60%. Table 3.1 shows the final optimum reactants feed ratios during which the reaction at specified temperature range occurs in carbon free environment and without any hazard. In the range selected for propane, nitrogen and air, mole fraction of CO is very low i.e. around 4.5 %, which leads to the production of hydrogen rich syngas.

3.2.5 Autothermal Reforming (ATR) of Propane

ATR combines partial oxidation (POX) and steam reforming (SR), in a single process. Exothermic, endothermic and thermoneutral conditions can be selected by choosing an appropriate ratio of propane: air: steam as suggested by Ayebee et al. [4]. The thermoneutral point can be defined as a point where heat of reaction is zero i.e. ΔT is zero. From Figure 3.6b, it can be seen that ΔT is zero at

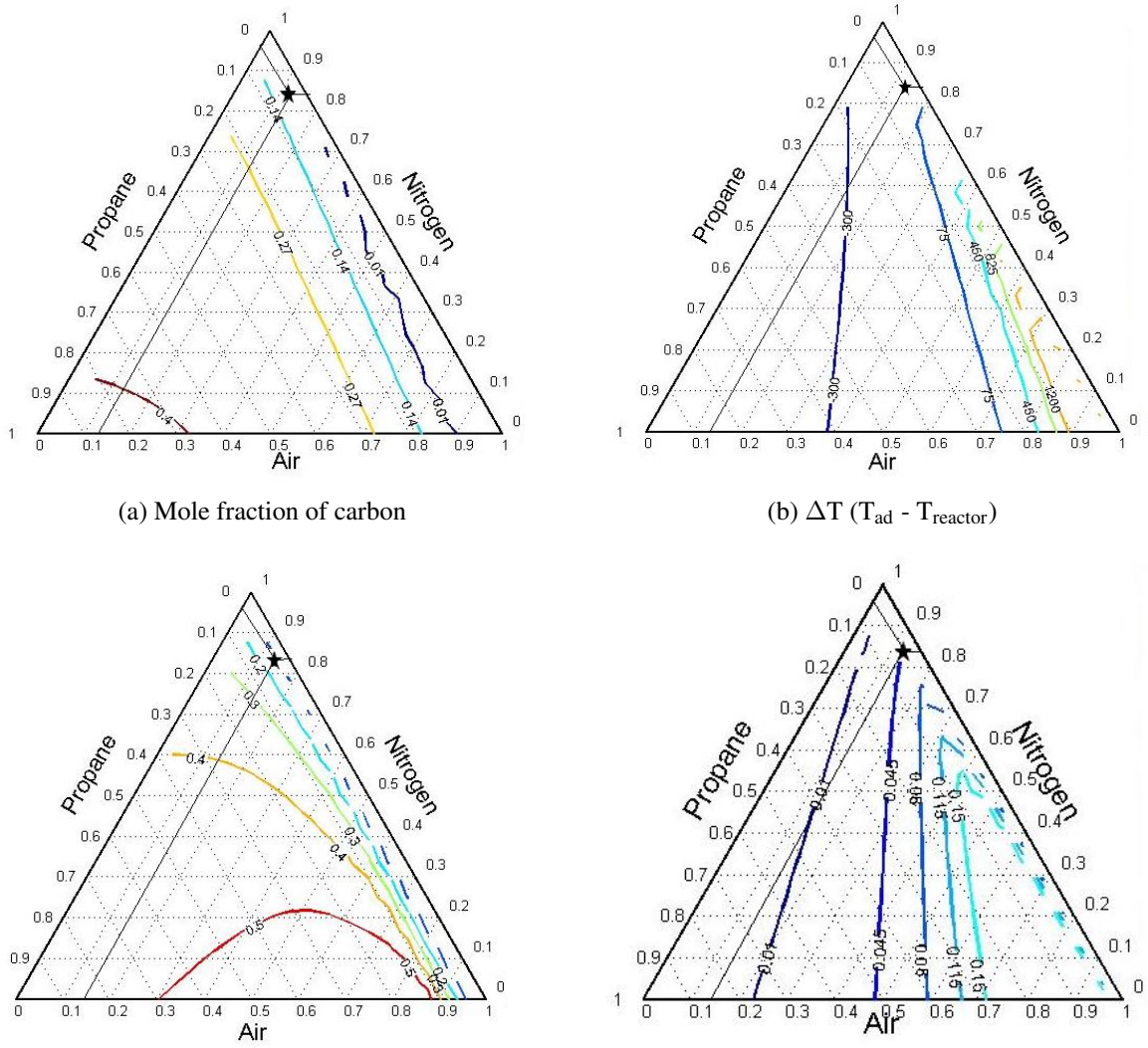

(a) Mole fraction of carbon

(b) ΔT (T_{ad} - $T_{reactor}$)

(c) Mole fraction of H_2

(d) Mole fraction of CO

Figure 3.5: Ternary diagram for POX of propane.

propane feed mole fractions range of 0 ~ 0.1 and also it the range for carbon free reactions, since carbon (Figure 3.6a)appears to be completely zero in this range of propane supply. In this range of fuel, it is also noticed that hydrogen rich syngas can be produced (i.e. $\chi_{H_2} = 0.3$ and $\chi_{CO} = 0.15$, refer Figures 3.6c and 3.6d, respectively). However, for a combination of reactants feed ratios, the optimum ratio appears to be 0.0357/0.8573/0.107 for C_3H_8/Air/H_2O , a ratio of 0.0357/0.107/0.107/0.75 is used for C_3H_8/Air/H_2O/$N_2$by diluting the reactants mixture with 75% N_2.

3.3 Reactants Feed Ratio Selection

The gas residence time (τ_r) of 1.30 s and plug flow reactor volume (V_R) of 0.0107 mm^3 (based on reactor length L_R = 305 mm and diameter D_R = 6.7 mm) are used for all non-catalytic propane reforming reac-

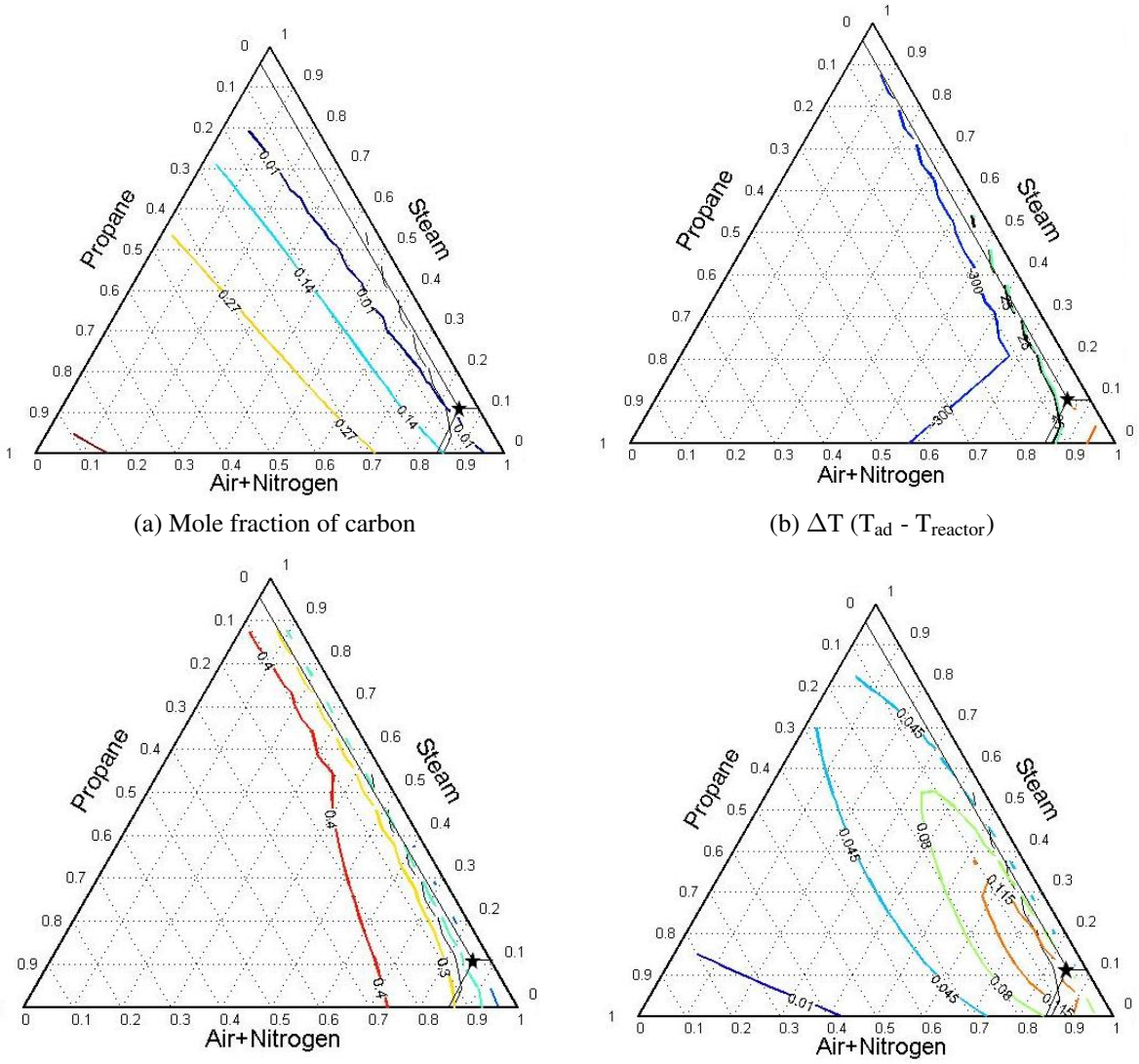

(a) Mole fraction of carbon

(b) ΔT (T_{ad} - $T_{reactor}$)

(c) Mole fraction of H_2

(d) Mole fraction of CO

Figure 3.6: Ternary diagram for ATR of propane.

tions. Correspondingly, GHSV (gas hourly space velocity = $\frac{1}{\tau_r} \times 3600$) and inlet flow rate ($\dot{V} = V_R \times \tau_r$) are 2763.63 $h^{-1}$and $8.25 \times 10^{-6}\,m^3$ (equals 495 mlpm) respectively. The reactants feed ratio i.e. career to propane ratio (CPR) for DR is 24 whereas for all other processes is 21, air to propane ratio (APR) is 3 for all cases whereas water to propane ratio (WPR) for all cases is 3. An atmospheric pressure and the temperatures range for experiments is between 600 ~ 1000º C. An equivalence ratio (φ) for POX and ATR is 1.67 whereas for SR process it is not applicable. The operating parameters including reactants feed ratios, pressure and temperature range selection is tabulated in Table 3.1.

Table 3.1: Operating parameters scheme for homogeneous reforming reactions for propane.

Case	C_3H_8 [%vol]	Air [%vol]	H_2O [%vol]	N_2 [%vol]	CPR	APR	WPR	P [atm]	T [° C]	φ	ΔT [° C]
DR	4.0	-	-	96	24.0	-	-	1	600 ~ 1000	∞	-85 ~ -125
POX	4.0	12.0	-	84	21.0	3.0	-	1	600 ~ 1000	1.67	65 ~ 12
SR	4.0	-	12.0	84.0	21.0	-	3.0	1	600 ~ 1000	N/A	-125 ~ -360
ATR	3.58	10.71	10.71	75.0	21.0	3.0	3.0	1	600 ~ 1000	1.67	-25 ~ -190

Table 3.2: Various efficiency comparisons for homogeneous DR, POX, SR and ATR of propane with their operating conditions mentioned in Table 3.1.

Process	$\eta_{H_2,prod.}$[%]	$\eta_{CO,prod.}$[%]	$\eta_{CH_4,prod.}$[%]	$\eta_{C,prod.}$[%]	$\eta_{C_3H_8,conv.}$[%]
DR	80	0	0.05	80	100
POX	82	35	0.02	48	100
SR	119	45	8	18	100
ATR	128	73	0.01	0	100

3.4 Assessment of Homogeneous Reforming Processes

From the above discussion of DR, POX, SR and ATR, various efficiencies including $\eta_{H_2,prod.}$, $\eta_{CO,prod.}$, $\eta_{CH_4,prod.}$, $\eta_{C,prod.}$ and $\eta_{C_3H_8,conv.}$at 1000° C and 1 atm pressure are tabulated in Table 3.2. It is noted that maximum H_2 production (128%) appears in ATR whereas minimum appears in DR (80%). On the other hand, maximum carbon formation (80%) appears in DR whereas 0% in ATR. A negligible amount of CH_4 (0 ~ 0.05%) occurs in DR, POX and ATR for the reason of methanation reaction ($CH_4 + H_2O \leftrightarrow CO + 3H_2$) in POX and ATR whereas propane cracking reaction ($CH_4 \rightarrow 2H_2 + C$) in DR of propane. It is also noted that propane is completely (100 %) converted to lower hydrogen bound species for all reforming processes. No CO is appeared in DR at all temperatures, since no oxygen bound species are present in the reactants mixture. However, significant amount of CO appears in POX (35%), SR (45%) and ATR (73%) processes for the reason of predominance of methanation reaction over water gas shift reaction ($CO + H_2O \leftrightarrow CO_2 + H_2$) at higher temperatures.

Figures 3.7a, 3.7b, 3.7c and 3.7d show the comparison among DR, POX, SR and ATR processes in terms of ΔT and efficiencies including η_{H_2}, η_{CO} and $\eta_C$for reactant mixtures presented in Table 3.1. The reactions DR, SR and ATR appear endothermic (ΔT is negative) whereas the process POX is exothermic (ΔT is positive) as shown in Figure 3.7a. The reason for this behavior of ΔT is the heat of reaction (ΔH_R); heat is generated for POX whereas heat is consumed during reactions for DR, SR and ATR.

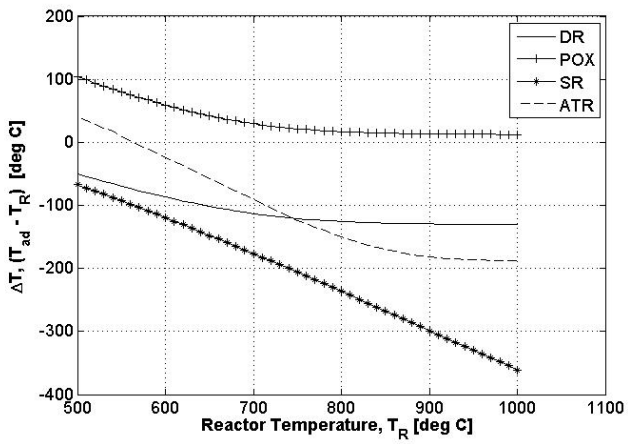

(a) Effect of T_R on ΔT

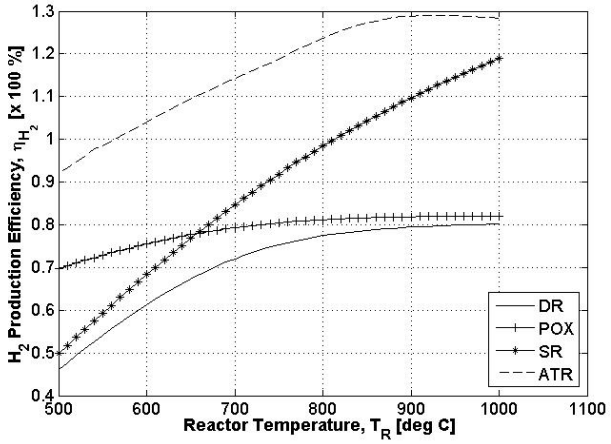

(b) Effect of T_R on $\eta_{|H_2}$

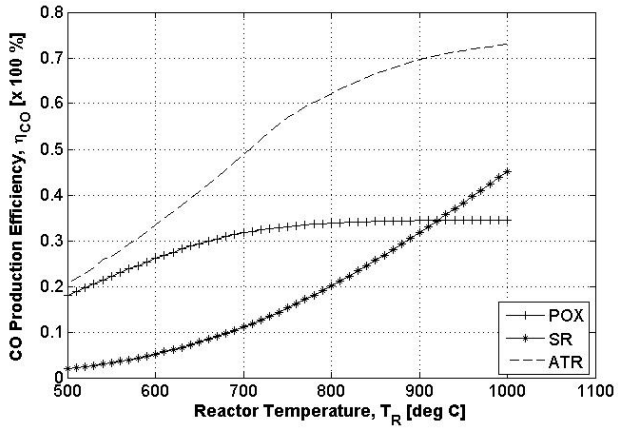

(c) Effect of T_R on $\eta_{|CO}$

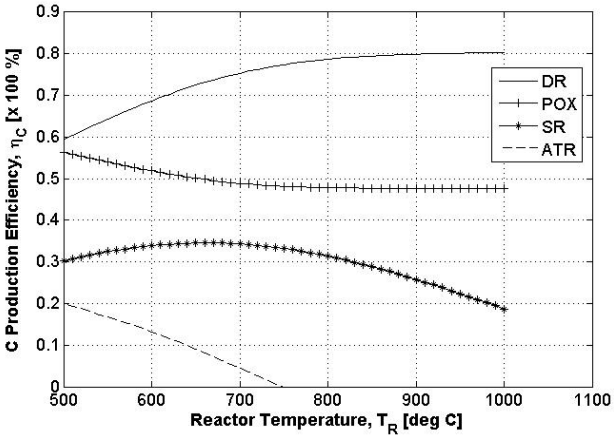

(d) Effect of T_R on $\eta_{|C}$

Figure 3.7: Effect of homogeneous thermochemical conversion routes (with atmospheric pressure and 500 ~ 1000º C reaction temperatures range) of propane on ΔT , $\eta_{|H_2}$, $\eta_{|CO}$ and $\eta_{|C}$ for the reactants feed ratio mentioned in Table 3.1

Figure 3.7b shows the trend of hydrogen production for all reforming processes at temperature range of 500 ~ 1000º C. H_2 increases with temperature for all cases of propane reforming. The corresponding reaction parameters used in each reforming process are mentioned in Table 3.1. It is observed that more hydrogen is produced in SR and ATR as compared to POX and DR as expected. It is observed that the overall production of hydrogen is always higher in ATR ($\eta_{|H_2}$ = 92 ~ 128%) as compared to SR ($\eta_{|H_2}$ = 50 ~ 119%), POX ($\eta_{|H_2}$ = 70 ~ 82%) and DR ($\eta_{|H_2}$ = 48 ~ 80%). The H_2 production efficiency for SR and ATR appears greater than 100% because of addition of H_2 into H_2O. Therefore, the order of H_2 production is ATR >SR >POX >DR.

The CO production efficiency (Figure 3.7c) increases with temperature for POX (18 ~ 35%), SR (2 ~ 45%) and ATR (21 ~ 73%). The increase of CO with temperature for POX, SR and ATR processes is due to the methanation reaction predominance over water gas shift reaction as already discussed earlier. Since no oxygen is present in the reactants mixture for DR, no CO is observed.

Coke formation is a concern in the reforming of hydrocarbon fuels for the production of hydrogen. It is noticed in Figure 3.7d that carbon is increased with temperature for DR whereas decreased with increasing temperature for POX, SR and ATR processes. Carbon formation appears almost constant after 850º C for DR (~ 80%) and PO (~ 48%). The possible reason for carbon presence at high temperature is simultaneous production of carbon along with H_2 production reaction ($CH_4 \rightarrow 2H_2 + C$). On the other hand, the carbon formation continuously decreases for ATR process and vanishes after 730º C temperature. The reason for carbon formation in SR at high temperatures is the solid carbon formation reactions ($CH_4 \rightarrow 2H_2 + C$, $2CO \rightarrow CO_2 + C$, $CO + H_2 \rightarrow H_2O + C$ and $CO_2 + 2H_2 \rightarrow 2H_2O + C$) [59]. It can be concluded that the ATR is most clean process whereas DR is least clean process in terms of carbon formation among all four processes considered in the present study. In other words, the carbon formation increasing order for propane reforming process is ATR< SR< POX< DR.

In addition to hydrogen and carbon species, other major species appeared in the product stream are shown in Figure 3.8. For hydrogen gas production, it is apparent that methane is not a desirable product [57]. Figure 3.8 depicts the product stream main species production as a function of temperature at atmospheric pressure. Higher temperature favors CO production in POX (Figure 3.8b), SR (Figure 3.8c) and ATR (Figure 3.8d) whereas CO_2 and CH_4 production decrease with increase of temperature. The possible reason is that methanation reaction ($CH_4 + H_2O \leftrightarrow CO + 3H_2$) is more predominant as compared to water gas shift reaction ($CO + H_2O \leftrightarrow CO_2 + H_2$) at higher temperature. In DR process (Figure 3.8a), there is no oxygenated species (CO and CO_2) appears, since there is no oxygen present in the reactant stream. Other hydrocarbon species such as C_2H_2 and C_2H_6 are almost negligible in the product stream for all homogeneous reforming processes of propane at all temperatures range.

3.5 Summary

Thermodynamic equilibrium analysis for homogeneous fuel reforming processes Viz. DR, POX, SR and ATR provides information that is useful for the assessment of a combustion process as well as a valuable

tool to obtain some insights into the potential of non-catalytic reforming. Equilibrium calculations use an idealized thermodynamic state with maximum entropy to predict the composition of the reacted mixture. This state requires infinite residence time for all chemical reactions to complete, which in actual practice it is not feasible. Therefore, it restricts equilibrium calculations to qualitative predictions. The thermodynamic equilibrium solver is used as a reference tool to qualitatively choose operating conditions such as pressure, temperature and reactants feed ratio irrespective of reaction kinetics, reactor design and operation.

It was seen in Figure 3.1 in thermodynamic equilibrium analysis of homogeneous propane reforming processes that the lower pressure favors the formation of H_2 . In the present study, atmospheric pressure was preferred for all experimental tests. It was noted that maximum H_2 production efficiency for DR process is close to that of POX, around 78 ~ 82% for 1 atm pressure and 800 ~ 1000º C. However, H_2 production efficiency for POX reforming always appears higher than DR of propane for the entire temperature. A thermodynamic equilibrium analysis in context with ternary system was used as a tool to find out an optimum reactants feed ratios at which carbon free reactions are feasible without harming the reaction system. It was noted in all homogenous reforming processes that the amount of carbon increases with an increase in propane supply from 0 to 1 (in mole fractions) and it also increases with the decrease of dilution gas (nitrogen). The reason for this trend is the dominance of propane in high carbon region. Large amount of propane in the reactant mixture has tendency of more carbon formation in product stream. However, mole fraction of H_2 is maximum towards the increasing side of propane supply and decreasing side of N_2. The amount of syngas (mainly H_2 and CO) was appeared to increase with addition of steam because of methanation reaction ($CH_4 + H_2O \leftrightarrow CO + 3H_2$). Based on the homogeneous thermodynamic equilibrium analysis results, it was concluded that an optimum reactants feed proportions for DR was $\chi_{C_3H_8} = 0.04$, $\chi_{N_2} = 0.96$ and CPR $= 24$ whereas for POX the reactants feed ratios appeared as $\chi_{C_3H_8} = 0.04$, $\chi_{air} = 0.12$, $\chi_{N_2} = 0.84$, CPR $= 21$ and APR $= 3$. Similarly, an optimum reactants feed ratios for SR and ATR were $\chi_{C_3H_8} = 0.04$, $\chi_{H_2O} = 0.12$, $\chi_{N_2} = 0.84$, CPR $=$ 21 and WPR $= 3$ and $\chi_{C_3H_8} = 0.0358$, $\chi_{air} = 0.1071$, $\chi_{H_2O} = 0.1071$, $\chi_{N_2} = 0.75$, CPR $= 21$, WPR $=$ 3 and APR $= 3$ receptively. From the results and discussion for thermodynamic equilibrium analysis, it was noted that maximum H_2 production (128%) appears in ATR whereas minimum appears in DR

(80%). On the other hand, maximum carbon formation (80%) appeared in DR whereas 0% in ATR. No CO was appeared in DR at all temperatures, since no oxygen was present in the reactants mixture. However, significant amount of CO was appeared in POX (35%), SR (45%) and ATR (73%) processes for the reason of predominance of methanation reaction over water gas shift reaction ($CO + H_2O \leftrightarrow CO_2 + H_2$) at higher temperatures. Figure 3.7b showed the trend of hydrogen production for all reforming processes at temperature range of 500 ~ 1000º C. H_2 increases with temperature for all cases of propane reforming. The corresponding reaction parameters used in each reforming process are mentioned in Table 3.1. It was observed that more hydrogen is produced in SR and ATR as compared to POX and DR. It was observed that the overall production of hydrogen is always higher in ATR ($\eta_{|H_2}$ = 92 ~ 128%) as compared to SR ($\eta_{|H_2}$ = 50 ~ 119%), POX ($\eta_{|H_2}$ = 70 ~ 82%) and DR ($\eta_{|H_2}$ = 48 ~ 80%). The H_2 production efficiency for SR and ATR appeared greater than 100% because of addition of H_2in H_2O. Therefore, the order of H_2 production is ATR > SR > POX > DR.

The CO production efficiency (Figure 3.7c) increases with temperature for POX (18 ~ 35%), SR (2 ~ 45%) and ATR (21 ~ 73%). The increase of CO with temperature for POX, SR and ATR processes is due to the methanation reaction predominance over water gas shift reaction. It was noticed in Figure 3.7d that carbon is increased with temperature for DR whereas decreased with increasing temperature for POX, SR and ATR processes. Carbon formation appeared almost constant after 850º C for DR (~ 80%) and PO (~ 48%). The reason for carbon presence at high temperature is simultaneous production of carbon along with H_2 production reaction ($CH_4 \rightarrow 2H_2 + C$). On the other hand, the carbon formation continuously decreases for ATR process and disappears after 730º C temperature. The reason for carbon formation in SR at high temperatures is the solid carbon formation reactions ($CH_4 \rightarrow 2H_2 + C$, $2CO \rightarrow CO_2 + C$, $CO + H_2 \rightarrow H_2O + C$ and $CO_2 + 2H_2 \rightarrow 2H_2O + C$) [59]. It was concluded that the ATR is most clean process whereas DR is least clean process in terms of carbon formation among all four processes considered in the present study. In other words, the carbon formation increasing order for propane reforming process is ATR < SR < POX < DR.

The 100% propane conversion efficiency in thermodynamic analysis for all reforming processes at entire temperature range is attributed to its tendency to its complete break down into hydrogen, carbon and methane along negligible amount of acetylene and ethane even at at temperature 500°C .

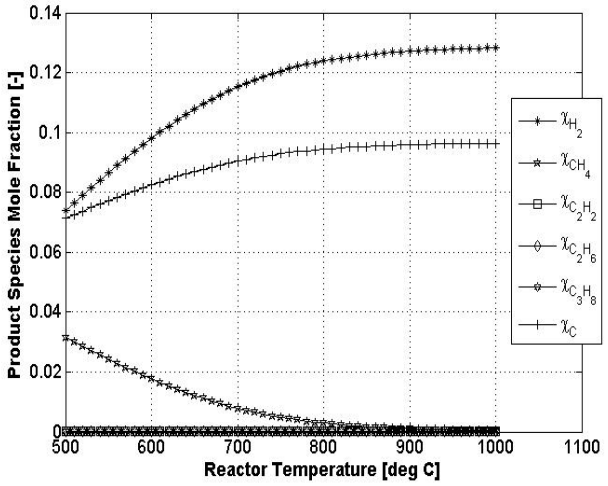

(a) DR

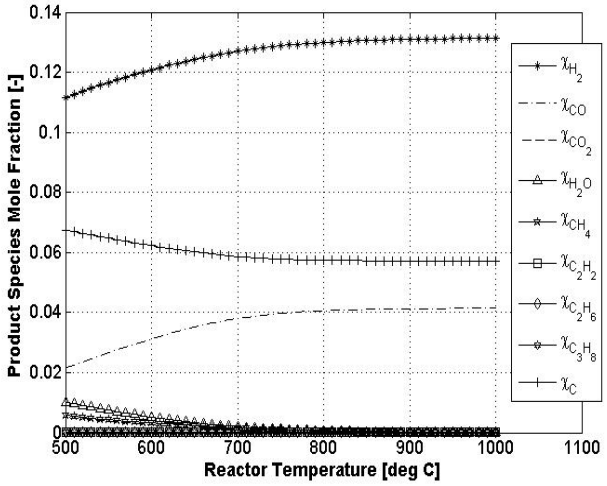

(b) POX

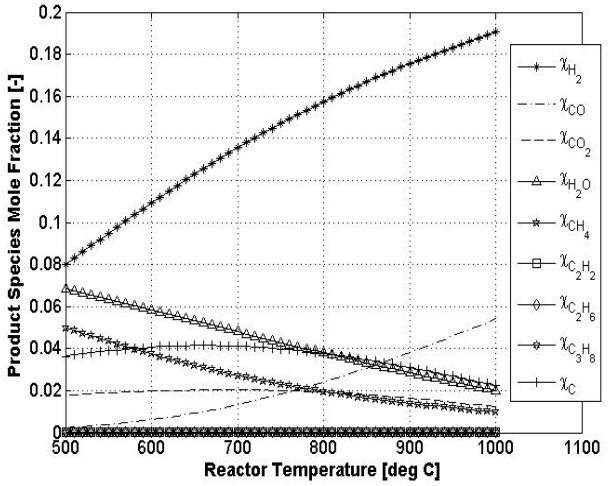

(c) SR

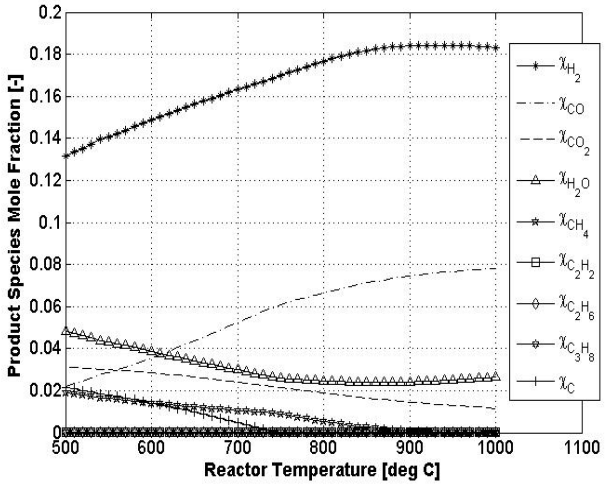

(d) ATR

Figure 3.8: Effect of reactor temperature on product species for homogeneous reformings of propane with operating conditions are mentioned in Table 3.1

Chapter 4
Experimental Results for Homogeneous Fuel Reforming

The development of a CSB reactor, as mentioned earlier in Chapter 1, is divided into three phases: the cold flow model facility in the first phase deals with the study of hydrodynamic behavior of a CSB reactor and the second phase involves a simpler plug flow reactor facility which is used for an evaluation of favorable operating conditions for hydrogen rich syngas production. The plug flow reactor is meant to provide preliminary results that are used to evaluate different reforming approaches, which will eventually be applied in the third phase for the CSB reactor system. The different reforming approaches include dry reforming (DR), partial oxidation (POX), steam reforming (SR) and autothermal reforming (ATR). Tests from the plug flow reactor hot flow studies are used to assess the efficiency of each homogeneous reforming process. Results from this study will lay the foundation for follow-up research in the third phase, where similar tests will be performed for a bench-scale CSB reactor facility for syngas production. The experimental apparatus, product species concentration (vol%) and conversion efficiencies for major species (H_2, CO, C_3H_8 etc.) for homogeneous DR, POX, SR and ATR are discussed in this chapter. A detailed description of experimental method is discussed in Appendix A.

4.1 Experimental Apparatus

The experimental apparatus consists of three main parts: the flow system, reactor and data acquisition system. The flow system provides the feed gases of interest which include propane and nitrogen common to all test cases, whereas air and steam according to test case requirement of POX, SR and ATR. A plug flow reactor is used for all reforming reactions at different set temperatures and at atmospheric pressure conditions, and the data acquisition system collects temperature, emissions data and it also controls the flow rates for feed gases. The same experimental apparatus facilitates both homogeneus and heterogeneous thermochemical conversion processes.

4.1.1 Reactor Set Up for Dry and Partial Oxidation Fuel Reformings

A schematic for the experimental setup for homogeneous dry reforming (DR) and partial oxidation (POX) is shown in Figure 4.1. The reactor unit (Figure 4.1) is set up as a dual-feed system that can deliver

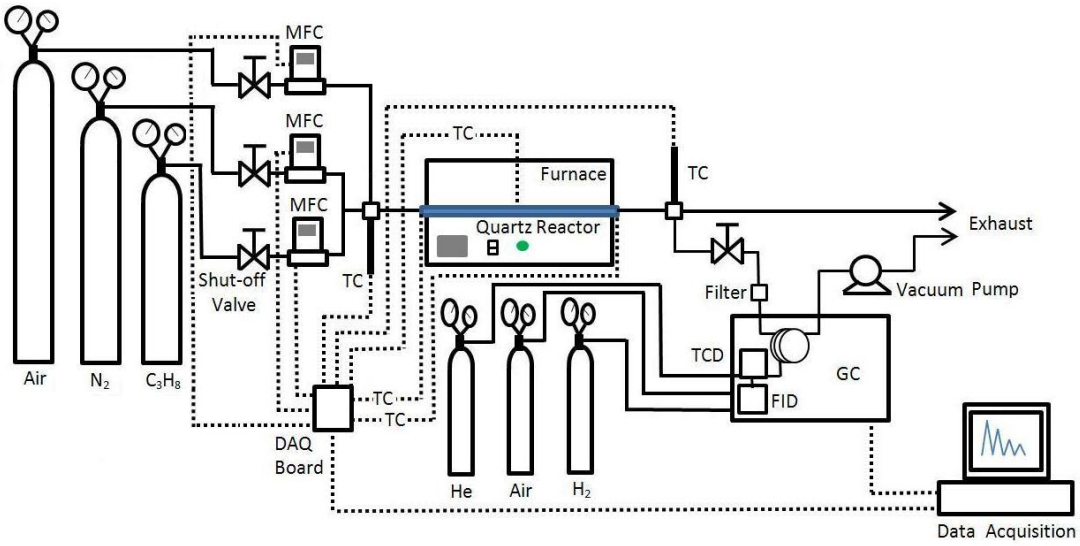

Figure 4.1: Schematic diagram for DR and POX reforming experimental setup.

propane/nitrogen mixtures for dry reforming case as well as propane/nitrogen/air mixtures for partial oxidation case. The gaseous fuel, nitrogen and air are mixed prior to the reactor in a connector which has four openings; one for propane/nitrogen and second for air whereas the third outlet is connected to thermocouple (TC as shown in Figure 4.1) and fourth one is for outlet mixture upstream to the reactor. The air supply is shut off when the only dry reforming of propane tests are required. The unit has three gas feed lines, each being independently controlled by digital mass-flow controllers. A tubular quartz flow reactor having 6.35 mm diameter is placed inside furnace. A quartz reactor is preferred than stainless steel reactor in order to visualize the coke formation or soot accumulation if any. The furnace temperature is controlled and monitored by an inbuilt temperature controller.

4.1.2 Reactor Set Up for Steam and Autothermal Fuel Reformings

A schematic for the experimental setup for homogeneous steam reforming (SR) and autothermal reforming (ATR) of propane reactor system is shown in Figure 4.2. This reactor system is similar to DR and POX reactor set-up except it has a career gas bubbler/vaporizer in order to provide vaporized carrier gas supply to SR and ATR reactions. This set-up (Figure 4.2) is also used as a dual-feed system that can deliver propane/nitrogen/steam mixtures for steam reforming case as well as propane/nitrogen/air/steam mixtures for autothermal reforming case. The air supply is shut off when the only steam reforming of

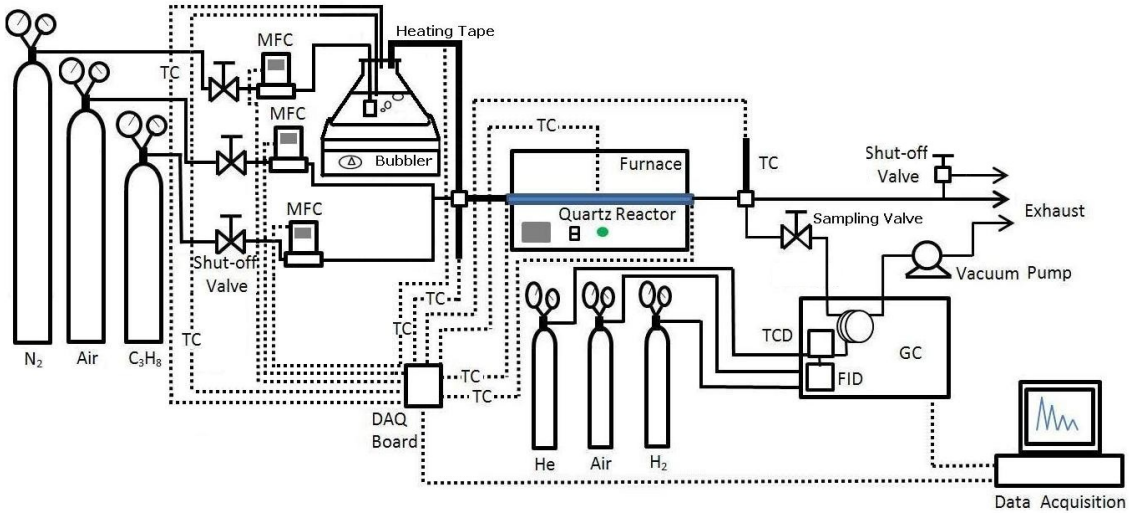

Figure 4.2: Schematic diagram for SR and ATR experimental setup.

propane tests are required.

The data acquisition system is set up to gather temperature measurements from the reactor, to control the flow rates of feed gases supply and also the reformed gas measurements from the exhaust. The temperature is measured with K-type thermocouples (OMEGA), which are inserted at different locations of the reactor system. The thermocouples at inlet and outlet positions within the furnace are at 5 inches apart from the middle thermocouple. One thermocouple is located at a position where a sample is taken for quantitative analysis of reformed gas from the exhaust. An another thermocouple is attached to the heating tape (refer Figure 4.2) to monitor its temperature whereas the last thermocouple is inserted inside of the flask (Figure 4.2) for the purpose to monitor water temperature. All these thermocouples and the digital mass flow controllers are connected with a multifunction data acquisition (DAQ) device (NI USB-6216, NATIONAL INSTRUMENTS). All the acquisition data is recorded and saved in a computer.

The bubbler system, as shown in Figure 4.2, consists of a liquid reservoir, often referred to as a flask which is held at constant elevated temperature. A detailed description is discussed in Appendix C, however a brief operation is summarized here. A carrier gas (N_2) is flowed (bubbled) through the liquid in the flask. The rate of carrier gas flow through the flask is set with a MFC. The bubbles of carrier gas absorb some of the molecules of the liquid and proceed through a heated delivery line into the main process chamber. The delivery line is heated to ensure that none of the vapor condenses prior to arriving in the process chamber. The amount of liquid vapor delivery to the process chamber strongly depends on

carrier gas flow rate, stability of liquid temperature, vapor pressure in the head space above the liquid and absorption rate of the liquid into the carrier gas. The absorption rate further depends on the formation of small bubbles of carrier gas in the liquid, in which the vapor quickly reaches its equilibrium vapor pressure as the bubble float to the liquid surface. In order to ensure formation of small bubbles and rapid equilibration, a sparger, a cap with multiple small perforations, is added at the end of the carrier gas inlet dip tube.

4.1.3 Analytical Technique

The composition of the effluent is quantitatively analyzed using a two channel gas chromatography system (SRI GC8610), which reports species concentrations in dry volume percentages. The details are discussed in Appendix B, but a brief operation is summarized here. The carrier gas carries the sample through a separation column where the compounds in the sample gas partition into the separation column, based on their solubilities at the given temperature. The thermal conductivity (TCD) detector measures the difference in thermal conductivity in carrier gas flow and the analyte peaks. Helium is used as a carrier gas for the TCD as it has a higher thermal conductivity compared to most organic compounds. As each compound of the separated sample gas passes through the detector, a quantitative response in the form of a peak is generated by the detector signal and a collection of these peaks make up a chromatogram. The fraction containing H_2, O_2, N_2, CO and CH_4 is detected by a Molecular Sieve column whereas the haysep D packed column inside gas chromatography (GC) system determines concentrations of CO_2 and hydrocarbon species such as ethylene, ethane, acetylene and propane hydrocarbon species. Although the quantitative analysis tests were done by using both detectors, the TCD and FID, only TCD analysis test results are used as a reference in order to compare each fuel reforming process in terms of species concentrations and reactor performances. The exhaust sample is extracted from the reactor with an external GC vacuum pump through an inert Silco steel tubing of 1/16" diameter. The detailed description of gas chromatography system, which includes standard gases calibration, detailed procedure to perform quantitative analysis using GC, retention time of peaks of interest, temperature program and events table, presented in Appendix B. To turn the raw area of a peak into a real world number, the peak needs to be calibrated. A table listing the retention time and standard gases calibration of each species is also mentioned in Appendix B.

4.1.4 Experimental Procedure

A pressure drop leak test is performed prior switching on the furnace in order to make sure all the flow lines are leak proof. Once the desired temperature inside furnace is stabilized, nitrogen gas at desired flow rate is supplied upstream to the reactor. A clean nitrogen sample is verified by analyzing its retention time and peak into the GC system to make sure there is no diffusion of air through possible connections of the setup. Then, fuel (propane) at required flow rate is mixed with nitrogen upstream to the reactor for DR tests. Air, however, is supplied at set flow rate before adding propane during POX reactions. On the other hand, for SR tests, nitrogen is first entered to the bubbler section and a mixture of nitrogen and vapors mixed with propane prior supplying feed upstream to the reactor. Same set-up of SR except additional air was used for ATR tests. All the experiments were conducted at atmospheric pressure and at temperatures ranging from 500 to 1000 °C. The operating parameters including reactants flow rates, their feed ratios, pressure and temperature range selection is tabulated in Table 3.1. Propane is supplied for a duration of five minutes prior taking any sample for GC measurements. The carbon deposits inside the reactor tube are occasionally removed by interrupting fuel supply and purging the reactor with air for five minutes, after which the experiment is continued. Experiments are carried out in an empty bed reactor in order to investigate homogeneous reforming of propane.

In order to assess the uncertainty of the GC measurements, the gas analysis is repeated for three consecutive samples to get a consistent gas composition. While the uncertainty is calculated for each species in the product stream for each analysis test as the root-sum-square of the contributing uncertainties, error bars are plotted for relative error of the mean for individual species composition.

4.2 Results and Discussion

This section focuses on results and discussion for experimental data obtained for homogeneous (non-catalytic) reforming via DR, POX, SR and ATR. The experimental data is quantitatively obtained from a gas chromatogram; the procedure of analyzing product samples downstream the reactor is described in detail in Appendix B. The data includes product species concentration for major species (H_2, CO, C_3H_8 etc.) and minor species (trace amounts of small hydrocarbon species). It includes performance evaluation in terms of efficiencies for DR, POX, SR and ATR processes. Out of many possible matrices useful for the assessment of the fuel reforming process, three efficiencies are sufficient to define the performance of

each reforming process. These efficiencies include propane conversion, hydrogen generation and carbon monoxide generation efficiencies. Propane conversion efficiency can be defined as

$$\eta_{C_3H_8,\,conversion} = \frac{\dot{N}_{C_3H_8,in} - \dot{N}_{C3H8,out}}{\dot{N}_{C_3H_8,in}} \times 100\% \tag{4.1}$$

Hydrogen production efficiency compares the amount of hydrogen in the exhaust to the hydrogen bound in the fuel and thus is a crucial parameter in evaluating reactor performance. It is defined as the ratio of molar rate (or moles or vol%) of H_2 generated to the maximum molar rate (or moles or vol%) of H_2 available in the reactant fuel.

$$\eta_{H_2,\,prod.} = \frac{\dot{N}_{H_2,\,prod.}}{4\dot{N}_{C_3H_8,in}} \times 100\% \tag{4.2}$$

In eqn. 4.2, 4 is the maximum number of H_2 atoms bound to propane.

Another important constituent of syngas is carbon monoxide, which can be used directly as a fuel as well as indirectly to increase hydrogen production in catalyzed water-gas shift reactions [12]. Similar to hydrogen production efficiency, CO production efficiency is calculated by dividing the molar rate (or moles or vol%) of CO in the products by the molar rate (or moles or vol%) of carbon in the reactant fuel.

$$\eta_{CO,\,prod.} = \frac{\dot{N}_{CO,\,prod.}}{3\dot{N}_{C_3H_8,in}} \times 100\% \tag{4.3}$$

The conversion of volumetric flow rates of species in the reactant mixture into their molar flow rates is discussed in Appendix A.

4.2.1 Exhaust Gas Composition

4.2.1.1. Homogeneous Dry Reforming

Figure 4.3 depicts the effect of temperature on species concentration present in the product stream for a case of DR of propane. The reactants flow rates of 19.8 mlpm, 475.2 mlpm and 495 mlpm for propane, nitrogen and mixture respectively are used, which are in accordance with reactants molar ratios specified in Table 3.1. Results in Figure 4.3 show that propane decreases with increase of temperature and it vanishes at 1000 °C. The reason for decreasing propane is the formation of hydrogen containing

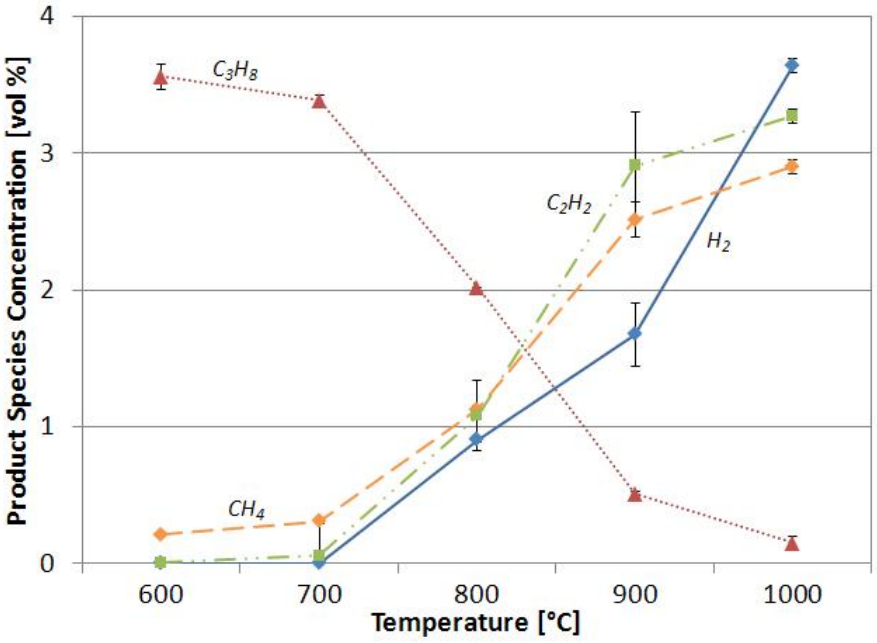

Figure 4.3: Effect of temperature on product species concentration for DR of propane (homogeneous reaction, $\chi_{C_3H_8} = 0.04$, $\chi_{N_2} = 0.96$ *and* $CPR = 24$; C_3H_8 = 19.8 mlpm, N_2 = 475.2 mlpm and mixture = 495mlpm) : experimental test result with error bars.

species as temperature increases. The concentration of these hydrogen species increases with reactor temperature. The hydrogen containing species appear in the temperature range tested include H_2, CH_4, C_2H_2(acetylene), C_2H_6 (ethane) and negligible amount of other hydrocarbons. It is noted that only hydrocarbon species appear in DR whereas no CO and CO_2 appear because no oxygen is introduced into the reactant stream. Many intermediates of the complex fuel break-down of propane combustion are found in the syngas, where CH_4 and C_2H_2 are more significant (Figure 4.3). The GC system does not allow for a conclusive analysis of C_3 species, for example insufficient separation between C_3H_6 and C_3H_8, although measurements indicate that concentrations are significantly lower than those of C_2 intermediates. The reason for insufficient separation between propene and propane is their appearance at the same time into chromatogram i.e. they have identical retention times. Among the remaining hydrocarbon species captured by the GC, C_2H_6 was most significant with typical levels of 0.05%. The formation of C_2H_6 in the exhaust is closely linked to C_2H_2, both of which are important precursors for polycyclic aromatic hydrocarbons (PAHs) and, subsequently, soot [49].

It is noted that all propane is converted to hydrogen and carbon in the thermodynamic equilibrium analysis (Figure 3.8a) because of propane cracking and carbon formation reactions [58]: $C_3H_8 \rightarrow 4H_2 +$

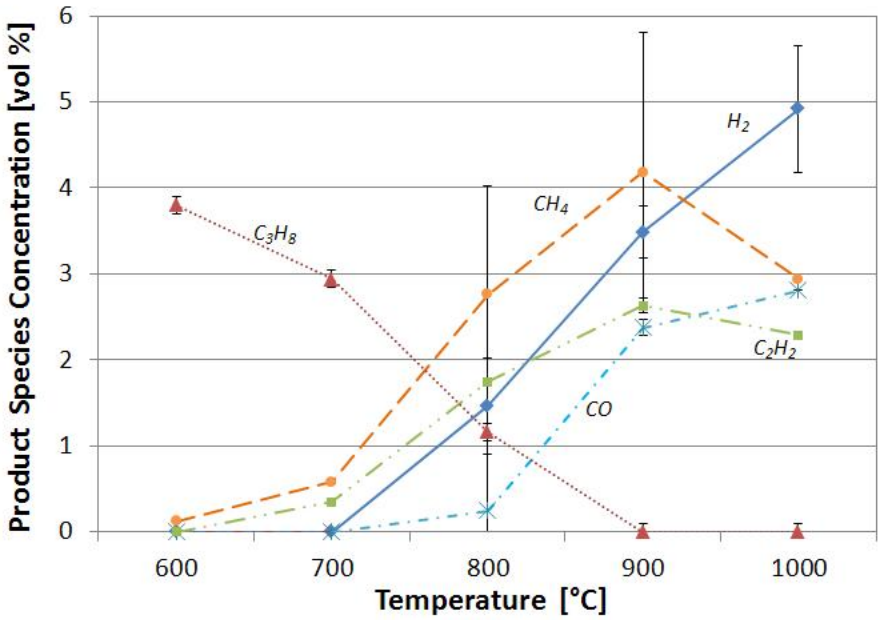

Figure 4.4: Effect of temperature on product species concentration (vol.%, dry basis) for POX of propane (homogeneous reaction, $\chi_{C_3H_8} = 0.04$, $\chi_{air} = 0.12$, $\chi_{N_2} = 0.84$, CPR = 21 and APR = 3; C_3H_8 = 19.8 mlpm, air = 59.4 mlpm, N_2 = 415.8 mlpm and mixture = 495mlpm) : experimental test result with error bars.

3C and $CH_4 \rightarrow 2H_2 + C$. However, in actual conditions, carbon is preferentially converted to small hydrocarbon species (mainly CH_4, C_2H_2 and negligible fractions of C_2H_6, isobutane, normal butane, isopentane, normal pentane, and normal hexane). It is noted that no hydrogen is observed (Figure 4.3) below 700 °C and a fraction of propane is converted to methane. Results show that propane requires temperature more than 700 °C to break down into lower hydrocarbon species if no catalysts are used. The theoretical amount of hydrogen (Figure 3.8a) always appears above experimental data. Maximum hydrogen obtained from DR reaction is below 4% whereas from thermodynamic analysis is above 12 % (vol%). The reason for this difference is due to the formation of acetylene and ethane in actual tests whereas negligible amount of them appeared in thermodynamic equilibrium calculations. The reason for decreasing trend of CH_4 in thermodynamic equilibrium analysis is attributed to the reaction $CH_4 \rightarrow 2H_2 + C$ whereas its increasing trend in experiments is due to propane cracking reaction $C_3H_8 \rightarrow C_2H_2 + CH_4 + H_2$.

4.2.1.2. Homogeneous Partial Oxidation

Figures 3.8b and 4.4 depict the effect of temperature on product species concentrations for par-

tial oxidation of propane. Figure 3.8b shows product species predicted by thermodynamic equilibrium whereas Figure 4.4 represents experimentally determined product species concentration (vol.%). The reactants flow rates of 19.8 mlpm, 59.4 mlpm, 415.8 mlpm and 495 mlpm for propane, air, nitrogen and mixture respectively are used according to reactants molar ratios specified in Table 3.1. It is observed in Figure 3.8b that propane decreases with temperature, since it breaks down to hydrocarbon species. Propane completely disappears at 900°C and beyond this temperature there is no further tendency for propane to break down to hydrocarbon species. This is the reason that major hydrocarbon species such as methane and acetylene decrease beyond 900°C. Maximum hydrogen obtained from POX experiments is 4.9% whereas from thermodynamic analysis is above 12 % . This difference is due to the formation of lower hydrocarbon species such as C_2H_2, CH_4 and fractions of C_2H_6 in actual reforming tests whereas negligible amount of them appears in thermodynamic equilibrium analysis. All propane is converted to hydrogen and carbon in thermodynamic analysis, however, in actual conditions, carbon is used to form other hydrocarbon species. It is noted in Figure 3.8b that H_2 linearly increases with entire temperature range for thermodynamic equilibrium predictions and it always appears above experimental observations. However, H_2 (Figure 4.4) increases from 700 °C to 1000 °C and no hydrogen is observed below 700°C. This is because a fraction of propane is only converted only to methane below 700°C. The maximum hydrogen achieved in POX (4.9%) is higher than maximum hydrogen achieved in DR (3.6%). It is noted that a carbon balance between reactants and products can be used to quantify carbon contained in product species not captured by the GC system. An analysis of the GC results reveals, however, that carbon contained in the measured product species balances the carbon in the reactant stream. While this does not contradict formation of soot and graphite in experiments, it indicates that carbon is preferentially converted to CO and small hydrocarbon species. It is noticed in Figure 4.4 that CH_4 first increases from 600 to 900°C and then decreases beyond 900°C for the reason of complete conversion of propane into lower hydrogen containing species at 900°C. Also, CO continuously increases from 700 to 1000°C whereas negligible fractions of CO_2 (not shown) appeared in decreasing fashion. The reason for these trends is attributed to methanation reaction ($CH_4 + H_2O \leftrightarrow CO + 3H_2$) and reverse water gas shift reaction ($CO + H_2O \leftrightarrow CO_2 + H_2$) at high temperatures. The reverse water gas shift reaction is also a reason for formation of small amount of water in experiments. This might be an another reason for lower

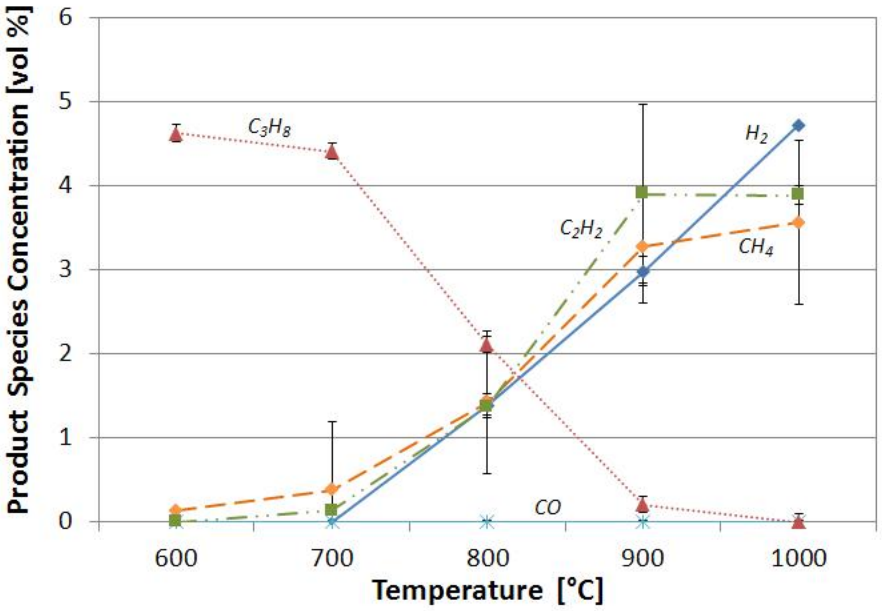

Figure 4.5: Effect of temperature on product species concentration (vol.%, dry basis) for SR of propane (homogeneous reaction, $\chi_{C_3H_8} = 0.04$, $\chi_{H_2O} = 0.12$, $\chi_{N_2} = 0.84$, CPR = 21 and WPR = 3; C_3H_8 = 19.8 mlpm, water vapors = 59.4 mlpm, N_2 = 415.8 mlpm and mixture = 495mlpm) : experimental tests result.

hydrogen production in experiment than in thermodynamic equilibrium analysis. The results presented for product species concentration are based on dry basis because of limitations of the GC system to directly measure the H_2O content in the product stream. Similar to homogeneous dry reforming results, the partial oxidation results indicate that propane requires temperature more than 700 °C to break down into lower hydrocarbon species if no catalysts are used.

4.2.1.3. Homogeneous Steam Reforming

Figure 4.5 shows experimentally determined product species concentration (vol.%). The reactants flow rates of 19.8 mlpm, 59.4 mlpm, 415.8 mlpm and 495 mlpm for propane, vapors, nitrogen and mixture respectively are used according to reactants molar ratios specified in Table 3.1. It is observed in Figure 3.8c that propane decreases with increase of temperature and it vanishes at 1000 °C. The decrease in propane below 700°C and above 900°C is gradual, however, a steep decrease in propane is observed in the temperature range of 700 ~ 900°C. The reason for decreasing propane is the formation of hydrogen containing species as temperature increases. Although the concentration of these hydrogen species increases with reactor temperature, their gradual increase below 700°C and above 900°C is due to behavior of propane as discussed above. The hydrogen containing species appear in the temperature

range tested include H_2, CH_4, C_2H_2(acetylene), C_2H_6 (ethane) and negligible amount of other hydrocarbons. It is observed in Figure 3.8c that H_2 linearly increases (between the range of 11% to 19%) with all temperature range for the thermodynamic equilibrium predictions. However, H_2 starts increasing from 700°C to 1000°C for the reason propane requires temperature higher than 600°C to produce hydrogen. However, small fraction of hydrogen (around 0 to 0.05%) is observed below 700°C and a fraction of propane is converted to methane. This is due to the tendency of propane to breaks down only to small hydrocarbon species below 700°C. Theoretical amount of hydrogen (Figure 3.8c) always appears above the experimental data points for H_2. Maximum hydrogen obtained from SR experiments is limited to 4.9% whereas it is 19% in the thermodynamic equilibrium. This difference is due to the formation of lower hydrocarbon species such as C_2H_2, CH_4 and fractions of C_2H_6 in actual reforming tests whereas negligible amount of them appears in the thermodynamic equilibrium. It is noted that no CO and CO_2 appear in experimental test results. This is attributed to strong dependency of SR on propane cracking reaction $C_3H_8 \rightarrow C_2H_2 + CH_4 + H_2$. This claim could be substantiated by simultaneous increase of H_2, C_2H_2 and CH_4 in the experimental test results.

4.2.1.4. Homogeneous Autothermal Reforming

The reactants flow rates of 17.68 mlpm, 53.04 mlpm, 53.04 mlpm, 371.25 mlpm and 495 mlpm for propane, vapors, air, nitrogen and mixture respectively are used according to reactants molar ratios specified in Table 3.1. The product species appeared in ATR of propane are shown in Figures 3.8d and 4.6. Figure 3.8d shows product stream species appeared in the thermodynamic equilibrium analysis whereas Figure 4.6 shows experimentally determined product species at different temperatures. Results in Figure 4.6 that propane as appeared in the homogeneous DR, POX and SR decreases with temperature and it completely disappears at 900 °C. It is noted in Figures 3.8d and 4.6 that the trend of H_2in product stream is same i.e. it increases with temperature. However, theoretical H_2 concentration in product stream varies between 15.5% to 20.5%) whereas experimental H_2 concentration appears very low i.e. it increases in the range 0 to 5.5% between 700 to 1000°C. The reason for this difference between theoretical and experimental amount of H_2 is attributed to the formation of small hydrocarbon species such as CH_4 and C_2H_2 along with H_2 at high temperature for actual tests. No hydrogen is observed below 700 °C and a fraction of propane is converted only to methane. This is due to propane requirement

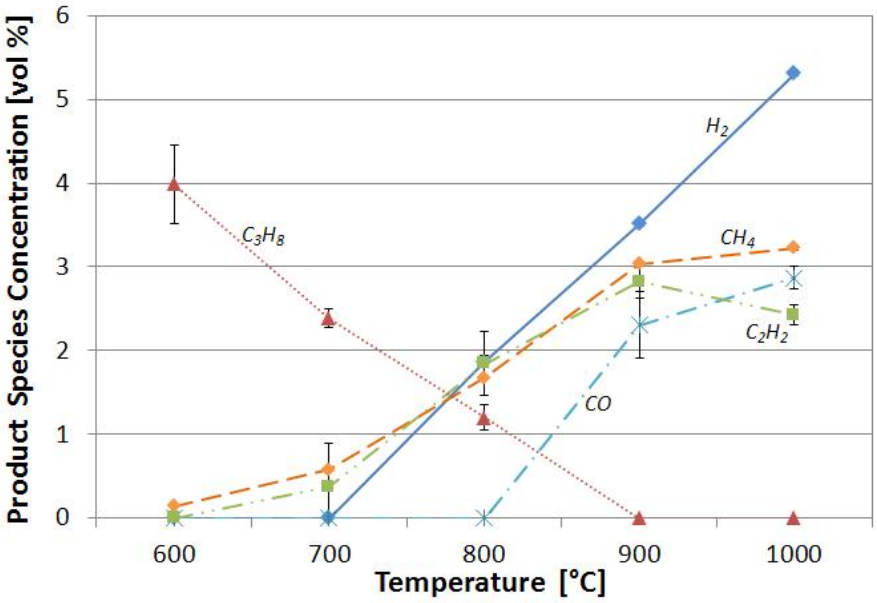

Figure 4.6: Effect of temperature on product species concentration (vol.%, dry basis) for ATR of propane (homogeneous reaction, $\chi_{C_3H_8} = 0.0358$, $\chi_{air} = 0.1071$, $\chi_{H_2O} = 0.1071$, $\chi_{N_2} = 0.75$, CPR = 21, WPR = 3 and APR = 3; C_3H_8 = 17.68 mlpm, air = 53.04 mlpm, water vapors = 53.04 mlpm, N_2 = 371.25 mlpm and mixture = 495mlpm) : experimental tests result.

to breaks down into lower hydrocarbon species above 700 °C temperature. It is noticed in Figure 4.6 that CH_4 concentration continuously increases from 0 to 3% between temperature 600 to 900°C and then its concentration becomes almost stable from 900 to 1000°C. The increase of methane upto 900°C is due to propane cracking reaction $C_3H_8 \rightarrow C_2H_2 + CH_4 + H_2$. Negligible change in methane and increase of CO above 900°C is attributed to methanation reaction ($CH_4 + H_2O \leftrightarrow CO + 3H_2$). It is also noted that CO increases from 0 to 2.8% between temperature range from 800 to 1000°C. The maximum hydrogen achieved in ATR is 5.8% which is higher than SR, POX and DR.

4.2.2 Evaluation of Homogeneous Reforming Processes

4.2.2.1. Propane Conversion Efficiency

Thermodynamic equilibrium predicts complete conversion of propane (Figure 4.7) for all homogeneous reforming processes Viz. DR, POX, SR and ATR at all temperatures. However, propane conversion efficiency increases with temperature for experimental analysis for all homogeneous reforming processes. The 100% propane conversion efficiency in thermodynamic analysis for all reforming processes at entire temperature range is due to the tendency of propane to completely breaks down into

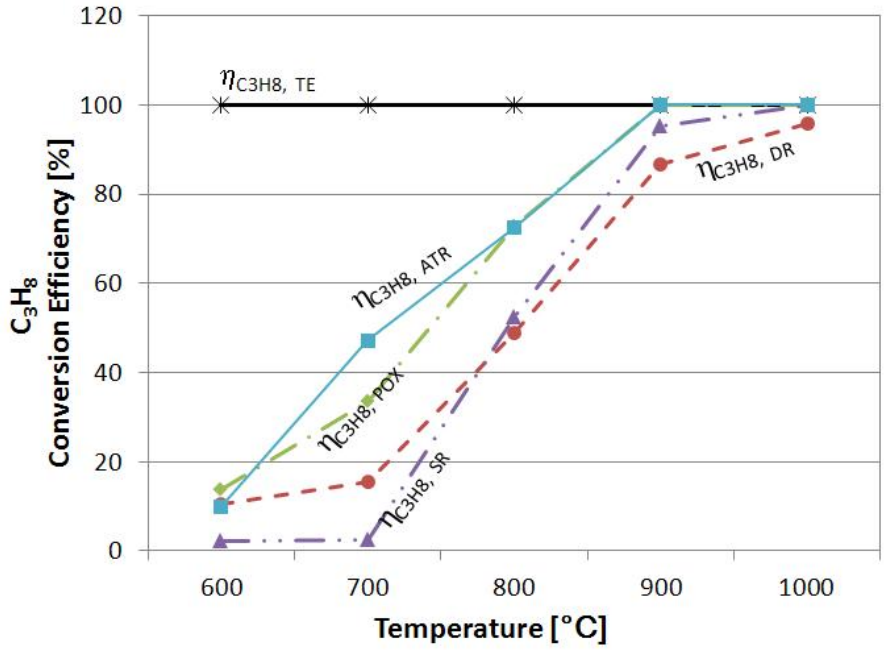

Figure 4.7: Propane conversion efficiency comparisons of DR, POX, SR and ATR homogeneous processes (experiments) with thermodynamic equilibrium (TE) predictions.

hydrogen, carbon and methane along negligible amount of acetylene and ethane even at at temperature 500°C . Propane conversion efficiency for homogeneous DR process (experiment) increase from 10.6% to 96% with temperature. The maximum propane conversion efficiency achieved in homogeneous DR process is 96% at 1000 °C. This indicates that hydrogen containing species such as C_2H_2, CH_4 and H_2 increase simultaneously with temperature, since propane tendency to breaks down into hydrogen containing species increases with temperature increase. Propane conversion efficiency for homogeneous POX process (experiment) increases linearly (from 14% to 100%) with temperature. It is observed that maximum propane conversion efficiency for POX is 100% achieved at 900°C. This indicates that propane requires 900°C to completely convert into hydrogen and other lower hydrocarbon species. Also it is noted that propane conversion efficiency for homogeneous SR process (experiment) continuously increases from 2 to 100% with temperature increase from 600 to 1000°C. The experimental propane conversionefficiency for homogeneous ATR process always appears higher than that of DR, POX and SR, and it continuously increases from 10 to 100% with temperature increase from 600 to 900°C. It becomes stable above 900°C. The overall propane conversion efficiency trend for homogeneous propane reforming processes is ATR>POX>SR>DR. The high propane conversion efficiency for ATR process is

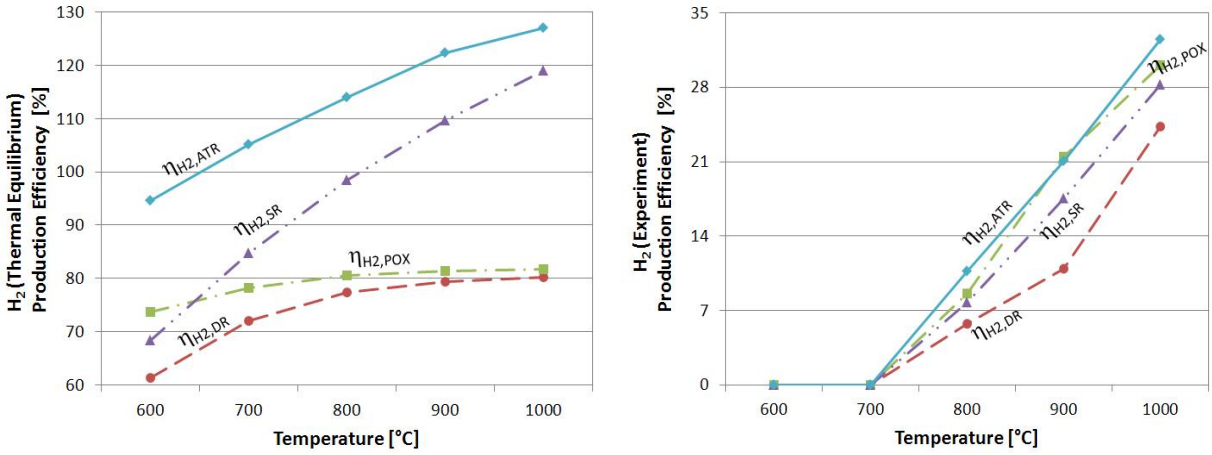

(a) η_{H_2} (Thermodynamic equilibrium)

(b) η_{H_2} (Experiments)

Figure 4.8: Hydrogen production efficiency comparisons of experimental homogeneous propane reforming routes with thermodynamic equilibrium analysis predictions

due to the addition of both steam and air into the reactant stream.

4.2.2.2. Hydrogen Production Efficiency

Hydrogen production efficiency compares the amount of hydrogen in the exhaust to the hydrogen bound in the fuel and thus is a crucial parameter in evaluating reactor performance. The hydrogen production efficiencies for homogeneous thermodynamic equilibrium analysis and experimental analysis for DR, POX, SR and ATR are shown in Figures 4.8a and 4.8b respectively. It is noted that hydrogen production efficiency increases with respect to temperature for both thermodynamic equilibrium predictions as well as experimental test runs for all reforming processes at temperature range from 600 to 1000°C. This trend of increasing hydrogen is attributed to break down of propane into hydrogen and lower hydrocarbon species with the increase of temperature. It is noted that the hydrogen production efficiency always appears higher in the thermodynamic equilibrium predictions as compared to experiments for homogeneous DR, POX, SR and ATR. This difference is due to to the formation of acetylene and ethane in actual tests whereas negligible amount of them appeared in thermodynamic calculations. It is also seen that hydrogen production efficiency for homogeneous ATR always appears higher than all other propane reforming processes for both thermodynamic analysis and actual tests. Also, the lowest hydrogen production efficiency appears in propane dry reforming and hydrogen production efficiencies for POX and SR stay between efficiencies of ATR and DR processes. In other words, the most efficient homogeneous

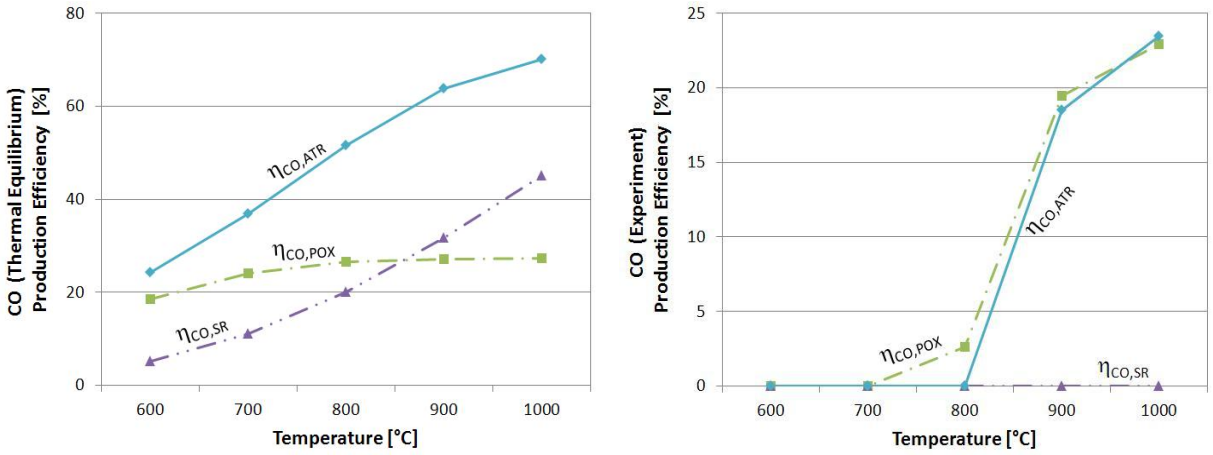

(a) η_{CO} (Thermodynamic equilibrium)

(b) η_{CO} (Experiments)

Figure 4.9: CO production efficiency comparisons of experimental homogeneous propane reforming routes with thermodynamic equilibrium analysis predictions

propane reforming process has the order of ATR > POX > SR > DR for actual tests whereas for thermodynamic predictions the order is ATR > SR > POX > DR. This difference is attributed to the absence of CO in actual homogeneous steam reforming process whereas a significant amount of CO appears in the thermodynamic equilibrium analysis for steam reforming. This leads to different behavior of water-gas shift reaction in thermodynamic calculations and actual tests. The maximum hydrogen production efficiency achieved at 1000°C in actual homogeneous reforming in DR is 24% whereas 28% for SR, 30% for POX and 32.5% for ATR. The reason for lower hydrogen production efficiency is due to formation of other hydrocarbon species in large amounts such as methane, acetylene and small amounts of ethane and other hydrocarbon species.

4.2.2.3. CO Production Efficiency

Figure 4.9 shows CO production efficiency as a function of temperature for homogeneous propane reforming processes The comparisons among actual homogeneous POX, SR and ATR with the thermodynamic equilibrium prediction are shown in Figure 4.9. The CO production efficiency for homogeneous DR process is zero at all temperatures, because of absence of oxygen in reactant stream. It is noted in Figure 4.9a that the CO production efficiency linearly increases for both the SR and ATR whereas it increases for POX upto 800°C and it does not change much afterward. However, it is seen in Figure 4.9b that the CO production efficiency behavior is very similar in homogeneous POX and ATR processes

i.e. it increases linearly with temperature. The CO production efficiency always appear lower in homogeneous POX and ATR process than in the thermodynamic equilibrium predictions. This is due to the formation of large amount of small hydrocarbon species such as CH_4, C_2H_2 and small fraction of C_2H_6 in the product stream for actual POX and ATR processes and therefore, there is less tendency for the reaction of oxygen with carbon in propane to produce CO and CO_2. It is also noted that no CO appears in actual homogeneous steam reforming tests. The reason for this experimental behavior of homogeneous SR of propane for CO is the occurrence of propane cracking reaction $C_3H_8 \rightarrow C_2H_2 + CH_4 + H_2$ instead of methanation reaction (CH_4 + $H_2O \leftrightarrow$ CO + $3H_2$) and water gas shift reaction (CO + $H_2O \leftrightarrow$ CO_2 + H_2).

4.3 Summary

Experiments were conducted for homogeneous reforming of propane via. dry, partial oxidation, steam and autothermal reforming thermochemical energy conversion processes. The optimum operating parameters (refer Table 3.1) including pressure, temperatures, career to propane (CPR), air to propane (APR) and water to propane (WPR) in experiments were guided by the thermodynamic equilibrium evaluation of homogeneous binary (i.e. DR) and ternary (i.e. POX, SR and ATR) reforming processes. The thermodynamic equilibrium calculations use an idealized thermodynamic state with maximum entropy to predict the composition of the reacted mixture. This state requires infinite residence time for all chemical reactions to complete, which in actual practice it is not feasible. Therefore, it restricts equilibrium calculations to qualitative predictions. The thermodynamic equilibrium solver is used as a reference tool to qualitatively choose operating conditions such as pressure, temperature and reactants feed ratio irrespective of reaction kinetics, reactor design and operation.

It was observed that the 100% propane conversion efficiency was appeared in the thermodynamic equilibrium analysis for all reforming processes at entire temperatures range. The propane conversion efficiency for homogeneous DR process (experiment) increase from 10.6% to 96% with temperature. The maximum propane conversion efficiency achieved in homogeneous DR process is 96% at 1000 °C. The propane conversion efficiency for homogeneous POX process (experiment) increases linearly (from 14% to 100%) with temperature. It is observed that the maximum propane conversion efficiency for POX is 100% achieved at 900°C. Also it is noted that propane conversion efficiency for homogeneous

SR process (experiment) continuously increases from 2 to 100% with temperature increase from 600 to 1000°C. The experimental propane conversionefficiency for homogeneous ATR process always appears higher than that of DR, POX and SR, and it continuously increases from 10 to 100% with temperature increase from 600 to 900°C. It becomes stable above 900°C. The overall propane conversion efficiency trend for homogeneous propane reforming processes is ATR > POX > SR > DR.

It was noted that the hydrogen production efficiency always appeared higher in the thermodynamic equilibrium predictions as compared to the experiments for homogeneous DR, POX, SR and ATR. This difference is due to the formation of acetylene and ethane in actual tests whereas negligible amount of them appeared in thermodynamic calculations. It was also seen that hydrogen production efficiency for homogeneous ATR always appears higher than all other propane reforming processes for both thermodynamic analysis and actual tests. Also, the lowest hydrogen production efficiency appears in propane dry reforming and hydrogen production efficiencies for POX and SR stay between efficiencies of ATR and DR processes. In other words, the most efficient homogeneous propane reforming process has the order of ATR > POX > SR > DR for actual tests whereas for the thermodynamic equilibrium predictions the order is ATR > SR > POX > DR. This difference is due to the absence of CO in actual homogeneous steam reforming process whereas a significant amount of CO appears in the thermodynamic analysis for steam reforming. This leads to different behavior of water-gas shift reaction in thermodynamic calculations and actual tests. The maximum hydrogen production efficiency achieved at 1000°C in actual homogeneous reforming in DR is 24% whereas 28% for SR, 30% for POX and 32.5% for ATR. The reason for lower hydrogen production efficiency is due to formation of other hydrocarbon species in large amounts such as methane, acetylene and fraction of ethane.

CO production efficiency for homogeneous DR process is zero at all temperatures, because of absence of oxygen in reactant stream. CO production efficiency linearly increases for SR and ATR whereas it increases for POX upto 800°C and it does not change much afterward. However, it is seen in Figure 4.9b that the CO production efficiency behavior is very similar in homogeneous POX and ATR processes i.e. linearly increases with temperature. The CO production efficiency always appear lower in homogeneous POX and ATR process than in thermodynamic predictions. This is due to the formation of large amount of small hydrocarbon species such as CH_4, C_2H_2 and small fraction of C_2H_6 in the product

stream for actual POX and ATR processes. It is also noted that no CO appears in actual homogeneous steam reforming tests.

From the thermodynamic equilibrium analysis and experimental investigations, it is concluded that the autothermal reforming (ATR) process is most suitable whereas DR is least suitable for not only producing hydrogen rich syngas but also in terms of clean and carbon free process. The thermodynamic equilibrium analysis, however, provides similar trends in the assessment of homogeneous propane reforming processes in terms of major syngas species, propane conversion, hydrogen production and carbon monoxide production efficiencies. The difference between the theoretical qualitative predictions and the experiment quantitative results is attributed to inclusion of solid carbon in product stream in the thermodynamic equilibrium analysis whereas the carbon in actual tests is converted to ethane and acetylene.

Chapter 5
Preliminary Studies for Heterogeneous Fuel Reforming

This Chapter discusses preliminary studies for heterogeneous autothermal reforming for future scope of catalytic thermochemical energy conversion routes. The suitable non-noble metal base catalyst selection, its preparation and preliminary test results for heterogeneous ATR processes are proposed to improve the performance of reactor performance at low temperatures, however, the detail study of heterogeneous fuel reforming is beyond the scope of this thesis.

5.1 Literature Review

5.1.1 Catalyst Selection

Various catalysts, mostly noble metal-based catalysts (Pt, Rh and Pd) have already been studied in detail in the past decade for the reforming of hydrocarbon fuel, especially for methane and propane [38, 27, 14]. However, very limited resources are available for non-noble metal based catalysts favoring heterogeneous fuel reforming processes. Holmen et al. [51] suggested in his extensive study on catalytic POX and ATR of propane that rhodium (Rh) has been found to be superior to platinum with respect to optimizing H_2 and minimizing H_2O formation. In addition, Rh catalyst showed no loss in activity at 1000 ºC for several hours. Although nickel (Ni) catalysts offered similar conversion and selectivity, but showed a stronger tendency to deactivation. Laosiripojana et al. (2006) [32] suggested the order of catalysts reactivity for dry reforming as well as steam reforming of propane is Ru > Rh > Ni > Pt > Pd.

Olsbye et al. [26] reported an highly stable Ni/Mg(Al)O hydrotalcite-derived catalyst and he suggested that the intrinsic activity of catalysts strongly depends on Ni particle size. It has been discussed in literature [33, 32, 6, 62] that higher dispersion of Ni and its smaller particle size can minimize Ni sintering at high temperatures and impede coke accumulation at Ni lattice sites, and thus, accelerating catalyst stability in hydrocarbon reforming processes. Hardiman et al. [25] investigated a bimetallic Co-Ni/Al_2O_3 catalyst in both DR and SR of propane and catalyst was deactivated due to carbon deposition.

Moreover, previously developed Ni metal-based catalysts for natural gas reforming process, suffer from deactivation issues because of sintering of metallic Ni and also of the coke formation. Ozkan et al.

[62] suggested the formation of two side reactions, Boudouard reaction ($2CO = C + CO_2$) and methane decomposition, are the possible reason for coke formation at the surface of Ni during hydrocarbon steam reforming. To avoid the issues of carbon deposition and sintering of non-noble metal based catalysts, extensive research has been done in the development of supported precious metal catalysts (Pd, Pt and Rh) for hydrocarbon reforming reactions, since they showed excellent activity and stability as compared to Ni metal based catalysts. However, low cost, easy availability and long performance of Ni-based catalysts, still it can be efficiently used in hydrocarbon fuel reforming by improving its resistance to coke formation.

A few researchers have worked in the direction of improving Ni-based catalysts in hydrocarbon fuel reforming applications [54, 26, 19]. For instance, Alkali metal oxides (CaO and K_2O) have shown to improve coke resistance. The addition of tungsten or molybdenum in small proportions (~ 0.5 wt%) in Ni catalysts has been proven to inhibit coke formation without loosing catalyst activity.

Furthermore, lanthanide addition in Ni-based catalysts (collectively known as rare earth elements; a series comprising fifteen metallic chemical elements with atomic numbers 57 through 71, from lanthanum through lutetium) suppress coke formation by inhibiting diffusion of carbon into Ni particles without sacrificing its activity [62]. Wang and Lu [56] have shown in his work on catalytic dry reforming of methane that the addition of CeO_2 into Ni/Al_2O_3 catalysts enhanced nickel dispersion and reactivity, and hence improved catalyst activity and stability.

Due to the low cost and ready availability of nickel (Ni) metal, the supported Ni metal-based catalysts are the preferred choice for the present investigation of catalytic reforming reactions for propane. The purpose of the catalytic thermochemical conversion in present study is to determine the overall behavior of reforming reactions of propane, especially SR and ATR using supported non-noble metal based catalysts such as Nickel (Ni).

5.1.2 Catalyst Support Selection

A catalyst support is the material, usually a solid with a high surface area, to which a catalyst is affixed. The reactivity of catalysts occurs at the surface atoms. Consequently great effort is made to maximize the surface area of a catalyst by distributing it over the support. The support may be inert or participate in the catalytic reactions. Typical supports include various kinds of carbon, alumina, and

silica. It was observed that selectivity of syngas (collectively for H_2 and CO) decreases in the order Al_2O_3 > MgO > CaO, where Al_2O_3, MgO and CaO are used as catalyst supports. The propane conversion and hydrogen selectivity is much lower in the presence of NiO/MgO and NiO/SiO_2 catalysts than with NiO/Al_2O_3 catalyst. Table 5.1 shows a compilation of various alumina supported catalysts investigated previously for POX, SR and ATR. It also includes various process parameters e.g. temperature, S/C ratio and O_2/C_3H_8 ratio, and their process evaluation in terms of propane conversion and hydrogen percentage.

5.1.3 Additive Promoter Selection

According to the study done by Wang and Lu [56], the addition of CeO_2 into Ni/Al_2O_3 catalysts enhanced the nickel dispersion and reactivity of carbon deposits, leading to an improvement in the catalytic activity and stability in CO_2 reforming of methane. Cerium oxide has been suggested to promote catalysis of oxidation reactions due to its the high capability of oxygen storage. A high oxygen mobility (redox property), high oxygen storage capacity, strong interaction with the supported metal (strong metal–support interaction) and a modifiable capability makes this material very promising for catalytic thermochemical conversion of hydrocarbons. Ceria-based catalysts in steam reforming reactions have been reported by several researchers [33, 32, 2, 16] to be promising supports among α-Al_2O_3, γ-Al_2O_3 and rare earth metal oxide. It contains a high concentration of highly mobile oxygen vacancies, which act as local sources or sinks for oxygen involved in reactions taking place on its surface. Cerium oxide shows an easy transition between Ce^{4+} and Ce^{3+} and so can store large amounts of O_2 [6]. Recently, the successful test of ceria for the methane steam reforming reaction has been reported [33]. As the promoter, ceria was also reported to be a good promoter for the dry methane reforming at intermediate temperature. However, ceria causes several additional problems. On one hand, it stabilizes the catalyst, but on the other, it also creates side reactions, which causes changes at the surface sites [23]. One possible reason is that sub-oxide generated via the reduction of reducible oxides could migrate onto the surface of the metal particles and decrease the number of active Ni sites.

It can be concluded from the above discussion that Ni/Al_2O_3 catalysts performance in terms of its reactivity, stability and coke resistance can be improved either by making strong metal-support interaction, addition of CeO_2 into Ni/support catalyst, or by using smaller Ni particle size and its higher dispersion.

Therefore, nickelous aluminum oxide (Ni/Al_2O_3) is selected as a based catalyst rather than precious

Table 5.1: Various catalysts investigated for heterogeneous POX, SR and ATR and system parameters.

Reference	**Catalyst**	**Metal Loading [wt%]**	**Temp. [°C]**	**O_2/C_3H_8**	**S/C**	**$x_{C_3H_8}$ [%]**	**H_2**
Huff et al. (2001)	Pt/Al_2O_3foam monolith	4.3	800 ~ 1200	2.1	0	100	0 ~ 55 [Selectivity %)]
Guimaraea et al. (2003)	$Pd/Ce/Al_2O_3$	1	600	2.5	0	90	0.9 [mol %]
Guimaraea et al. (2003)	Pd/Al_2O_3	1	600	2.5	0	70	1.25 [mol %]
Gjervan et al. (2003)	Rh/Fecralloy reactor	-	1000	1.9	0	100	18 [vol %]
Ayabe et al. (2003)	Ni/Al_2O_3	2, 10	300 ~ 800	0.5	0, 0.5, 1.0, 1.5	20 ~ 100	~ 15, 30, 39, 49 [vol %]
Bansode (2006)	Pt/Al_2O_3, Pt/CeO_2	1	300 ~ 800	1.78	0	0 ~ 86.7	0 ~ 5.2 [Selectivity %)]
Olsbye et al. (2007)	Ni/SiO_2, Ni/Al_2O_3	2	600	5 (N_2:C_3H_8)	0	11 ~ 27	-
Laosiripojana et al. (2006)	Ceria doped Ni/Al_2O_3	10	700 ~ 900	0	2.86	0 ~ 80	18 ~ 80 [Yield %]
Ozkan et al. (2009)	Ni/Al_2O_3	20	500	0	1.33	upto 60	21 ~ 50 [vol %]
Holmen et al. (2004)	Rh/Al_2O_3	0.01	400 ~ 1000	1.88	1.0	80 ~ 100	55 ~ 65 [Selectivity %)]
Adesina et al. (2008)	Ce promoted Co-Ni/Al_2O_3	5 Co - 10 Ni	505 ~ 680	5 (CO_2: C_3H_8)	0	-	4.9 × 105 [mol/s]
Muhammad et al. (-)	Ni/Al_2O_3	75	300 ~ 500	0	2, 3.3, 5.2	-	~ 55, 65, 70 [mol%]

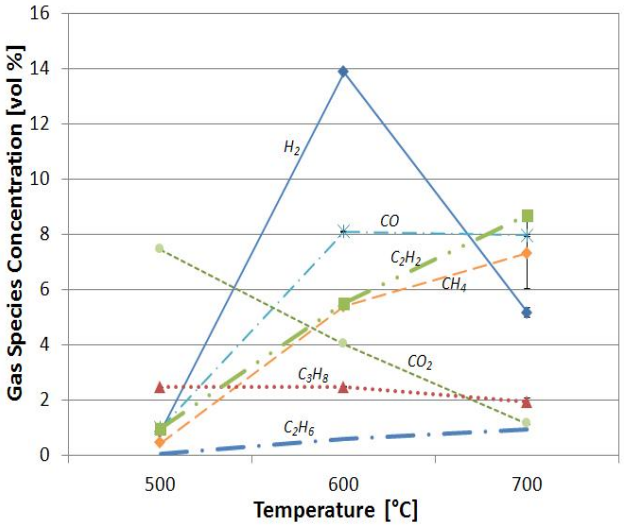

Figure 5.1: Effect of temperature on product species concentration (vol.% dry basis) for catalytic (15 wt.% Cerium- Ni/Al_2O_3) ATR of propane ($\chi_{C_3H_8} = 0.0358$, $\chi_{air} = 0.1071$, $\chi_{H_2O} = 0.1071$, $\chi_{N_2} = 0.75$, CPR = 21, WPR = 3 and APR = 3; C_3H_8 = 17.68 mlpm, air = 53.04 mlpm, water vapors = 53.04 mlpm, N_2 = 371.25 mlpm and mixture = 495mlpm) : experimental tests result.

metals whereas cerium oxide (CeO_2) is selected as an additive promoter in the present thesis. In this work, 15 wt% cerium oxide doped in 10 wt% Ni/Al_2O_3 catalyst is used mainly in steam reforming and oxidative steam reforming of propane and comparison has been made with the results obtained with 10 wt% Ni/Al_2O_3 catalyst.

5.2 Preliminary Test Results for Heterogeneous ATR

The variation of product species in exhaust gas as a function of temperature for the case of heterogeneous autothermal reforming process is depicted in Figure 5.1. The reactants feed ratios identical to homogeneous autothermal reforming process are used. A 15 wt% CeO_2 doped 10 wt% Ni/Al_2O_3 catalyst is used inside the reactor. The catalyst preparation method is discussed in Appendix D. The reactants mixture flow conditions identical to homogeneous ATR are used. These flow conditions include reactants feed ratio, gas hourly space velocity (GHSV = $\frac{1}{\tau_r} \times 3600$) and inlet total flow rate ($\dot{V} = V_R \times \tau_r$) of 2763.63 $h^{-1}$and $8.25 \times 10^{-6}\,m^3$ (equals 495 mlpm) respectively. The temperature of reactor varies from 500 to 700°C and pressure is maintained at 1 atm.

It is noted in Figure 5.1 that some of the results are as expected, but a substantially different behavior of heterogeneous ATR than homogeneous cases is observed. The results indicate that C_3H_8 barely changed with respect to temperature, while H_2 first increases from 500 to 600°C, then it suddenly de-

creases upto 700°C. Whereas overall behavior of concentration of CO increases with temperature and CO_2 concentration decreases with temperature. C_2H_2 increase from 500 to 700°C. The sudden fall in the concentration of $H_2$is attributed to deactivation of catalyst. It is also noted that due to deactivation of catalyst above 600°C, CH_4 suddenly increases. Although deactivation of catalyst appears above 600°C, the maximum concentrations of H_2(13.8 vol.% at 600°C) and CO (8 vol.% at 600°C) are substantially higher than maximum concentration of H_2(5.3 vol.%) and CO (2.9 vol.%) achieved at 1000°C in homogeneous autothermal reforming process. The reason for substantial difference between heterogeneous and homogeneous ATRs is attributed to the fact that the mass between inlet and outlet streams into the reactor is no longer easily balanced. This unbalanced mass conservation among species is caused by unexpected high concentration of C_3 species (for e.g. n-heptane).

5.3 Summary

The preliminary results for heterogeneous ATR indicate that the selected non-noble catalyst has promising results in terms of syngas production as compared to the homogeneous fuel reforming under identical operating conditions even at lower temperatures. However, due to unexpected behavior of heterogeneous process, more samples of catalyst with different CeO_2 and Ni loadings on Al_2O_3 metal support are needed to analyze heterogeneous DR, POX, SR and ATR in detail. In addition, detail gas-solid chemical kinetics study and reaction mechanism are needed to better understand the phenomenon behind higher concentration of hydrogen containing species in heterogeneous reforming processes. While commercial nickel-based catalysts are very effective in the elimination of biomass tar and its conversion to H_2 and CO, the quick deactivation of the nickel-based catalyst by carbon deposition and sintering of active Ni particles impedes its application. The proposed CeO_2 promoted Ni/Al_2O_3 catalyst has a potential for reforming/gasification of biomass because of redox properties of CeO_2. A high oxygen mobility (redox property), high oxygen storage capacity, strong interaction with the supported metal (strong metal–support interaction) and a modifiable capability makes this catalyst very promising for catalytic thermochemical conversion of hydrocarbons and biomass wastes. Due to strong interaction of cerium oxide with the supported metal, a common problem of catalyst attrition caused by particle collisions could be avoided during its application in spouted bed reactors.

Chapter 6
Conclusions

This thesis works in the direction of development of a laboratory scale conical spouted bed (CSB) reactor system for producing hydrogen rich syngas from hydrocarbon fuels such as propane and long-term fuel i.e. biomass wastes such as glycerol. The work towards this goal divides into three phases: the cold flow model facility in the first phase deals with the study of hydrodynamic behavior of a CSB reactor and the second phase involves a simpler plug flow reactor facility which is used for an evaluation of favorable operating conditions for hydrogen rich syngas production. The plug flow reactor is meant to provide preliminary results that are used to evaluate different reforming approaches, which will eventually be applied in a CSB reactor. The different reforming approaches include dry reforming (DR), partial oxidation (POX), steam reforming (SR) and autothermal reforming (ATR). Tests from the plug flow reactor hot flow studies are used to assess the efficiency of each homogeneous reforming process. The selection of operating conditions is guided by results from thermodynamic equilibrium analysis. Results from this study will lay the foundation for follow-up research, where similar tests will be performed for a bench-scale CSB reactor facility in the third phase for syngas production.

6.1 Summary

The main purpose of studying cold flow model of conical spouted bed system is to investigate the hydrodynamic behavior of a small, laboratory scale, conical spouted bed (CSB) by considering the effect of specific system parameters (stagnated bed height, particle size and inlet diameter) on minimum spouting velocity $(u_{ms})_o$, stable operating pressure drop (ΔP_{ms}) and maximum pressure drop (ΔP_M). Knowledge of the minimum spouting velocity (u_{ms}) is of fundamental importance in the design and operation of spouted beds. Minimum spouting velocity and pressure drop over the bed are major parameters for a spouted bed system, which are used for sizing of bed dimensions and selection of auxiliary equipment. The minimum spouting velocity is the minimum gas velocity needed to maintain spouting operation. Experimental results show fair agreement with correlations for $(u_{ms})_o$ available in existing literature. Using experimental data, an alternative correlation for minimum spouting velocity is developed.

Thermodynamic equilibrium analysis for homogeneous fuel reforming processes Viz. DR, POX, SR and ATR provides information that is useful for the assessment of a combustion process as well as a valuable tool to obtain some insights into the potential of non-catalytic reforming. Equilibrium calculations use an idealized thermodynamic state with maximum entropy to predict the composition of the reacted mixture. This state requires infinite residence time for all chemical reactions to complete, which in actual practice it is not feasible. Therefore, it restricts equilibrium calculations to qualitative predictions. The thermodynamic equilibrium solver is used as a reference tool to qualitatively choose operating conditions such as pressure, temperature and reactants feed ratio irrespective of reaction kinetics, reactor design and operation.

Tests from the plug flow reactor hot flow experimental studies are used to assess product species concentration (vol%) and conversion efficiencies for major species (H_2, CO, C_3H_8 etc.) for homogeneous DR, POX, SR and ATR. The experimental data is quantitatively obtained from gas chromatogram system. The data includes product species concentration for major as well as minor species. The reactor performance in terms of fuel conversion efficiency, hydrogen and carbon monoxide production efficiency for each homogeneous reforming process is evaluated experimentally and compared with thermodynamic equilibrium analysis. In addition, a non-noble metal catalyst (CeO_2 promoted Ni/Al_2O_3) is prepared by using standard impregnation method. The preliminary results for heterogeneous ATR are presented which determine the feasibility of heterogeneous fuel reforming for future work of catalytic thermochemical energy conversion routes. Results from this study will lay the foundation for follow-up research, where similar tests will be performed over wide variety of fuels for a bench-scale CSB reactor facility for syngas production.

6.2 Conclusion

The thesis focused on the development of a laboratory scale conical spouted bed (CSB) reactor for the purpose of producing hydrogen rich syngas from a variety of fuel feed including liquid biomass such as glycerol and hydrocarbon fuels. Hydrogen and synthesis gas (mixture of hydrogen and carbon monoxide) production via thermochemical technologies can utilize energy more efficiently, eliminate pollutant emissions and significantly cut emissions of greenhouse gases. Syngas production can contribute to more efficient electrical power generation through advanced energy systems, such as Integrated Gasification

Combined Cycle (IGCC) and high temperature fuel cells. Syngas is considered as an important intermediate product for further syntheses to produce valuable clean transportation fuels. Hydrogen has been attracting great interest as a major source of eco-friendly future clean fuel for small and portable power applications including combustion engines, gas turbines and fuel cells.

The development of CSB reactor system involves three phases: the cold flow model facility in the first phase studied hydrodynamic behavior of a CSB reactor, the second phase involved a simpler plug flow reactor facility which is used for an evaluation of favorable operating conditions for hydrogen rich syngas generation. The plug flow reactor allowed for a detailed characterization of reforming conditions in terms of temperature and gasification regime, i.e. dry reforming (DR), partial oxidation (POX), steam reforming (SR) and auto-thermal reforming (ATR). For validation purposes, experiments used propane as a supplying fuel, while additional tests will use glycerol as a renewable fuel source. The selection of operating conditions is guided by results from thermodynamic analysis. The third phase includes the follow-up research where similar tests will be performed for a bench-scale CSB reactor facility.

Minimum spouting velocity and pressure drop over the bed are the major parameters for a spouted bed system, which are used for sizing of conical spouted bed (CSB) dimensions and selection of auxiliary equipment. The cold flow conical spouted bed model study presents results for the hydrodynamic behavior of a laboratory scale conical spouted bed. In experiments, minimum spouting velocity $(u_{ms})_o$, pressure drop under stable spouting operating ΔP_{ms} and maximum pressure drop ΔP_M were determined for varying stagnated bed heights (H_o). A test matrix with three different inlet diameters (D_o) and two mean alumina particle sizes (d_p) yielded six data sets. Experimental results verified that $(u_{ms})_o$ increases with increasing particle size (d_p) and increasing stagnation bed height (H_o), whereas it decreases for increasing D_o. A comparison of experimental data to results from correlations for $(u_{ms})_o$ that are available in literature revealed that, while trends were predicted correctly, values showed significant deviations. All available correlations showed relative errors (RE) in excess of 50% for at least one out of the six available data sets. An analysis of the results revealed that predicted values appear to be dependent on the particle size and inlet diameter, which indicates an insufficient number of dimensionless parameters in existing correlation. As an alternative, a simple empirical correlation for $(u_{ms})_o$ was fitted to the six available experimental data sets taken for cold flow study, where an additional non-dimensional param-

eter relating particle size to inlet diameter was included. While additional tests using varying particle densities and cone angles are required for the development of a universally applicable correlation for small sized conical spouted beds, results from the new correlation show a drastic improvement of prediction quality. Predicted values show excellent agreement for all available experimental data with varying inlet diameters, particle sizes and stagnated bed heights.

Thermodynamic equilibrium analysis for homogeneous fuel reforming processes Viz. DR, POX, SR and ATR provided information that is useful for the assessment of a combustion process as well as a valuable tool to obtain some insights into the potential of non-catalytic reforming. The equilibrium calculations used an idealized thermodynamic state with maximum entropy to predict the composition of the reacted mixture. This state requires infinite residence time for all chemical reactions to complete, which in actual practice it is not feasible. Therefore, it restricted equilibrium calculations to qualitative predictions. The thermodynamic equilibrium solver was used as a reference tool to qualitatively choose operating conditions such as pressure, temperature and reactants feed ratio irrespective of reaction kinetics, reactor design and operation.

A thermodynamic equilibrium analysis in context with ternary system was used as a tool to find out an optimum reactants feed ratios at which carbon free reactions are feasible without harming the reaction system. From thermodynamic equilibrium analysis for homogeneous propane reformings study, it was noted that lower pressure favors the formation of H_2 . In the present study, atmospheric pressure was preferred for all experimental tests. It was noted that H_2 production efficiency for POX reforming always appears higher than DR of propane for the entire temperature. Maximum H_2 production appeared in ATR whereas minimum appears in DR. It was also observed that the overall production of hydrogen is always higher in ATR ($\eta_{|H_2}$= 92 ~ 128%) as compared to SR ($\eta_{|H_2}$= 50 ~ 119%), POX ($\eta_{|H_2}$= 70 ~ 82%) and DR ($\eta_{|H_2}$= 48 ~ 80%). The H_2 production efficiency for SR and ATR appeared greater than 100% because of addition of H_2 into H_2O. Therefore, the order of H_2 production is ATR > SR > POX > DR. The CO production efficiency increased with temperature for POX (18 ~ 35%), SR (2 ~ 45%) and ATR (21 ~ 73%). The increase of CO with temperature for POX, SR and ATR processes was due to the methanation reaction predominance over water gas shift reaction. Carbon was increased with temperature for DR whereas decreased with increasing temperature for POX, SR and ATR processes.

Carbon formation appeared almost constant after 850º C for DR (~ 80%) and PO (~ 48%). On the other hand, the carbon formation continuously decreases for ATR process and vanishes after 730º C temperature. It was concluded that the ATR is the most clean process whereas DR is the least clean process in terms of carbon formation among all four processes considered in the present study. In other words, the carbon formation increasing order for propane reforming process is ATR < SR < POX < DR. The 100% propane conversion efficiency in thermodynamic analysis for all reforming processes at entire temperature range is attributed to its tendency to its complete dissociation even at at temperature 500°C into hydrogen, carbon and methane along negligible amount of acetylene and ethane.

Propane conversion efficiency for homogeneous DR process (experiment) increased from 10.6% to 96% with temperature. The maximum propane conversion efficiency achieved in homogeneous DR process is 96% at 1000 °C. This indicates that hydrogen containing species such as C_2H_2, CH_4 and H_2 simultaneously increase with temperature, since propane breaks down at higher temperatures into lower hydrogen containing species (C_2H_2, CH_4, H_2 etc.). The maximum propane conversion efficiency for POX is 100% achieved at 900°C. Propane conversion efficiency for homogeneous SR process continuously increased from 2 to 100% with temperature increase from 600 to 1000°C. The experimental propane conversionefficiency for the homogeneous ATR process always appeared higher than DR, POX and SR, and it continuously increased from 10 to 100% with temperature increase from 600 to 900°C. It becomes stable above 900°C. The overall propane conversion efficiency trend for homogeneous propane reforming processes is ATR > POX > SR > DR.

It was noted that the hydrogen production efficiency always appeared higher in the thermodynamic equilibrium predictions as compared to experiments for homogeneous DR, POX, SR and ATR. This difference is due to the formation of acetylene and ethane in actual tests whereas negligible amount of them appeared in the thermodynamic equilibrium calculations. It was also seen that the hydrogen production efficiency for the homogeneous ATR always appears higher than all other propane reforming processes for both thermodynamic equilibrium analysis and actual tests. Also, the lowest hydrogen production efficiency appears in propane dry reforming and hydrogen production efficiencies for POX and SR stay between efficiencies of ATR and DR processes. In other words, the most efficient homogeneous propane reforming process has the order of ATR > POX > SR > DR for actual tests whereas for thermodynamic

predictions the order is ATR > SR > POX > DR. This difference is attributed to the absence of CO in actual homogeneous steam reforming process whereas a significant amount of CO appears in thermodynamic analysis for steam reforming. This leads to different behavior of water-gas shift reaction in thermodynamic calculations and actual tests. The maximum hydrogen production efficiency achieved at 1000°C in actual homogeneous reforming in DR is 24% whereas 28% for SR, 30% for POX and 32.5% for ATR. The reason for lower hydrogen production efficiency is due to formation of other hydrocarbon species in large amounts such as methane, acetylene and fraction of ethane. The CO production efficiency for homogeneous DR process is zero at all temperatures, because of absence of oxygen in reactant stream. The CO production efficiency linearly increases for SR and ATR whereas it increases for POX upto 800°C and it did not change much afterward. However, CO production efficiency behavior is very similar in homogeneous POX and ATR processes i.e. linearly increases with temperature. CO production efficiency always appear lower in homogeneous POX and ATR process than in thermodynamic predictions. This is due to the formation of large amount of small hydrocarbon species such as CH_4, C_2H_2 and small fraction of C_2H_6 in the product stream for actual POX and ATR processes and therefore, there is less tendency for the reaction of oxygen with carbon in propane to produce CO and CO_2. No CO appears in actual homogeneous steam reforming tests.

6.3 Recommendations and Future Work

Cold Flow Hydrodynamic Studies: The results from the new proposed correlation for calculating minimum spouting velocity for small sized conical spouted beds show a drastic improvement of prediction quality, additional tests using varying particle densities and cone angles are required for the development of a universally applicable correlation. The time to take measurements for pressure drops and flow rates for cold flow study of CSB system as well as their measurement uncertainties could be reduced by using more sophisticated data acquisition (DAQ) system. The DAQ device could control pressure transducer to record pressure drop readings and at the same time it could also control the digital mass flow controller to precisely control the flow of air upstream to the CSB.

Gas Chromatography System: Helium was used as a carrier gas for quantitative analysis of product stream species in gas chromatographic system as it has a higher thermal conductivity compared to most organic compounds; thus, yielding larger thermal conductivity detector (TCD) responses than nitrogen

and argon carrier gases. Helium is most often used with TCD detectors due to its high thermal conductivity (343 W/m-K) compared to most organic compounds; thus yielding larger TCD responses than nitrogen (57 W/m-K) and argon (39 W/m-K) carrier gases. Given that the thermal conductivity of helium is close to the thermal conductivity of hydrogen (419 W/m-K), the peak area of H_2 in the He carrier gas was appeared small. If argon was used as a carrier gas instead of helium in order to detect hydrogen, then the detection of CO, CH_4, O_2 and CO_2 would have to be sacrificed, as their thermal conductivities are similar to that of argon. Since nitrogen is one of the major reactant species (dilution agent) for propane reforming processes, nitrogen as a carrier gas for TCD system is obviously not a wise option. If argon career gas could be used in future and detection of small peak areas could be improved by using external methanizer. The CO and CO_2 are converted to methane while passing through the mechanize. Hydrocarbons such as ethane, propane, etc. pass through the mechanize unaffected. Because the CO and CO_2 are converted to methane, they can be detected by the FID down to 1 ppm. Intermittent water accumulation into the GC sample line was observed during steam and auto-thermal reforming processes, because vapors condensation at room temperature. This vapor condensation could be avoided by maintaining sample line temperature close to 60°C temperature of sample valve oven box situated inside GC. This could be achieved by wrapping heating tape onto the sample line prior to the gas chromatography system.

Heterogeneous Reforming: A non-noble catalyst (15 wt% CeO_2- promoted Ni/Al_2O_3) preparation method and preliminary tests for heterogeneous ATR process are discussed in Chapter 5, however more samples of catalyst with different CeO_2 and Ni loadings on Al_2O_3 metal support need to be prepared and tested to access the detailed charaterization of catalysts performance for heterogeneous DR, POX, SR and ATR processes.

Construction of a Bench Top CSB Reactor: The third phase of CSB reactor facility eventually involves construction of a bench top laboratory scale CSB for the follow-up research where similar tests needs to be performed. The spouted bed reactor will be heated externally to account for heat requirements. Solid and liquid product yields will be assessed quantitatively by filters/traps, whereas a detailed analysis of gaseous products will be obtained from the gas chromatography measurements.

References

[1] S. Ahmed and M. Krumpelt. Hydrogen from hydrocarbon fuels for fuel cells. *Int. J. Hydrogen Energy*, 26:291–301, 2001.

[2] Z. Al-Hamamre, S. Voß, and D. Trimis. Hydrogen production by thermal partial oxidation of hydrocarbon fuels in porous media based reformer. *Int. J. Hydrogen Energy*, 34:827–832, 2009.

[3] S. Aravinth and T. Murugesan. A general correlation for the minimum spouting velocity. *Bioprocess Engineering*, 16:289–293, 1997.

[4] S. Ayabe, H. Omoto, T. Utaka, R. Kikuchi, K. Sasaki, Y. Teraoka, and K. Eguchi. Catalytic autothermal reforming of methane and propane over supported metal catalysts. *Applied Catalysis A: General*, 241:261–269, 2003.

[5] S. P. Babu. Thermal gasification of biomass technology development: End of task report for 1992 to 1994. *Biomass and Bioenergy*, 9:5–15, 1995.

[6] V. A. Bansode. Partial oxidation of propane on ceria-and alumina-supported platinum catalysts. Master's thesis, West Virginia University, 2006.

[7] A. M. Beenackers. Biomass gasification in moving beds, a review of european technologies. *Renewable Energy*, 16:1180–1186, 1999.

[8] H. T. Bi. A discussion on minimum spout velocity and jet penetration length. *The Canadian Journal of Chemical Engineering*, 82:1–7, February 2004.

[9] H. T. Bi, A. J. Chaouki, and R. Legros. Minimum spouting velocity of conical spouted beds. *Can. J. Chem. Eng.*, 75:460–465, 1997.

[10] A. V. Bridgwater. Renewable fuels and chemicals by thermal process of biomass. *Chem. Eng. J.*, 91:87–102, 2003.

[11] A. J. Byrd, K. K. Pant, and R. B. Gupta. Hydrogen production from glycerol by reforming in supercritical water over Ru/Al_2O_3 catalyst. *Fuel*, 87:2956–2960, 2008.

[12] M. Castaldi, M. Lyubovsky, R. LaPierre, W. C. Pfefferle, and S. Roychoudhury. Performance of microlith based catalytic reactors for an isooctane reforming system. Number 2003-01-1366. SAE International, 2003.

[13] M. Choi and A. Meisen. Hydrodynamics of shallow conical spouted beds. *Can. J. Chem. Eng.*, pages 916–924, 1992.

[14] W. C. Chueh, Z. Shao, and S. M. Haile. Tunability of propane conversion over alumina supported pt and rh catalysts. *Top Catal*, pages 1–12, 2007.

[15] H. Cui and J. R. Grace. Spouting of biomass particles: A review. *Bioresource Technology*, 99:4008–4020, June 2008.

[16] K. M. Dooley, A. K. Bhat, C. P. Plaisance, and A. D. Roy. Methylketones from acid condensation using metal/CeO_2 catalysts. *Applied Catalysis A: General*, 320:122–133, 2007.

[17] N. Epstein, C. J. Lim, and K. B. Mathur. Data and models for flow distribution and pressure drop in spouted beds. *Can. J. Chem. Eng.*, 56:436–447, 1978.

[18] Norman Epstein and John R. Grace. *Spouted and Spout-Fluid Bed, Fundamental and Applications*. Cambridge University Press, 2011 edition, 2011.

[19] T. H. Gardner, J. J. Spivey, A. Campos, J. C. Hissam, E. L. Kugler, and A. D. Roy. Catalytic partial oxidation of CH_4 over $Ni-substituted$ barium hexaaluminate catalysts. *Cataysis Today*, 157, Issue 1-4:166–169, 2010.

[20] A. D. Goltsiker. *Spouted Bed System*. PhD thesis, Lensovet Technology Institute, Leiningrad, 1967.

[21] D. G. Goodwin. Cantera. `http://www.cantera.org`, 2002-2007.

[22] A. E. Gorshtein and I. P. Mukhlenov. Hydraulic resistance of a fluidized bed in a cyclone without a grate. critical gas rate corresponding to the beginning of jet formation. *Zh. Prikl. Khim. (Leningrad)*, 37(9):1887 – 1893, 1964.

[23] A. L. Guimaraes, L. C. Dieguez, and M. Schmal. Surface sites of $Pd/CeO_2/Al_2O_3$ catalysts in the partial oxidation of propane. *Journal of . Physical Chemistry B*, 107:4311–4319, 2003.

[24] D. Halliche, R. Bouarab, O. Cherifi, and M. M. Bettahar. Carbon dioxide reforming of methane on modified Ni/alpha-Al_2O_3 catalysts. *Catalyst Today*, 29:373–377, 1996.

[25] K. M. Hardiman, T. T. Ying, A. A. Adesina, E. M. Kennedy, and B. Z. Dlugogorski. Performance of a Co-Ni catalyst for propane reforming under low steam-to-carbon ratios. *Journal of Chemical Engineering*, 102:119–130, 2004.

[26] D. J. Haynes, A. Campos, M. W. Smith, D. A. Berry, D. Shekhawat, and J. J. Spivey. Reducing the deactivation of *Ni*-metal during the catalytic partial oxidation of a surrogate diesel fuel mixture. *Catalysis Today*, 154:210–216, 2010.

[27] M. Huff, P. M. Torniainen, and L. D. Schmidt. Partial oxidation of alkanes over noble metal coated monoliths. *Catalysis Today*, 21:113–128, 1994.

[28] M. J. S. Jose, M. Olazar, A. T. Aguayo, J. M. Arandes, and J. Bilbao. Expansion of spouted beds in conical contactors. *J. Chem. Eng.*, pages 45–52, 1993.

[29] M. K. Karmakar and A. B. Datta. Generation of hydrogen rich gas through fluidized bed gasification of biomass. *Bioresource Technology*, 2010.

[30] A. Kmiec. The minimum spouting velocity in conical beds. *The Canadian Journal of Chemical Engineering*, 61:274–280, June 1983.

[31] G. Kolb, R. Zapf, V. Hessel, and H. Lowe. Propane steam reforming in micro-channels: Results from catalyst screening and optimisation. *Applied Catalysis A: General*, 277:155–166, 2004.

[32] N. Laosiripojana, W. Sangtongkitcharoen, and S. Assabumrungrat. Catalytic steam reforming of ethane and propane over $CeO_2-dopedNi/Al_2O_3$ at sofc temperature: Improvement of resistance toward carbon formation by the redox property of doping CeO_2. *Fuel*, 85:323–332, 2006.

[33] N. Laosiripojana, W. Sutthisripok, and S. Assabumrungrat. Synthesis gas production from dry reforming of methane over $CeO_2 - \text{doped}Ni/Al_2O_3$: Influence of the doping ceria on the resistance toward carbon formation. *Chemical Engineering Journal*, 112:13–22, 2005.

[34] J. H. Lee and D. L. Trimm. Catalytic combustion of methane. *Fuel Processing Technology*, 42:339–359, 1995.

[35] X. Li, J. R. Grace, A. P. Watkinson, C. J. Lim, and A. Ergudenler. Equilibrium modeling of gasification: A free energy minimization approach and its application to a circulating fluidized bed coal gasifier. *Journal of Fuel*, 80:195–207, 2001.

[36] J. A. Liu. Kinetics, catalysis and mechanism of methane steam reforming. Master's thesis, Worcester Polytechnic Institute, 2006.

[37] K. Liu, C. Song, and V. Subramani. *Hydrogen and Syngas Production and Purification Technologies*. John Wiley & Sons Publications, 2010.

[38] B. Lounsbury, K. Leichliter, J. Steciak, and S. Beyerlein. Catalytic ignition temperatures of propane-oxygen-nitrogen mixtures over platinum. Technical report, National Institute for Advanced Transportation Technology University of Idaho, 2007.

[39] A. Markowski and W. Kaminski. Hydrodynamic characteristics of jet spouted beds. *Can. J. Chem. Eng.*, 61:377–381, 1983.

[40] D. J. Moon, J. W. Ryu, S. D. Lee, B. G. Lee, and B. S. Ahn. Ni-based catalyst for partial oxidation reforming of iso-octane. *Applied Catalysis A: General*, 272:53–60, 2004.

[41] Dahl IM Olsbye U Schuurman Y Olafsen A, Slagtern A and Mirodatos C. Mechanistic features for propane reforming by carbon dioxide over a ni/mg(al)o hydrotalcite-derived catalyst. *J Catalysis*, 229:163–175, 2005.

[42] M. Olazar, R. Aguado, M. J. San Jose, S. Alvarez, and J. Bilbao. Minimum spouting velocity for the pyrolysis of scrap tyres with sand in conical spouted beds. *Powder Technology*, 165:128–132, 2006.

[43] M. Olazar, M. J. San Jose, A. T. Aguayo, J. M. Arandes, and J. Bilbao. Stable operation conditions for gas-solid contact regimes in conical spouted beds. *Ind. Eng. Chem. Res.*, 31:1784–1792, 1992.

[44] L. B. Raberg, M. B. Jensena, U. Olsbye, C. Daniel, S. Haag, C. Mirodatos, and A. O. Sjastad. Propane dry reforming to synthesis gas over ni-based catalysts: Influence of support and operating parameters on catalyst activity and stability. *Journal of Catalysis*, 249:250–260, 2007.

[45] A. S. K. Raju, C. S. Park, and J. M. Norbeck. Synthesis gas production using steam hydrogasification and steam reforming. *Fuel Processing Technology*, 90, Issue 2:330–336, 2009.

[46] I. Schoegl. *Superadiabatic Combustion in Counter-Flow Heat Exchangers*. PhD thesis, The University of Texas at Austin, 2009.

[47] I. Schoegl and J. L. Ellzey. Superadiabatic combustion in parallel channels. In *Joint Meeting of the U.S. Sections of the Combustion Institute*, 2007.

[48] I. Schoegl and J. L. Ellzey. A mesoscale fuel reformer to produce syngas in portable power systems. In *Spring Meeting of the Western States Section of The Combustion Institute*, 2008.

[49] I. Schoegl, S. R. Newcomb, and J. L. Ellzey. Ultra-rich combustion in parallel channels to produce hydrogen-rich syngas from propane. *Int. J. Hydrogen Energy*, 34:5152–5163, 2009.

[50] M. Sharma, M. Lousteau, and I. Schoegl. An experimental study of small-sized conical spouted beds. *ASME Early Career Technical Journal*, 10:149–155, 2011.

[51] B. Silberova, H. J. Venvik, and A. Holmen. Production of hydrogen by short contact time partial oxidation and oxidative steam reforming of propane. *Catalysis Today*, 99:69–76, 2005.

[52] G. P. Smith, D. M. Golden, M. Frenklach, N. W. Moriarty, B. Eiteneer, M. Goldenberg, C. T. Bowman, R. K. Hanson, S. Song, Jr. W. C. Gardiner, V. V. Lissianski, and Z. Qin. GRI-Mech 3.0. `http://www.me.berkeley.edu/gri_mech/version30/`, 1999.

[53] X. Song and Z. Guo. Technologies for direct production of flexible H_2/CO synthesis gas. *Energy conversion and Management*, 47:560–569, 2006.

[54] V. Subramani, P. Sharma, and L. Zhang. Catalytic steam reforming technology for the production of hydrogen and syngas. *Book Chapter 2, Hydrogen and Syngas Production and Purification Technologies, AlChE, Whiley and Sons*, pages 14–126, 2010.

[55] F. Wan-Fyong, P. G. Romankov, and N. B. Rashkovskaya. Research on hydrodynamics of the spouting bed. *Zh. Prikl. Khim*, 42(3):377–381, 1969.

[56] S. Wang and G. Q. (Max) Lu. Role of $CeO_2 in Ni/CeO_2 - Al_2O_3$ catalysts for carbon dioxide reforming of methane. *Applied Catalysis B: Environmental*, 19:267–277, 1998.

[57] X. Wang, N. Wang, and L. Wang. Hydrogen production by sorption enhanced steam reforming of propane: A thermodynamic investigation. *International Journal of Hydrogen Energy*, 36:466–472, 2011.

[58] X. Wang, N. Wang, J. Zhao, and L. Wang. Thermodynamic analysis of propane dry and steam reforming for synthesis gas or hydrogen production. *International Journal of Hydrogen Energy*, 35:12800–12807, 2010.

[59] X. Wang, N. Wang, J. Zhao, and L. Wang. Thermodynamic analysis of propane dry and steam reforming for synthesis gas or hydrogen production. *International Journal of Hydrogen Energy*, 35:12800–12807, 2012.

[60] Y. Wang, Y. H. Chin, R. T. Rozmiarek, B. R. Johnson, Y. Gao, J. Watson, A. Y. L. Tonkovich, and D. P. Vander Wiel. Highly active and stable $Rh/MgO\text{-}Al_2O_3$ catalysts for methane steam reforming. *Cat. Today*, 98:575–581, 2004.

[61] F. J. Weinberg, T. G. Bartleet, F. B. Carleton, P. Rimbotti, J. H. Brophy, and R. P. Manning. Partial oxidation of fuel-rich mixtures in a spouted bed combustor. *Combust. Flame*, 72:235–239, 1988.

[62] L. Zhang, X. Wang, B. Tan, and U. S. Ozkan. Effect of preparation method on structural characteristics and propane ssteam reforming performance of Ni/Al_2O_3 catalysts. *Journal of Molecular Catalysis A: Chemical*, 297:26–34, 2009.

Appendix A
Experimental Procedure and Performance Evaluation

A.1 Instruments Detail for Experimental Setup

The gaseous fuel, nitrogen and air are mixed prior to the reactor in a connector which has four openings; one for propane/nitrogen and second for air whereas the third outlet is connected to thermocouple (TC as shown in Figure 4.1) and fourth one is for outlet mixture upstream to the reactor. The air supply is shut off when the only dry reforming of propane tests are required. The unit has three lines for gas feeds, each being independently controlled by digital mass-flow controllers (models # EW-32907-57, EW-32907-61 and EW-32907-63 for fuel, air and nitrogen respectively, COLE-PARMER). All the three MFCs are connected to shut-off valves prior connecting feed gases supply to it. A quartz tubular-flow reactor having length 495 mm, inner diameter 6.35 mm and outer diameter of 6.70 mm, is placed inside a single zone electrically heated furnace (# TF55030A, LINDBERG/BLUE M mini mite tube furnace, 120 V) of maximum temperature range upto 1100º C. A quartz reactor is preferred than stainless steel reactor in order to visualize the coke formation or soot accumulation if any. The ends of a quartz reactor are connected to pyrex tube pieces (length 50 mm, inner diameter 6.35 mm) by two stainless steel clips for easy and quick connections with feed gases supply line as well as reformed gas stream. A special care is taken in order to provide and maintain leak proof tight fittings at all possible connections. For this purpose, an FKM high temperature O-rings (# FCBR-90-OR-508, SWAGELOK) are sandwiched between main quartz reactor tube and pyrex tubes, and also ultra-torr vacuum union (# SS-4-UT-6-400, SWAGELOK) fittings are used to connect pyrex glass tubings with their stainless steel counterparts. The furnace temperature is controlled and monitored by an inbuilt temperature controller. Two firm steel supports are provided at both ends in order to adjust the position as well as to support the reactor tube inside the furnace. A carbon monoxide alarm is also mounted for safety concerns, since the exhaust gas consists of syngas, which mainly consists of H_2 and harmful CO in high proportions. All the experiments were carried out under the hood. Safety goggles and laboratory coat are necessary all the time during experiment.

During preliminary tests with SR and ATR, it was observed that the water was accumulated in the COLE-PARMER PTFE non-sterile syringe filters (used in DR and POX), which caused flow blockage in the sample probe and due to which an insufficient peaks were observed. Since, it is well known fact that SR and ATR processes are clean as compared to DR and POX reforming reactions, a separate shut-off valve (Figure 4.2) is provided in the bypass line of the exhaust stream instead of using non-sterile syringe filters. When the system is idle i.e. no propane flow is sent to the system, the shut-off valve is turned on in order to remove water accumulation, which is trapped during SR and ATR test runs, without compromising the reactor system atmospheric pressure conditions.

A total eight thermocouples (labeled as TC in Figure 4.1) are used in the reactor system, one is located at mixture inlet location where all feed gases mix together upstream of the reactor whereas the three thermocouples are inserted at inlet, middle and outlet locations into the annulus space between the reactor and the furnace in order to measure reactor outer wall temperatures and mixture outlet location. The thermocouples at inlet and outlet positions within the furnace are at 5 inches apart from the middle thermocouple, and on an average, a difference of around 50 ~ 80º C is recorded between thermocouples at inlet and outlet positions with the central one. One thermocouple is located at a position where a sample is taken for quantitative analysis of reformed gas from the exhaust. The sixth thermocouple is provided to the pyrex outlet piece in order to verify that its temperature is below its maximum temperature range of 100º C. The seventh thermocouple is attached to the heating tape for steam reforming process (refer Figure 4.2) in order to monitor its temperature whereas the last thermocouple is inserted inside of the flask (Figure 4.2) for the purpose to monitor water temperature. All these thermocouples and the digital mass flow controllers are connected with a multifunction data acquisition (DAQ) device (NI USB-6216, NATIONAL INSTRUMENTS). This device has 16 analog inputs and 2 analog output channels, which is sufficient to monitor all the thermocouples and to control upto two mass flow controllers whereas a second DAQ device (NI USB-6009, NATIONAL INSTRUMENTS), however, is used to control the mass flow controller for air supply as required in partial oxidation as well as in autothermal reforming processes. All the acquisition data is recorded and saved in a computer.

A.2 Experimental Detailed Procedure

First of all, a pressure drop leak test was performed prior switching on the furnace in order to make sure all the flow lines are leak proof. The desired temperature in the furnace was set through in-built temperature controller. Furnace and GC system both were run to reach and stabilize at their desired temperatures. It took one hour for the whole system to reach steady state. After a steady temperature was achieved, nitrogen gas at desired flow rate supplied by a mass flow controller was passed through the system. Prior running reforming tests, it was important to verify there was only one gas (nitrogen) is flowing through the system. This was verified by sending a sample through sample line to the GC system. It took 36 minutes for the GC 8610C to analyze each sample. Then, propane gas at required flow rate was mixed with nitrogen upstream to the reactor for DR tests. Air, however, was supplied at set flow rate before adding propane during POX reactions. On the other hand, for SR tests, nitrogen was first entered to the bubbler section and a mixture of nitrogen and vapors mixed with propane prior supplying feed upstream to the reactor. Same set-up of SR except additional air was used for ATR tests. All the experiments were conducted at atmospheric pressure and at temperatures ranging from 500 to 1000 °C. A mixture flow rate of 495 mlpm was selected based on preliminary tests with DR of propane as well as maximum flow rate range of available mass flow controllers. And correspondingly, the GHSV (gas hourly space velocity) of 2763.63 h^{-1} and gas residence time of 1.30 s is used for all homogeneous as well as heterogeneous reforming reactions of propane studied in the present investigation. The operating parameters including reactants feed ratios, pressure and temperature range selection is tabulated in table 3.1. Propane was supplied for a duration of five minutes. Before switching off the propane supply, sample at the exit of the reactor was injected to the GC system for quantitative gas composition analysis. The molar flow rates of the product gases were calculated based on the volumetric gas flow rate and dry gas composition obtained from the GC. The carbon deposits were removed by occasionally interrupting the fuel supply and purging the reactor with air for five minutes, after which the experiment was continued.

First experiments were carried out in an empty bed reactor in order to investigate homogeneous reforming of propane. The heterogeneous reactions, especially SR and ATR, were performed by using 15 wt% CeO_2 promoted 10 wt% Ni/Al_2O_3 catalyst. A catalyst loading of 50 mg each was used for different test cases of reforming. The quartz reactor tube was first loaded with quartz wool before loading

catalyst powder. The additional quartz wool was inserted on the catalyst bed. In this way, the catalyst was sandwiched between quart wool.

In order to assess the uncertainty of the GC measurements, gas analysis was done multiple times (thrice) to get a consistent gas composition. While the uncertainty was calculated for each species in the product stream for each analysis test as the root-sum-square of the contributing uncertainties, error bars were plotted for relative error of the mean for individual species composition.

A.3 Molar Flow Rate and Moles Calculations

Since, the volumetric flow rate of the reactants mixture is fixed i.e. 495 mlpm and correspondingly the the molar flow rates of reactant species can be calculated by using an Ideal gas law:

$$P\dot{V} = \dot{n}RT \tag{A.1}$$

Here,

$$\dot{V} = \frac{495 \times 10^{-3}}{60,000} = 8.25 \times 10^{-6} \quad m^3/s \tag{A.2}$$

By using P = 101325 Pa, R = 8.314 J/mol-K, T = 293 K in eqn. A.1 , the molar flow rate of the mixture can be found out as

$$\dot{n} = 343.157 \times 10^{-6} \quad mol/s \tag{A.3}$$

From the mixture flow rate, the reactants species molar flow rates for each reforming case can easily be find out by multiplying their mole fractions to the molar flow rate of the mixture. For example, the mole fractions of C_3H_8 and N_2 in DR process are 0.091 and 0.909 respectively and therefore their corresponding molar flow rates becomes

$$\dot{n}_{C_3H_8} = \chi_{C_3H_8} \times \dot{n} \tag{A.4}$$

The molar flow rate for nitrogen can be written as

$$\dot{n}_{N_2} = \chi_{N_2} \times \dot{n} \qquad or \qquad \dot{n}_{N_2} = \dot{n} - \dot{n}_{C_3H_8} \tag{A.5}$$

The number of moles of each species (N_i) in the reactant mixture can be easily calculated as

$$N_i = \chi_i \times N_{total} \tag{A.6}$$

The molar flow rate of any species *i* in the product stream is calculated by

$$\dot{N}_{prod} = \chi_{i,\,prod} \times \dot{N}_{tot,\,out} \tag{A.7}$$

The molar flow rates of products is related to the molar flow rate of reactant fuel as [46]

$$\frac{\dot{N}_{prod}}{\dot{N}_{C_3H_8}} = \frac{1}{\chi_i} \frac{\dot{N}_{i,\,prod}}{\dot{N}_{C_3H_8}} \tag{A.8}$$

A.4 Measurable Quantities to Gauge Reactor Performance

Hydrogen conversion efficiency (also equivalent to the reactor yield of hydrogen production from the fuel) is defined as the ratio of molar rate (or moles) of H_2 generated to the maximum molar rate (or moles) of H_2 available in the reactant fuel.

$$\eta_{H_2,\,prod.} = \frac{\dot{N}_{H_2,\,prod.}}{4\dot{N}_{C_3H_8,in}} \times 100\% \tag{A.9}$$

Where, 4 is the maximum number of H_2 atoms bound to propane.

In this way, the CO production efficiency can be calculated by replacing the maximum number of moles of carbon atoms (3 for CO whereas 1.5 for C_2H_2 and C_2H_6 in product species) with that of H_2 atoms present in the reactant fuel.

$$\eta_{CO,\,prod.} = \frac{\dot{N}_{CO,\,prod.}}{3\dot{N}_{C_3H_8,in}} \times 100\% \tag{A.10}$$

The propane conversion, in simple words, is its disappearance during reaction. It can be defined in terms of efficient such as

$$\eta_{C_3H_8,\,conversion} = \frac{\dot{N}_{C_3H_8,in} - \dot{N}_{C3H8,out}}{\dot{N}_{C_3H_8,in}} \times 100\% \tag{A.11}$$

Due to limitations of the gas chromatography system, H_2O content of the syngas, especially in POX, SR and ATR processes is not directly measured. However, the H_2O concentration can be theoretically determined by molar balances of O_2 between reactants and products. For example,

(a) For POX of propane,

$$\dot{N}_{H_2O,\,out} = 2(\dot{N}_{O_2,\,in} - \frac{1}{2}\dot{N}_{CO,\,out} - \dot{N}_{CO_2,\,out} - \dot{N}_{O_2,\,out}) \tag{A.12}$$

(b) For SR of propane,

$$\dot{N}_{H_2O,\,out} = 2(\frac{1}{2}\dot{N}_{H_2O,\,in} - \frac{1}{2}\dot{N}_{CO,\,out} - \dot{N}_{CO_2,\,out} - \dot{N}_{O_2,\,out}) \tag{A.13}$$

(c) For ATR of propane,

$$\dot{N}_{H_2O,\,out} = 2(\frac{1}{2}\dot{N}_{H_2O,\,in} + \dot{N}_{O_2,\,in} - \frac{1}{2}\dot{N}_{CO,\,out} - \dot{N}_{CO_2,\,out} - \dot{N}_{O_2,\,out}) \tag{A.14}$$

The amount of carbon produced in a particular reaction can be theoretically calculated by subtracting number of moles of carbon containing species in the reactant mixture from that of the sum of carbon contained species in the product stream [46].

A.5 Calibration Data

This section shows calibration plots for the instruments used in the present thesis, for example rotameters in cold flow studies and standard gases used in gas chromatography calibrations.

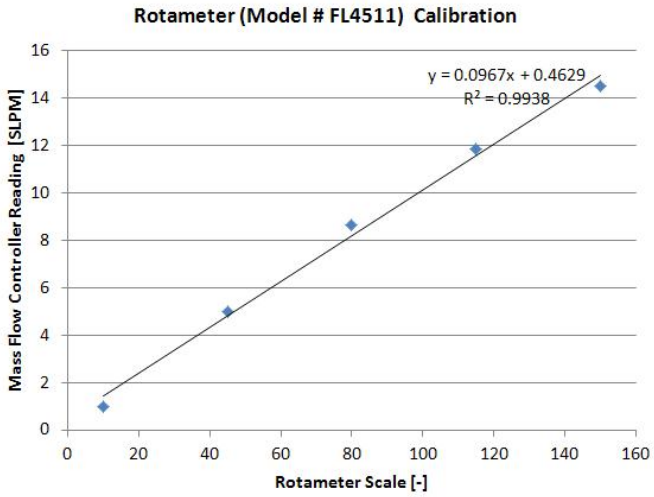

(a) Calibration of rotameter used for fine adjustments in cold flow experiments.

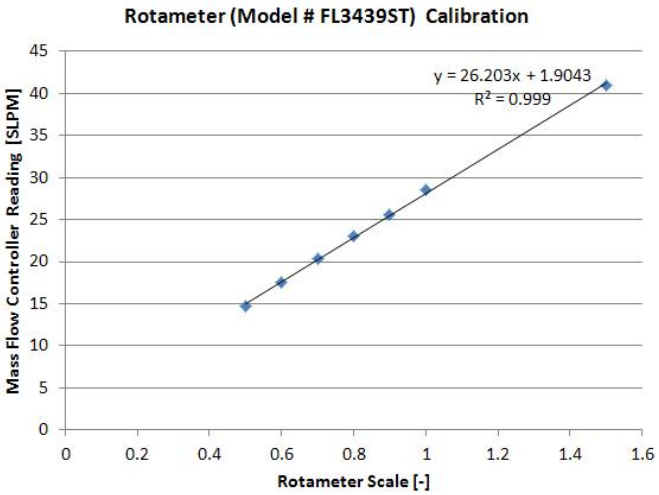

(b) Calibration of rotameter used for coarse adjustments in cold flow experiments.

Figure A.1: Rotameters calibrations.

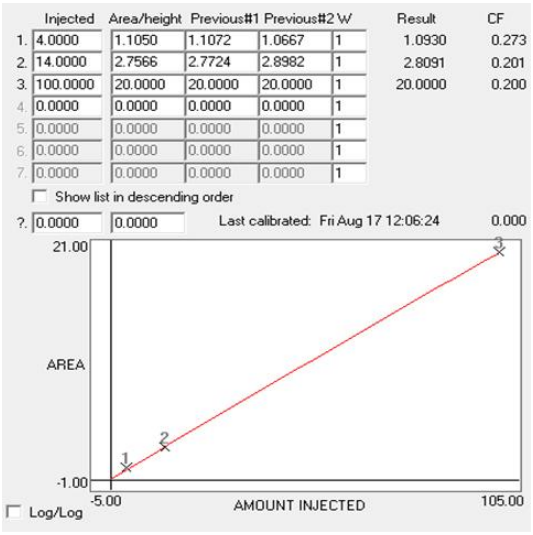

(a) H_2 gas calibration.

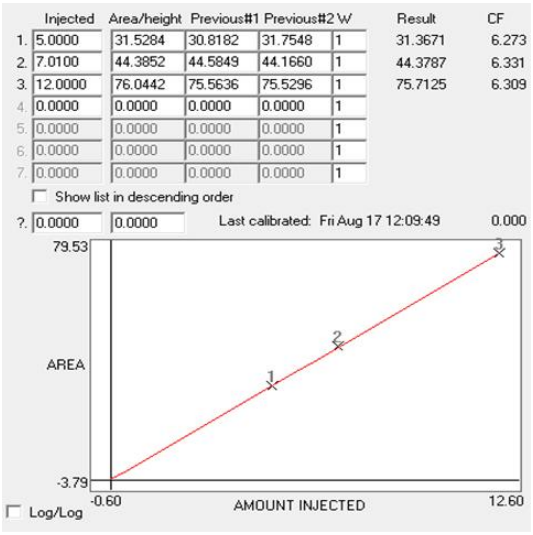

(b) CO gas calibration.

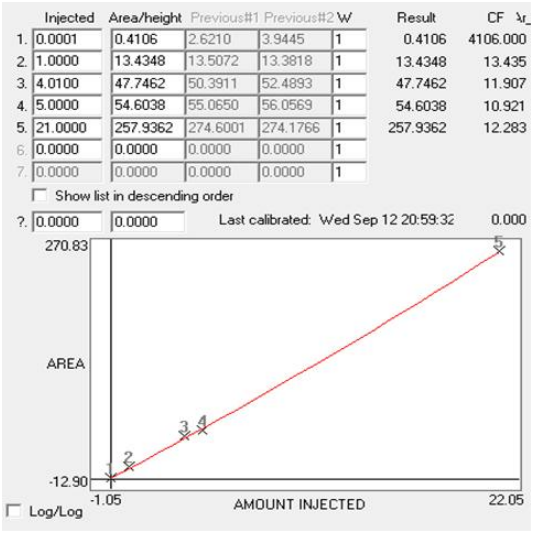

(c) O_2 gas calibration.

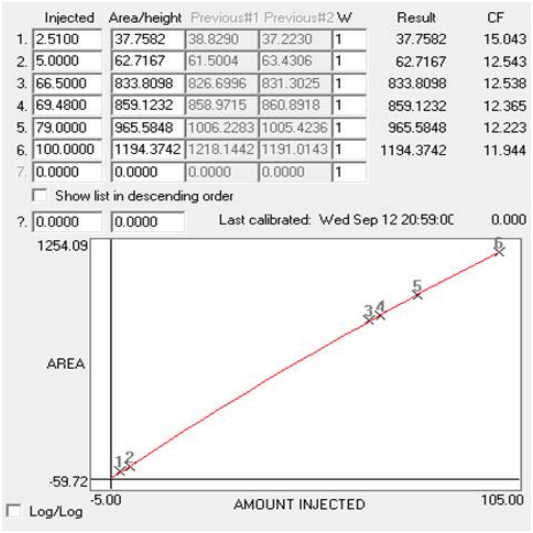

(d) N_2 gas calibration.

Figure A.2: Some of the standard gases calibration samples used for quantitative analysis in GC.

Appendix B
Quantitative Analysis (GC)

The detailed description of gas chromatography system, which includes standard gases calibration, detailed procedure to perform quantitative analysis using GC, retention time of peaks of interest, temperature program and events table, is presented here. Gas chromatography (GC) can be described as a separation process in which volatile organic compounds of a sample separate between a flowing mobile phase (i.e., carrier gas) and a stationary phase (i.e., separation column). The GC used in this study is capable to measure H_2, O_2, N_2, CH_4, CO, CO_2 and C_1 to C_{11} hydrocarbon compounds. The TCD has the ability to detect pure substances such as H_2, O_2, N_2, CO and CO_2 in addition to C_1 to C_{11} hydrocarbon compounds, whereas the FID detects only hydrocarbon species. Both of these detectors are remotely controlled by the Peaksimple software version 388. Although the quantitative analysis tests were done by using both detectors, the TCD and FID, only TCD analysis test results were used as a reference in order to discuss comparisons among each reforming route. As each compound of the separated sample gas passes through the detector, a quantitative response in the form of a peak is generated by the detector signal and a collection of these peaks make up a chromatogram. The detector signal is proportional to the quantity of each analyte. The retention time is the amount of time a compound spends in the separation column. The peak retention time is used to identify each compound and the area under the peak is used to quantify the amount of each compound. The two columns in series are used for separation: a 12' Hayesep D packed column and a 6' Molecular sieve (MS-13X) packed column. The fraction containing H_2, O_2, N_2, CO and CH_4 is detected by a Molecular Sieve column whereas the haysep D packed column determines concentrations of CO_2 and hydrocarbon species such as ethylene, ethane, acetylene, propane, butanes, hexanes, heptanes and octane hydrocarbon species. The exhaust sample is extracted from the reactor with an external GC vacuum pump through an inert Silco steel tubing of 1/16" diameter. The inert Silco tubing is connected between 1/4" diameter SWAGELOK Tee connection and 1/4" OD SWAGELOK shut-off valve. The COLE-PARMER PTFE non-sterile syringe filters with pore size of 0.20μm are used prior injecting samples to the GC inlet port in order to supply clean sample without impurities to the GC for DR and PO cases. A male and female luer lock SWAGELOK adapters are used to connect upstream

and downstream Swagelok reducers for the filter assembly, vacuum pump to create vacuum in the sample line as well in the sample loop of the GC.

B.1 Carrier Gas Selection

The main purpose of carrier gas is to carry the sample through separation column. It is inert and it does not interact with the sample. In measurements with a TCD, suitability of the carrier gas depends on its own thermal conductivity as it is the reference gas flow. Helium is used as a carrier gas for the TCD as it has a higher thermal conductivity compared to most organic compounds; thus, yielding larger TCD responses than nitrogen and argon carrier gases. Helium is most often used with TCD detectors due to its high thermal conductivity (343 W/m-K) compared to most organic compounds; thus yielding larger TCD responses than nitrogen (57 W/m-K) and argon (39 W/m-K) carrier gases. Given that the thermal conductivity of helium is close to the thermal conductivity of hydrogen (419 W/m-K), the peak area of H2 peak in the He carrier gas is small. If argon was used as a carrier gas instead of helium in order to detect hydrogen, then the detection of CO, CH_4, O_2 and CO_2 would have to be sacrificed, as their thermal conductivities are similar to that of argon. Since nitrogen is one of the major reactant species (dilution agent) for propane reforming cases, nitrogen as a carrier gas for TCD system is obviously not a wise option. Thus, for a TCD to be effective in analyzing a gas sample, the thermal conductivities of analytes must be significantly different than that of the carrier gas. Purity of the carrier gas affects the magnitude of the TCD signal. Thus, ultra-pure helium Grade 5.0 (99.999%) was used for both TCD and FID detectors.

B.2 Calibration

To turn the raw area of a peak into a real world number, the peak needs to be calibrated. Two techniques known as internal calibration and external calibration are common to calibrate sample gases. In the present study, external calibration method is used. In this method, Scotty standard calibration gas mixtures were used for hydrocarbons, oxygenated compounds, carbon dioxide, and carbon monoxide. These gas mixtures include:

1. Standard mixture G7 contains argon 1%, hydrogen 14%, nitrogen 66.5%, methane 0.5%, carbon monoxide 12%, carbon dioxide 5% and acetylene 1% (by volume).

Table B.1: Retention time for available standard gas samples for TCD and FID detectors.

Standard Gas Sample	**Retention Time [s] in TCD**	**Retention Time [s] in FID**
H_2	2.803	-
O_2	3.623	-
N_2	4.286	-
CH_4	5.99	6.033
CO	6.183	-
CO_2	8.093	-
C_2H_2	10.306	10.346
C_2H_6	11.303	11.343
C_3H_8	14.746	14.803
i-C_4H_{10}	16.95	17.01
n-C_4H_{10}	17.436	17.496
i-C_5H_{12}	20.16	20.223
n-C_5H_{12}	20.573	20.64
n-C_6H_{14}	25.203	25.243
n-C_7H_{16}	32.05	32.806

2. Standard mixture (given name C for easy identification) contains hydrogen 4%, oxygen 5%, nitrogen 5%, methane 4%, carbon monoxide 5%, carbon dioxide 5% and helium 72% (by volume).

3. Standard mixture (A) contains nitrogen 2.51%, carbon dioxide 3%, ethane 3.48%, propane 1.05%, iso-butane 0.407%, n-butane 0.397%, iso-pentane 0.148%, n-pentane 0.150%, n-heptane 0.0199%, n-hexane 0.0475%, n-octane 0.01% and balance of methane 88.7806 %.

4. Standard mixture (B) contains carbon dioxide 15.0%, carbon monoxide 7.01%, CH4 4.5%, O2 4.01% and N2 69.48%.

A table listing the retention time for each standard gases is mentioned in Table B.1.

B.3 Pressure Drop Leak Test

Pressure drop test is a convenient way to check if there is a leakage in the GC. This test is performed by connecting pressurized N_2 gas sample line from the supply cylinder. Insert a plug at the outlet of MS column into the GC chassis. Run nitrogen at pressure around 20 PSI for 1 to 2 minutes and then turn off the gas cylinder main valve. If there is a significant leakage in the system, pressure on the regulator will start decreasing at faster rate, for instance, pressure will be 0 PSIG within 2-3 minutes. If this is the case, find a point of leakage by inserting plug step by step from exit to entrance of the GC sample line.

If there is no leakage is observed in the system, proceed with the actual test analysis for the GC.

B.4 Procedure to Detect Measurement Samples from GC System

1. Turn on the required gases supply, H_2 and compressed air for FID (Flame Ionization Detector) and Helium carrier gas, before turning ON the GC. Make sure that the gases supply lines (copper tubings) are securely connected to the GC and are leak proof. For best performance, set the incoming gas pressures 5-10 psi higher than the required operating pressures.

2. Check to make sure that the TCD filament current is switched OFF. Plug in and turn ON the GC and open 'peaksimple' software version 388. Verify that the gases flow in the GC channels, FID and TCD, by observing the required pressures at the front panel of the GC. The required pressures for H_2, air and He are 20, 5 and 29 PSI respectively, and their corresponding flow rates are 25, 250 and 20 mlpm. Make sure that the set point and actual pressures are within 1 PSI.

3. Turn the TCD current to LOW position only if the flow of helium carrier gas is observed in the TCD channel, otherwise the TCD channel will be damaged if it runs in the absence of carrier gas. Set the FID amplifier gain switch to HIGH for most applications. If peaks of interest go off the scale (greater than 5000 mV), set the gain switch to MEDIUM. When peaks of interest are 20 seconds wide or more at the base and extra noise immunity is desired, set the gain switch to HIGH (filtered). This setting broadens the peaks slightly.

4. Ignite the FID by holding up the ignitor switch for a couple of seconds until you hear a small POP. The ignitor switch is located on the front panel of the GC. Verify that the FID flame is lit by holding the shiny side of a chromed wrench directly in front of the FID exhaust vent. If condensation becomes visible on the wrench surface, the flame is lit. If you wish to keep the ignitor ON to prevent flameout, set the ignitor voltage to -750 by adjusting the trimpot on the 'FLAME IGNITE' zone with the screwdriver.

5. Set the temperatures for in-built sample valve port, FID detector and TCD cell at 60, 150 and 150 ºC respectively. This can be done by adjusting trimpot settings on the GC chassis. The column oven temperature will be adjusted according to the temperature program requirement. Wait for the GC to be stabilized at these temperature settings.

Table B.2: Temperature program for TCD and FID detectors.

Initial Temp. (°C)	Hold (min.)	Ramp (°C/min.)	Final Temp. (°C)
40	12.80	30	250
250	17.00	00	250

Table B.3: Event table for FID and TCD detectors.

Event	Time (min.)	Switch	Description
Zero	0.00	ON	Auto-zero the detector signal
Sound	0.00	ON	Make a sound to insure the operator
Solenoid valve A	0.10	ON	Supply carrier gas only to MS column
Solenoid valve A	0.30	OFF	Carrier gas flows in both columns
Injection valve G	0.50	ON	Inject sample to 10 ml sample loop
Immediate based integration	0.60	ON	Peak area integration begins immediately
Solenoid valve A	5.85	ON	Stop carrier gas to HAYSEP D column
Solenoid valve A	9.50	OFF	Supply carrier gas to both columns
Injection valve G	9.50	OFF	Sample valve is in LOAD position
Immediate based integration	9.60	ON	Peak area integration begins immediately

6. The column oven temperature program[1] for both FID and TCD channels is set from the peaksimple software as mentioned in Table B.2.

7. The events table[2] as mentioned in Table B.3 is set in the peaksimple software's edit window.

8. Save the temperature program and events table for the entire future analysis tests. Give the convenient name to each test for both FID and TCD channels in the 'postrun' tab in the peaksimple software easy identification in the saved data files. Finally click OK to the channels setting and wait for GREEN signal on the GC to start analysis.

B.5 Sample Injection Scheme

The sample is injected either by following valve injection method or syringe injection method. If the required number of samples are very large, valve injection method is preferable. For this reason, valve

[1]The temperature program is prepared by performing extensive tests for the GC. AS a whole, the temperature program should be prepared in such a way that it should neither take too short time nor too long time for the peaks to elute. If the temperature program duration is too short, peaks co-elute with each other whereas longer temperature duration produces very far away peaks. From the tests, it is observed that the above mentioned temperature setting is appropriate.

[2]The event table is selected after performing extensive tests for the GC. The main part is to adjust the solenoid valve A ON/OFF positions. The solenoid valve should be turn ON between the CH4 and CO2 peaks in order to immobilize the CO2 and heavier peaks in column 1 (HAYSEP - D) while the H2, O2, N2, CH4 and CO peaks elute from column 2 (Molecular Sieve - 13X). Once the CO peak elutes, the valve G should be rotated back to the LOAD position by keeping it OFF (at 9.50 minutes) and also the stop-flow solenoid valve should de-energized at the same time.

injection method is used for our purpose. In this, the sample line, consists of a 1/16" OD steel tubing, 1/4" OD swagelok shut off valve for injecting sample to the GC inlet port when required, 1/4" OD swagelok tee connection which connects the sample line to the reactor exit line without interfering exhaust line flow, Cole-Parmer PTFE non-sterile syringe filters with pore size of 0.20μm in order to supply clean sample without impurities to the GC, male and female luer lock adapters to connect upstream and downstream swagelok reducers for the filter assembly, vacuum pump to create vacuum in the sample line as well in the sample loop of the GC. B.1. A standard procedure is followed for the following two cases:

- Standard gas sample injection: First of all, wait for the green signal on the GC prior to start analysis to make sure that GC is stabilized. No vacuum pump is required for this case, since the standard gas has certain pressure in the cylinder. Turn on sample gas regulator for 15-20 seconds and then immediately turn on the sample line shut off valve until the pressure gauge shows 0 PSIG on the regulator. Wait for another 10 seconds for sample gas to travel through the sample loop inside the GC and to make sure the pressure in both lines, the inlet line and the exit line of GC, is stabilized. Finally, run the GC by hitting space bar from computer where peaksimple software is opened.

- Actual gas sample injection: First of all, check if there is a leakage anywhere in the whole system including reactor, reactants supply unit, products exit unit and sample line of the GC, run nitrogen from pressurized cylinder through reactor system and wait for around 5 minutes to make sure there is a sufficient amount of nitrogen in the system. Then run the GC by following steps mentioned in standard gas sample injection section above. If there is no significant leakage, only one peak for nitrogen should be observed in the chromatogram. Once it is confirmed that there is no leakage in system, proceed with the following steps to analyze actual samples: wait for green signal on the GC before starting any analysis. Run vacuum pump for 5-10 seconds to create a suction in the sample line, since the actual sample is at atmospheric conditions. Turn on the sample line shut off valve for 60 seconds. Immediately run the GC and record data in peaksimle software.

B.6 Baking Test

It is also important to note during analyzing standard sample which includes CO gas that sometimes CO peak does not show into the chromatogram at the end of the analysis test. This indicates that the

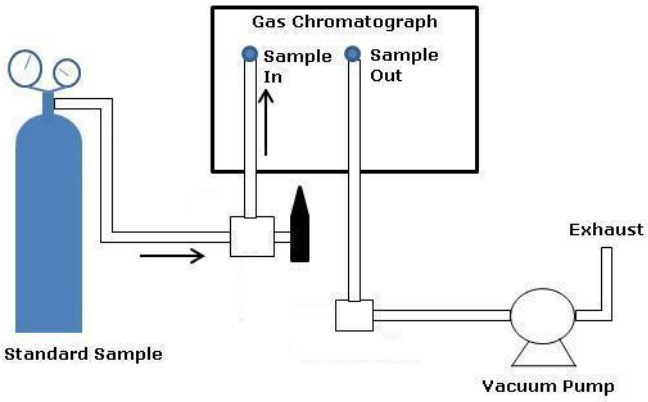

Figure B.1: Gas sampling scheme.

molecular sieve column has unwanted species in it, for e.g. water and it is the time to bake Molecular sieve column at high temperatures for long hours. For this purpose, replace the HAYSEP D column with a small piece (around 6" length) of tubing of 1/16" diameter. HAYSEP D column should be identified in the column oven of the GC. Once the small piece of tubing is installed in the oven, set its temperature at 320 ºC from trimpot settings on the GC chassis. Run the GC at 300 ºC for 8 hours along with helium carrier gas flow in the TCD detector. The FID detector is not necessarily running during baking test. Once the baking test is done, again reinstall the HAYSEP D column in the oven after removing small piece tubing. Check the CO peak by running couple of standard sample tests.

Appendix C
Bubbler/Vaporizer

C.1 Theory of Operation

Steam reforming and autothermal fuel reforming processes require steam or a vapor delivery as one of the most important input parameters for the process chamber. A vaporizer or bubbler is made in the lab in order to achieve an objective of vapors delivery with precise control specially for lab scale reactor. Simple constructions, easy to operate, inexpensive, very precise and reliable when properly used, are some of its advantages. The bubbler system, as shown in Figure C.1, consists of a liquid reservoir, often referred to as a flask which is held at constant elevated temperature. A carrier gas is flowed (bubbled) through the liquid in the flask. The rate of carrier gas flow through the flask is set with any of the flow control devices including needle valve, a rotameter, or a mass flow controller (MFC), but for the present system a MFC is used for more precise flow control. The bubbles of carrier gas absorb some of the molecules of the liquid and proceed through a heated delivery line into the main process chamber. The delivery line is heated to ensure that none of the vapor condenses prior to arriving in the process chamber. The amount of liquid vapor delivery to the process chamber strongly depends on carrier gas flow rate, stability of liquid temperature, vapor pressure in the head space above the liquid and absorption rate of the liquid into the carrier gas. The absorption rate further depends on the formation of small bubbles of carrier gas in the liquid, in which the vapor quickly reaches its equilibrium vapor pressure as the bubble float to the liquid surface. In order to ensure formation of small bubbles and rapid equilibration, a sparger, a cap with multiple small perforations, is added at the end of the carrier gas inlet dip tube.

C.2 Calibration Setup

The whole experimental unit for the bubbler system is shown in Figure C.2. The complete setup except ice box and weighing scale is used for the reforming cases. The weighing scale and ice box are used to check as well as calibrate the vapor delivery which comes out from bubbler. The setup is divided into four main parts: inlet section, process section, outlet section and temperature control system.

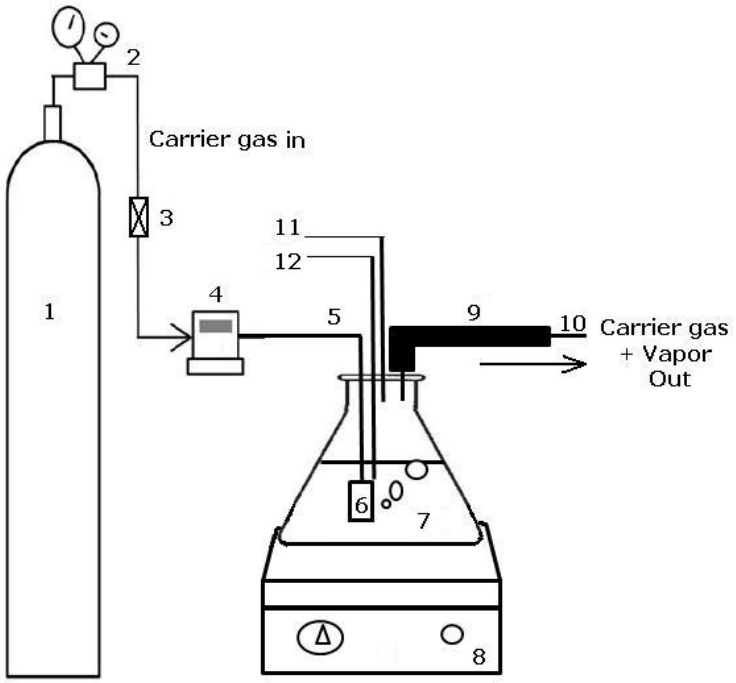

Figure C.1: Bubbler schematic diagram

1. Carrier gas cylinder 2. Regulator 3. Shut off valve 4. Mass flow controller 5. Carrier gas inlet 6. Sparger 7. Pyrex flask 8. Hot Plate 9. Heating Tape 10. Vaporized carrier gas outlet 11. Thermocouple for headspace 12. Thermocouple for liquid.

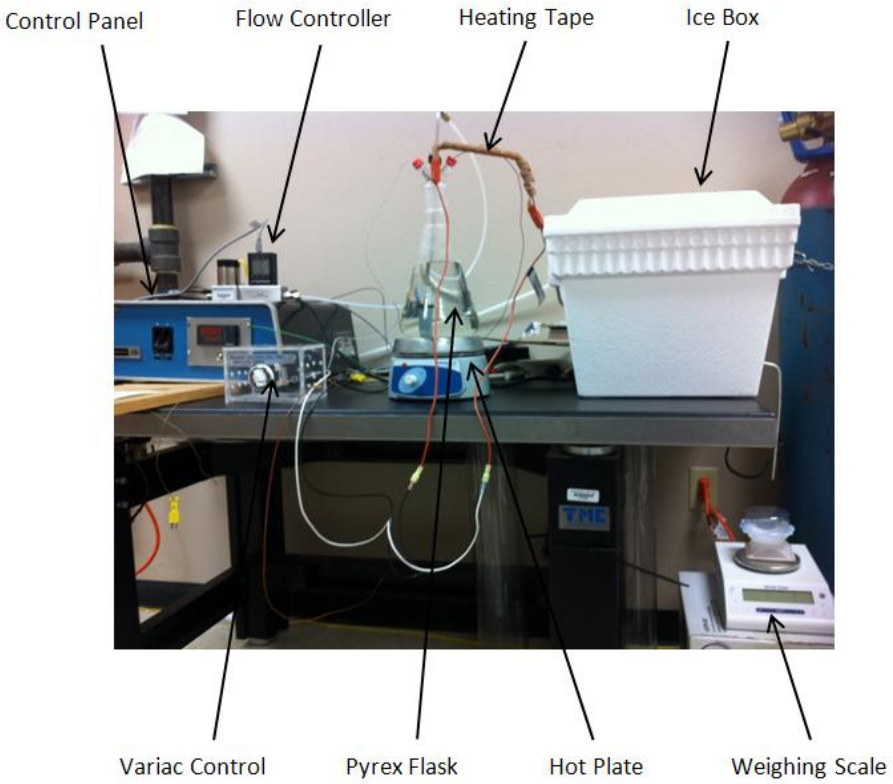

Figure C.2: Bubbler system complete setup.

C.2.1 Inlet Section

The inlet section consists of a carrier gas supply line. Nitrogen is used as a carrier gas, since it is chemically inert and so causes no reaction in the bubbler. A pressurized cylinder (1 in Figure C.1) is used to supply nitrogen. The supply line pressure of 15-20 PSIG is set by pressure regulator (2 in Figure C.1). A shut off valve (3) is provided in order to stop the flow when required. In order to achieve a stable flow rate of carrier gas into the bubbler, a mass flow controller (4), MFC[1] is used. A stainless steel tubing of 0.25" O.D. is used for gas flow. The end of carrier gas inlet dip tube (5) is provided with a sparger (6) in order to ensure formation of small bubbles and rapid equilibration.

C.2.2 Process Section

The process section as shown in Figure C.3 consists of a sealed container containing the liquid, usually water, whose vapor is to be delivered, with two tubes inserted. It should be apparent that the operation of the bubbler is dependent on the liquid level. In the present study, a transparent pyrex conical flask[2] of 2000 mL capacity is used for a purpose of visual observation of liquid level. One tube penetrates below the level of the liquid and delivers a carrier gas. The other tube extracts a carrier/vapor mixture from the headspace above the liquid. A tight seal is provided with a specially designed upper part which is also made of pyrex material. Silicon grease is used to give a tight fitting between flask neck and upper part. The upper part has four openings; two openings for carrier gas inlet tube and carrier gas-vapor mixture outlet tube respectively and other two additional openings for inserting thermocouples, one for water and other for head space temperature monitoring. The conical flak is situated on the top of a hot steel plate having 6.5" diameter. The hot plate[3] is used to provide heat to the flask. Its control is discussed in the temperature control system section.

C.2.3 Outlet Section

The outlet section consists of a stainless steel tube which extracts a carrier/vapor mixture from headspace above liquid in the flask. If the liquid temperature is greater than ambient temperature, the gas line must be heated to avoid condensation of the vapor. Therefore, the delivery line is heated to ensure that none of the vapor condenses prior to arriving in the process chamber. Temperature control of gas

[1] COLE-PARMER model # EW 32907-63, 5-500 sccm
[2] Pyrex Erlenmeyer Conical Flask, graduated, narrow mouth, VWR # 89-90-858
[3] 120 V, 575 W, VWR # 12620-978

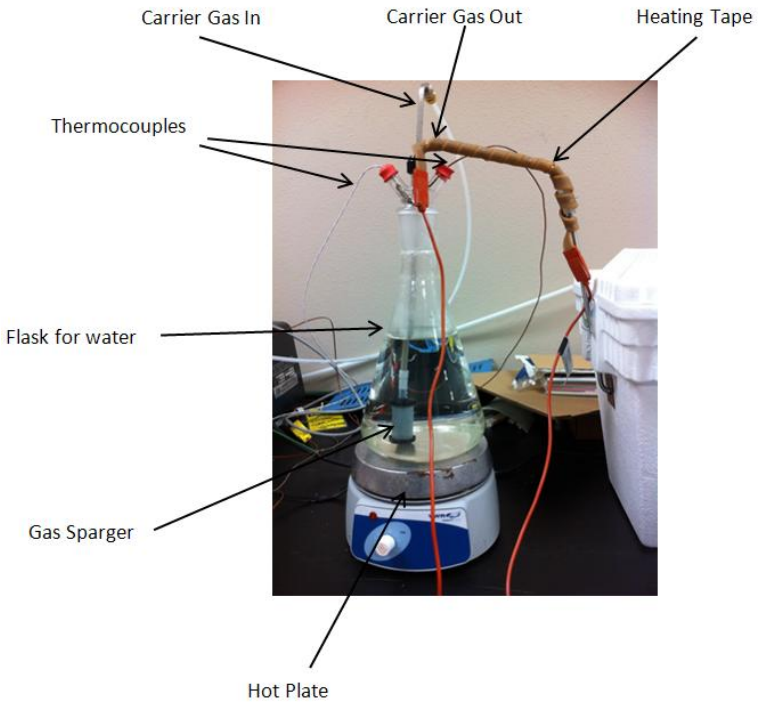

Figure C.3: Pyrex flask assembly diagram.

line is difficult and requires careful measurements, heating arrangements, and insulation. To provide sufficient heating in the range of 50 - 70°C, which depends on the set temperature of the hot plate, a heating tape[4] is wrapped around the delivery line. The temperature of wrapped tape is control by a Variac infinite control mechanism[5] which is shown in Figure C.2. The amount of vapor delivered is determined by the vapor pressure and thus the temperature of the liquid. The end of delivery tube is mounted to the ice box assembly line during condensate amount checking procedure otherwise it is mounted to the process chamber inlet supply line during steam reforming and autothermal reforming processes.

C.2.4 Temperature Control Section

Since bubbles keep the liquid agitated, the liquid itself may be reasonably isothermal; but the liquid temperature may differ considerably from the set temperature, due to transient cooling when carrier gas is turned on. If the pressure in the process chamber, for e.g. in the reactor, is less than the equilibrium vapor pressure of vapors produced in the bubbler, the bubbler doesn't work very well, because vapor flows into the process chamber in the absence of carrier gas. It is, however, very important to note that the bubbler system is only useful for controlled vapor delivery into a process chamber pressure higher

[4] size ½" x 2", max. temp. 230°C, 52 W, 120 V, OMEGALUX # SRT 051-020
[5] 120 V, 1800 W max, OMEGA # CH-152

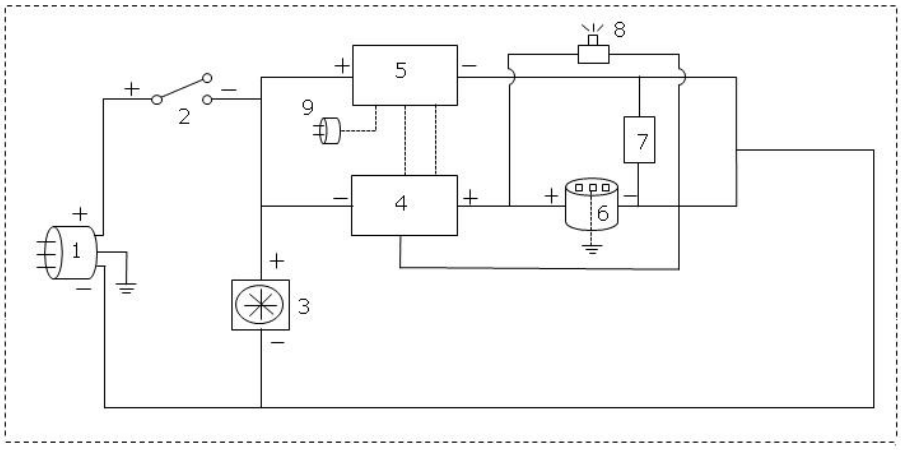

Figure C.4: Temperature control panel circuit diagram
1. 3-Prong Male Power Plug 2. Circuit Breaker Switch 3. Fan 4. SCR Power Controller 5. Temperature Controller 6. 3-Prong Female Power Plug 7. Fuse 8. LED Indicator 9. Thermocouple/RTD Probe Connector.

than the equilibrium vapor pressure of the liquid. That means vapors should be delivered at pressure higher than operating pressure (14.67 PSIA) of the reactor. Since amount of vapor delivery strongly depends on stable temperature, a tight temperature control is indispensable for accurate vapor delivery even when the nominal liquid temperature is set at room temperature. Theoretically, if there is minor change in temperature in the bubbler, for e.g. $\Delta T = \pm 1°C$ with a % error of 0.31% while taking 50°C as a reference temperature, a significant change in vapor pressure of water is obtained, i.e. $\Delta P = \pm 0.612$ kPa with a % error of 4.96%. The temperature control system (Figure C.2) consists of a control panel which controls the temperature of the bubbler system. The circuit diagram of control panel is shown in Figure C.4.

SCR Power Controller[6], shown as number 4 in Figure C.4, is provided to regulate ac power to electrical heating device, which is the hot plate (6) in this experimental setup. The controller accepts an input signal, such as 4-20 mA dc from signal conditioning device, e.g., a temperature controller[7], shown as number 5 in this setup. The combination of a temperature controller and SCR power controller provides very accurate and automatic temperature control which is very hard to achieve by any other devices combination such as solid state relay (SSR) and voltage ON/OFF type temperature controllers. The main reason for tight and smooth temperature control achieved by SCR power controller is that it has a zero crossing switched or burst fired function. The zero crossover SCR power controller convert

[6] 1 phase, 120 V, 40 amp, Zero switched, OMEGA # SCR 19Z-12-040
[7] 1/8 DIN horizontal controller, 4~20 mA linear current, alarm option relay R2, OMEGA # CN-448H-F1-R2

the analog output signal to a time proportional signal with a cycle time of about 2 seconds or less, and also provide switching at the zero crossover point to avoid generating electrical noise. Proportioning action is obtained by varying the number of cycles on to the number of cycles off. The output vary from a few cycles on and a large number of cycles off at low input, through half the cycles on and half off at half input, to all cycles on at maximum input. This output is integrated by the hot plate which produces a smoothly proportioning heat output that varies directly with the input signal. Thus, a smooth and tight temperature control is achieved.

The temperature controller used in the present setup provides proportional with integral and derivative control, also known as PID control, which helps the unit automatically compensate for changes in the system. It is usually required to provide very accurate, smooth and tight control of the process temperature. The proportional band is a temperature band expressed in % of full scale or degrees within which the controller's proportioning action takes place. The wider the proportional band, the greater the area around the setpoint in which the proportional action takes place. Integral, also known as reset, is a function which adjusts the proportional bandwidth with respect to the setpoint to compensate for offset from setpoint; that is, it adjusts the controlled temperature to setpoint after the system stabilizes. Derivative, also known as rate, senses the rate of rise or fall of system temperature and automatically adjusts the proportional band to minimize overshoot or undershoot. The RTD (Resistance temperature detector) probe [8], shown as number 9, is connected to the temperature controller in order to control the temperature exactly near the end part of delivery tube into the flask. The second thermocouple (K type) is inserted deep inside the water to measure its temperature. Due to substantial heat losses inside the flask, both thermocouples; RTD probe and K type, show a difference of 5 ~ 8 °C.

C.3 Vapors Delivery Calculations

The following assumptions are made for calculating vapors delivery:

1. The system is at steady state
2. Only vapors leave the system without splashing
3. The head region is at equilibrium with liquid vapor pressure
4. Ideal gases

[8](max. temp. up to 230°C, sensing element 100 Ω, class 'A' DIN, OMEGA # 805

We know that for ideal gases, the mixture pressure is the sum of constituent partial pressures

$$P = \sum_i P_i \tag{C.1}$$

And partial pressure can be related to the mixture composition and total pressure as

$$P_i = \chi_i P \tag{C.2}$$

Since total pressure is 1 atm. Therefore, the mole fraction of species equals its partial pressure. In other words, the ratio of mole fraction of vapor to carrier gas can be expressed as

$$\frac{\chi_v}{\chi_c} = \frac{P_v}{P_c} \tag{C.3}$$

Where, 'v' stands for vapor, 'c' stands for carrier gas and 'χ' is the mole fraction. It is also known that the total pressure, or head pressure inside bubbler is the sum of partial pressure of carrier gas and equilibrium vapor pressure (partial pressure of vapors). In other words,

$$\frac{\chi_v}{\chi_c} = \frac{P_v}{P_h - P_v} \tag{C.4}$$

Where, 'h' stands for head space inside the bubbler. It is apparent that flow rate (also the number of moles) of carrier gas at inlet equals to the flow rate of carrier gas at outlet under steady state condition and chemically inert environment inside the bubbler. Therefore, the amount of vapors delivered by bubbler can be obtained as follows:

$$\dot{V}_v = \dot{V}_c \left(\frac{P_v}{P_h - P_v} \right) \tag{C.5}$$

or

$$\dot{m_{v,out}} = \dot{m_{c,in}} \left(\frac{P_v}{P_h - P_v} \right) \tag{C.6}$$

Unit conversions are given as:

$$\dot{m}\,(g/s) = \dot{V}\,(lpm) \times \rho\left(kg/m^3\right) \times \frac{1000}{60,000} \tag{C.7}$$

We know that mole fraction of 'i' species can be written as

$$\chi_i = \frac{\dot{m}_i}{MW_i} \tag{C.8}$$

Here, 'MW' stands for molecular weight. The total output flow is also easily obtained since it must be the sum of carrier gas flow and vapor flow:

$$\dot{m}_{t,out} = \dot{m}_{c,in}\frac{P_h}{P_h - P_v} \tag{C.9}$$

Condensate amount calibration: In order to compare the amount of vapors delivered by bubbler system experimentally to that of theoretical predictions, an experiment setup is built in the lab (shown in Figure C.2). Rest of the setup is same except an ice box and weighing scale[9], which are added in order to check the amount of condensate. In a typical run, first of all, let the bubbler to be reach at particular set temperature. At the same time, set the heating tape temperature by a variac provided. Then, turn on the carrier gas supply and set the required flow rate from mass flow controller. When carrier gas flows through the system, wait for bubbler to stabilize at particular set temperature. The temperature of heating tape is measured by an external K type thermocouple which is connected to a digital data logger thermometer[10]. It is also used to record water temperature inside the bubbler. The head space temperature inside bubbler where vapors and carrier gas comes out is controlled as well as recorded by temperature controller mounted in the control panel. When all the system once stabilized, proceed with condensate amount check test. Vapors through heating tape passage are passed through an ice box in order to condense the vapors. Sufficient length of tubing is provided inside an ice box in order to condense the vapors completely. The condensate is then collected in a container and its amount is measured by a very precise weighing scale as mentioned above. Repeat the test three times in order to verify the vapors delivery (on an average of three readings) is within a range of ± 5 % relative to theoretical predictions.

[9] max. capacity = 320 g, d = 1 mg, METTLER TOLEDO # ML 303E/03
[10] OMEGA # HH1384

Table C.1: Condensate amount check at different settings in terms of temperatures and flow rates.

Tests	**Bubbler temp. (°C)**	**Heating tape temp. (°C)**	**N2 gas flow rate (mlpm)**	$\left(\frac{\chi_c}{\chi_v}\right)_{th.}$	**Condensate amount (g)**	$\left(\frac{\chi_c}{\chi_v}\right)_{exp.}$	**% error** $= \left(\frac{exp.-th.}{exp.}\right) \times 100$
Test 1	50	52 ~ 55	600	7.215	3.45	7.912	8.81
		52 ~ 55			3.77	7.241	0.355
		52 ~ 55			4.120	6.628	-8.86
Test 2	60	63 ~ 65	250	4.092	2.920	3.9	-4.92
		63 ~ 65			3.110	3.655	-11.95
		63 ~ 65			2.866	3.966	-3.18
Test 3	60	63 ~ 65	500	4.092	6.008	3.78	8.25
		63 ~ 65			5.591	4.069	0.57
		63 ~ 65			5.508	4.13	-0.9
Test 4	60	75 ~ 79	500	4.092	5.534	4.11	0.44
		75 ~ 79			5.257	4.328	5.45
		75 ~ 79			5.688	4.014	-0.19
Test 5	70	68 ~ 72	600	2.248	11.890	2.296	2.1
		68 ~ 72			12.115	2.253	0.222
		68 ~ 72			13.020	2.095	-7.303

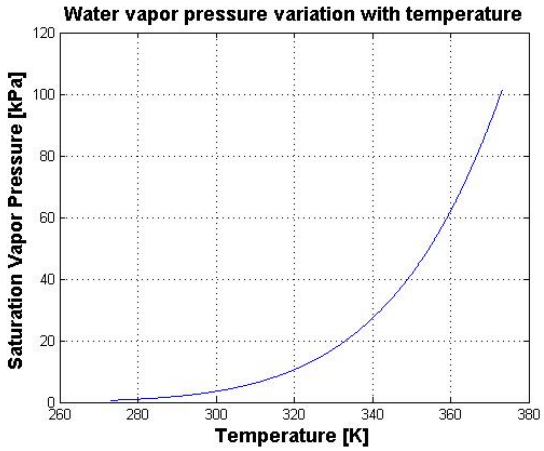

(a) T vs saturation vapor pressure of water

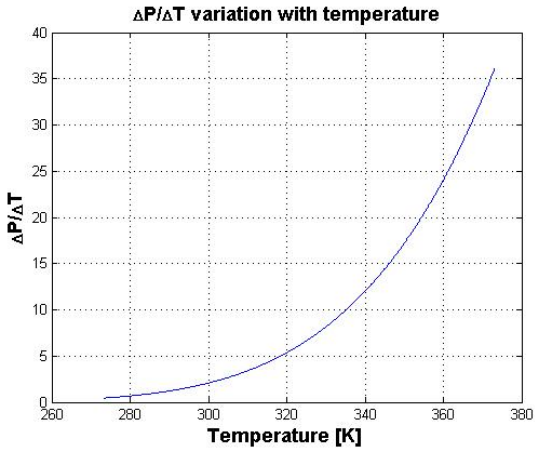

(b) T vs change in pressure per change in temperature (dP/dT)

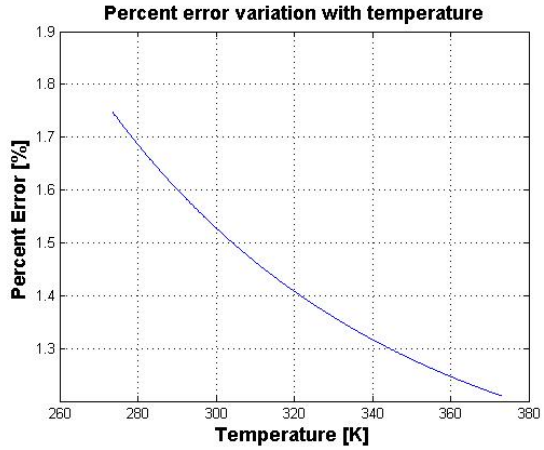

(c) T vs error percent in vapor pressure

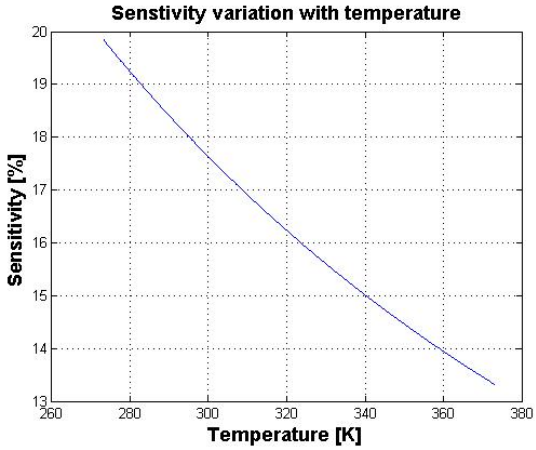

(d) T vs sensitivity

Figure C.5: Variation of different parameters with temperature

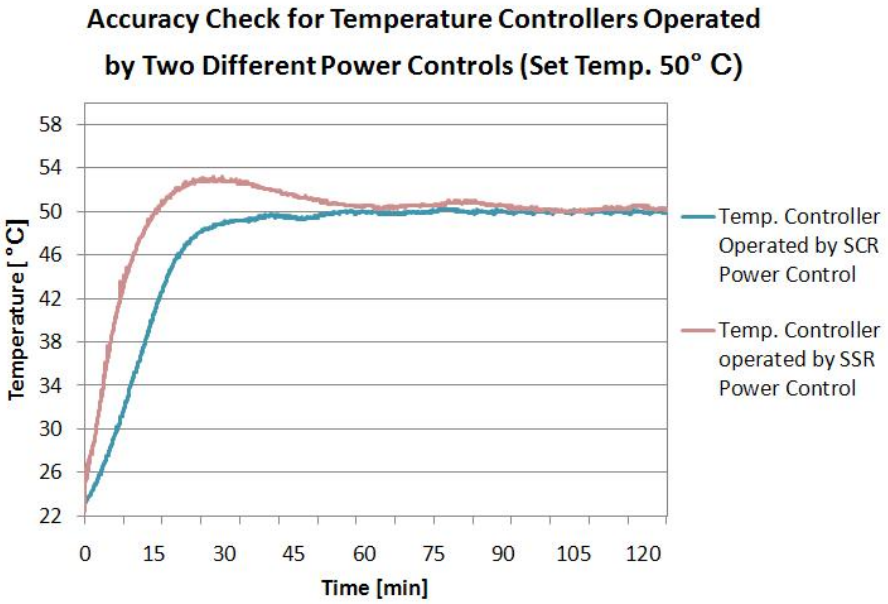

Figure C.6: Comparison between two temperature controller models (# CN-448H-F1-R2 operated by SCR power control and CN 7500 operated by SSR power control OMEGA) in terms of time taken by them to reach steady state.

Appendix D
Catalyst Preparation and Characterization

This section deals with the catalysts material quantity measurements by weight and also it deals with catalyst preparation and its characterization details.

D.1 Catalyst Quantification

I. Formulation for 10 wt% Ni/Al_2O_3, i.e. a mixture of 10 wt% of Ni and 90 wt% of Al_2O_3.

Suppose 'x' g of Al_2O_3 is added in the mixture of Ni/Al_2O_3, then '1/x' g of Ni is desired. But, nickel precursor ($Ni(NO_3)_2 \cdot 6H_2O$) is used instead of pure Ni. Therefore, the amount of nickel precursor is calculated by simply employing weight proportion method, for instance,

$$\frac{m_{Ni}}{MW_{Ni}} = \frac{m_{Ni(NO_3)_2 \cdot 6H_2O}}{MW_{Ni(NO_3)_2 \cdot 6H_2O}} \tag{D.1}$$

So, the amount of nickel precursor is

$$m_{Ni(NO_3)_2 \cdot 6H_2O} = 0.55\,x \text{ grams} \tag{D.2}$$

II. Formulation for 15 wt% CeO_2 promoted Ni/Al_2O_3, i.e. a mixture of 15 wt% of Ni and 85 wt% of Ni/Al_2O_3.

Suppose 'y' g of Ni/Al_2O_3 is added in the mixture of CeO_2 - Ni/Al_2O_3, then '1/y' g of Ni is desired. But, cerium oxide precursor ($Ce(NO_3)_2 \cdot 6H_2O$) is used instead of CeO_2. Therefore, the amount of cerium oxide precursor required is calculated by using same method as did before, such as,

Table D.1: Molecular weight of various materials used.

Material	Molecular Weight [g/mol]
Ni	58.69
$Ni(NO_3)_2 \cdot 6H_2O$	290.73
Al_2O_3	101.96
CeO_2	172.115
$Ce(NO_3)_2 \cdot 6H_2O$	434.22

Table D.2: Catalysts amount calculation and verification.

Catalyst	Material Amount	Cross-Check
10 wt% Ni/Al_2O_3	$m_{Al_2O_3}$ = 25 g, $m_{Ni(NO_3)_2 \cdot 6H_2O}$= 13.75 g, m_{Ni} = 2.78 g	$m_{Ni}(wt\%) = \frac{m_{Ni}}{m_{Ni}+m_{Al_2O_3}} = 0.10$
15 wt% CeO_2- Ni/Al_2O_3	m_{Ni/Al_2O_3} = 15 g, $m_{Ce(NO_3)_2 \cdot 6H_2O}$= 6.67 g, m_{CeO_2} = 2.64 g	$m_{CeO_2}(wt\%) = \frac{m_{CeO_2}}{m_{CeO_2}+m_{Ni/Al_2O_3}} = 0.15$

$$\frac{m_{CeO_2}}{MW_{CeO_2}} = \frac{m_{Ce(NO_3)_2 \cdot 6H_2O}}{MW_{Ce(NO_3)_2 \cdot 6H_2O}} \tag{D.3}$$

So, the amount of nickel precursor is

$$m_{Ce(NO_3)_2 \cdot 6H_2O} = 0.44\,\text{y grams} \tag{D.4}$$

D.2 Catalyst Preparation Method

The Ce promoted Ni/Al_2O_3 catalyst is prepared by using a standard catalyst impregnation method. In this method, first of all the supported nickel catalyst is prepared using nickel nitrate hexahydrate ($Ni(NO_3)_2 \cdot 6H_2O$, # 203874, SIGMA-ALDRICH, 99.999% metal basis) as the metal precursor. The material for support is Al_2O_3 (# 199974, SIGMA-ALDRICH, activated, neutral, 150 mesh). A 10 wt% Ni/Al_2O_3 catalyst is prepared by impregnating 25 g of Al_2O_3 powder with 13.75 g of nickel precursor ($Ni(NO_3)_2 \cdot 6H_2O$) into 50 ml ethanol solution at room temperature. The solution is stirred at room temperature by a magnetic stirrer at 200 rpm for 1 hour and then heat the solution at 85°C along with stirring action for 10 hours (the time is decided based on the visual observation until the solution is not dried), followed by drying it overnight in an oven at 115°C for additional 3 hours. The activation of the catalysts was performed in two consecutive steps: a calcination step, followed by an in situ reduction step. The calcination was performed at 900 °C in a 3 zone tube furnace (#STF55346C, LINDBERG/BLUE M tube furnace) in flowing air. The furnace was ramped from room temperature to the calcination temperature at a rate of 10 °C/min and then held at the setpoint temperature for 6 h. At the end of the calcination cycle, the furnace was shut off and the calcined samples were allowed to cool overnight. The reduction

step was performed in situ in the same furnace prior to the actual performance evaluation of the catalyst. The catalyst samples were reduced at 800 °C for 6 h with 8% H2/N2 with a mixture flow rate of 80 mlpm. The cerium promoted Ni/Al_2O_3 is prepared using cerium nitrate hexahydrate ($Ce(NO_3)_2{\cdot}6H_2O$, # 238538, SIGMA-ALDRICH, 99% metal basis) as a promoter. A 15 wt% $Ce\text{-}Ni/Al_2O_3$ catalyst is prepared by impregnating 15 g of Ni/Al_2O_3 with 6.66 g of cerium precursor ($Ce(NO_3)_2{\cdot}6H_2O$) into 50 ml ethanol solution, followed by stirring it at 400 rpm for 30 minutes, stir and heat it for at least 3 hours at 80°C, drying at 110°C in an oven for 8 hours and calcination in flowing air at 900°C in an oven for 7 hours. It is then reduced in H_2 atmosphere at 700°C for 7 hours. In the preliminary preparation of catalyst, both ethanol and water were used independently as a aqueous solution, however, ethanol was preferred when compared the physical texture of the catalyst powder prepared by both water and ethanol solutions.

D.3 Catalyst Characterization

After reduction, the catalyst was characterized with several physio-chemical methods. The catalyst specific surface area of 41.3 m^2/ g catalyst ($Ce/Ni/Al_2O_3$) was obtained from BET measurement. X-ray diffraction (XRD) measurements were obtained on the dried, calcined, and reduced catalyst samples, using a mini-flex model WD03541 diffractometer, using Cu Kα radiation (λ = 1.5418 Å). The voltage was 40 kV, and the electric current was 40 mA. The scanning rate was 2°/min, whereas the 2ϑ scanning range was 20° ~ 80°. Typically, a powder sample was mounted on the sample holder and then scanned to cover the indicated 2ϑ range. The measurements were used to identify the crystalline phases and possibly measure the nickel crystalline sizes. The reducibility percentage of nickel was measured from temperature-programmed reduction (TPR) using 5% H_2 in N_2 with a total flow rate of 80 mlpm. The total amount of hydrogen consumed during the reaction was 1.7 mg of H_2/g catalyst. TPR analysis was used to provide information on the reducibility of the catalyst. Also, TPR could be used in conjunction with XRD analysis to determine the species present in the catalysts.

Vita

Mandeep Sharma was born and brought up in Punjab, India. Most of school life he spent in his home town Kotkapura, Punjab. He spent early schooling at Ashoka Model High School up to 10^{th} grade and then he graduated higher secondary education from Government Brijindra College, Faridkot, Punjab. Then, he enrolled at Punjab Technical University through state level entrance exam to earn his Bachelors degree in Mechanical Engineering which he received in May 2007 with distinction award. Prior getting enrolled in graduate program at LSU, he worked for three different organizations in India: Production and Product Development Engineer at Tokai Imperial India Pvt. Ltd., Faridabad, R&D Assistant at Central Mechanical Engineering Research Institute, Durgapur, and lecturer at Bhai Maha Singh College of Engineering, Muktsar. He enrolled at Louisiana State University in January 2011 to pursue a Master of Science degree in Mechanical Engineering curriculum with majoring in Thermal & Fluid Science. Commencing January 2011,he has been working as a Graduate Research Assistant in Dr. Ingmar Schoegl's combustion research group at LSU. He is a candidate for graduation in Spring 2013 for his research, Development of a Laboratory Scale Reactor Facility to Generate Hydrogen Rich Syngas via Thermochemical Energy Conversion Routes. Immediately after graduation, he seeks himself working as an engineer in R&D in energy and gas sector.